Title
Photoluminescence Blinking, Stimulated Emission, and Charge Carrier Dynamics in Single Semiconductor Nanostructures

Author
Gibson, Natalie Anne

Publication Date
2018

Peer reviewed|Thesis/dissertation

Photoluminescence Blinking, Stimulated Emission, and Charge Carrier Dynamics in Single Semiconductor Nanostructures

by

Natalie Anne Gibson

A dissertation submitted in partial satisfaction of the

requirements for the degree of

Doctor of Philosophy

in

Chemistry

in the

Graduate Division

of the

University of California, Berkeley

Committee in charge:

Professor Stephen R. Leone, Chair
Professor Ke Xu
Professor Alessandra Lanzara

Summer 2018

Photoluminescence Blinking, Stimulated Emission, and Charge Carrier Dynamics in Single Semiconductor Nanostructures

Abstract

Photoluminescence Blinking, Stimulated Emission, and Charge Carrier Dynamics in Single Semiconductor Nanostructures

by

Natalie Anne Gibson

Doctor of Philosophy in Chemistry

University of California, Berkeley

Professor Stephen R. Leone, Chair

Semiconductor nanostructures are a class of materials that have many attractive properties for optoelectronic applications and incorporation into solid-state devices. Compared to bulk semiconductors, they offer discrete, tunable electronic energy levels and an enhancement of many charge carrier interactions. Improving our understanding of the charge dynamics in these materials and how their behavior fundamentally differs from bulk solids will be crucial for ongoing and future development of semiconductor nanostructure devices. In this dissertation, the use of single particle spectroscopy to probe charge carrier dynamics in semiconductor nanostructures is described.

The first introductory chapter provides an overview of some elementary background knowledge regarding the unique electronic structure of confined semiconductors and how this results in their distinct carrier dynamics. The advantages of single particle experiments are discussed as well as the detection methods available to obtain a sufficiently high signal-to-noise ratio, focusing primarily on the photoluminescence (PL) detection of a single optically excited particle. Finally, PL blinking in single semiconductor nanocrystals (NCs) is introduced and the leading theories proposed to account for the phenomenon are summarized. The second chapter details an experimental setup optimized for studying the PL emission from single particles, including an ultrafast, tunable laser system as the excitation source, a confocal microscope to obtain a small focal volume for single particle excitation, and the detection and acquisition components, namely sensitive photodiodes and time-correlated single photon counting techniques.

The subsequent three chapters present results from a range of semiconductor nano-materials. The third and fourth chapters focus on PL blinking in semiconductor NCs, beginning with the use of PL blinking results in thick-shell CdSe/CdS chalcogenide NCs to compare the effectiveness of two distinct analysis methods for probing multi-level emission. Extending to lead halide $CsPbBr_3$ perovskite NCs, PL blinking is investigated to understand how charge trap-

ping in these newly available compositions compares to traditional chalcogenide NCs. The next chapter provides three condensed summaries of PL studies in semiconductor nanowires (NWs). Time-resolved PL experiments of colloidal $CsPbX_3$ (X = Cl, Br, I) NWs and InP NWs are detailed, and a spectroscopic study of stimulated emission in isolated $CsPbBr_3$ NWs is described. Finally, the last chapter offers concluding remarks of the dissertation as well as a glimpse into the possible future directions of the laboratory.

To Matthew - my best friend, husband, and partner in everything

Contents

List of Figures

List of Tables

Acknowledgments

I am extremely grateful for the many supportive and inspiring people who helped me navigate through graduate school. It was the advice from mentors, comradery from friends, and unwavering encouragement from family that made the journey possible.

I would like to express my appreciation to my Ph.D. research advisor, Stephen Leone. By providing support and guidance when needed, but also flexibility and independence when appropriate, Steve allowed me to develop my critical thinking and technical troubleshooting skills in my own way, and always pushed me to follow through on the completion of projects. Under his mentorship, I was able to discover the aspects of science that I enjoy the most, which I know will prove to be invaluable insight going forward.

I can divide my time in the Leone group into three eras, and in each one, there were many lab-mates who had an impact on my time here at Berkeley. My early days in the group were defined by a tight-knit social community, of the sorts that I have since come to recognize as rare in academia and in the workplace in general. Lucas and Marina joined the group at the same time, so we endured all of the tough experiences together. I owe a special thank you to Lucas for being such a kind and loyal friend for so many years. I am also especially grateful for the close and undoubtedly long-lasting friendship I developed with Andrew. Desire inspired me to join my project, taught me how to be a laser chick, what it really means to be a good teacher, and so, so many other things. The friendship I developed with Christian during our overlap in the group was most enjoyable, and has only grown since. Thanks to those mentioned above as well as my friends and colleagues Chang-Ming, Lauren, Marieke, Chris, Denisia, and Mihai, for all the softball games, ski trips, holiday parties, beach trips, etc., and for making my early years in the Leone group my most memorable.

During my middle years, it was the likes of Henry, Peter, Maurizio, Kirsten, Aditi, Eunice, Michael, and Mazyar who helped me endure and surpass the quintessential grad school burnout time. I could always count on the lunch breaks, coffee hours, chemkegs, and after-work hangouts to lift my spirits. Towards the end of my time, our group had many newcomers and fresh faces. I wish them every success in the lab, and trust they will continue the tradition of having fun outside of it. Kathleen, our administrative assistant, was a constant, friendly presence throughout my entire tenure in the group. Beyond her tireless organization, she was always available for a chat and to offer words of support.

I feel very lucky for all the friends I have made outside of the Leone group. Ashley, you have been the most reliable ally and helped me through so many challenges at work and at life. Rachel and Travis, you are some of the most down-to-earth and friendly people I have met. Sam and Jon, thank you for your deck. And for being awesome. Tyler and Sophia, you are some of the funniest people to have the most fun with. I am also extremely grateful for the old friends that have stayed close despite being so far away. Austin and Elisabet,

our visits back and forth, with the highlight of course being caravanning around Spain with Matthew and Colin, are some of my favorite all-time memories. Dara, my best buddy from Mountain, you will always be my oldest, vair vair close friend. My university roommates Jessica, Kate, and Emily, I hope our reunions continue and with increased frequency - you are all so amazing.

I will forever be indebted to my parents for all of the opportunities they have provided me with and their never-ending encouragement towards whatever challenge I am faced with. Their support throughout my grad school days was no different, and their visits were some of the highlights of the last five years. To my entire family - my parents, my siblings Laura, Paul, and Patrick, all of my extended family, Don and Lana and all of my other in-laws - even when I struggled to find a clear way of explaining what it is that I do, you have always understood that graduate school is a long, arduous journey and you have been there for me along the way. Thank you.

Lastly, to my best friend and partner Matthew, you have *literally* been there every step of the way. From driving to Berkeley from Canada with one car of belongings, no home, and no idea what we were truly getting ourselves into, to celebrating handing in this dissertation and my last day of work, you have been right there. From you, I learned how to stress less, be calm, not freak out over the little things, and leave work behind at the end of each day. I really cannot imagine how I could have successfully navigated graduate school without you there. Thank you a million times over.

Chapter 1

Introduction

1.1 Optical and Electronic Properties of Semiconductor Nanostructures

Semiconductors are one of the most ubiquitous materials in our modern world. Anything computerized undoubtedly contains semiconductors at the core of its technology, and anything manufactured in the past few decades either contains semiconductors or it was made from a machine that does. This widespread usefulness is owed to their many unique and versatile properties. Semiconductors are a group of crystalline solid materials that have electrical conductivities and energy bandgaps between those of metals and insulators,[1] which can be precisely controlled through the introduction of impurities (i.e., doping). The behavior of charge carriers at junctions of differently doped regions allows semiconductor materials to act as switches, amplifiers, and energy converters, the solid-state devices that form the basis of all modern electronics.

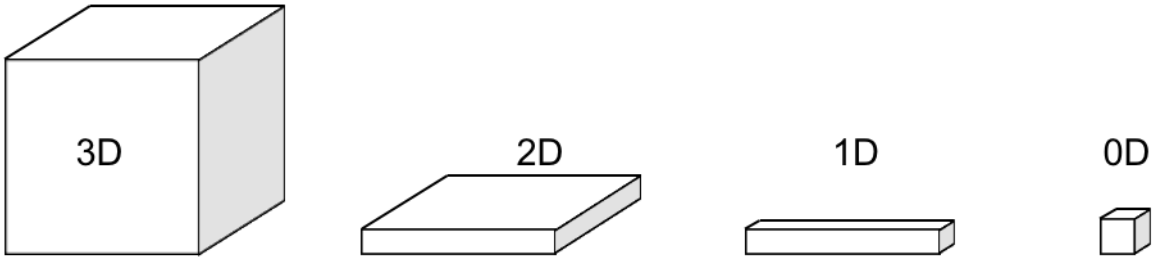

Figure 1.1: 3-D bulk solid compared with nanostructures of varying dimensions: 2-D nanoplates or quantum wells, 1-D nanowires or nanorods, and 0-D nanocrystals.

The first transistor was demonstrated in 1947, and the first integrated circuit in 1958.[1] A more recent technology breakthrough has been the nano revolution that began in the 1980s but gained significant momentum around 2000. Nanostructures are mostly synthetically

fabricated and contain at least one dimension (D) that is between $1 - 100$ nm.[2] Figure 1.1 compares the geometries of different nanostructures with bulk solids: 0-D nanocrystals, 1-D nanowires, and 2-D nanoplates. Like semiconductors, nanomaterials have been commercialized in an extensive array of applications. Silver nanoparticles have been incorporated into products in the medical, cosmetic, food packaging, bioengineering, electrochemistry, and catalysis industries, largely due to their antibacterial and antimicrobial activity, and have been[3] Titanium dioxide nanoparticles can be found in sunscreen, antifogging coatings, and paints, among many other products,[4] and these are just two out of many widely commercialized nanomaterials. Many of their enhanced properties compared to bulk materials arise from their larger surface areas. As the surface-to-volume ratio of a material increases, a greater amount of the material is available to come into contact and react with the surrounding environment.

1.1.1 Electronic Structure and Charge Carrier Dynamics

Like all nanomaterials, the increased surface area of semiconductor nanoparticles leads to several advantages over their bulk counterparts; however, they have one additional property that makes them extremely unique and versatile. When the size of a semiconductor nanoparticle is reduced below ~ 10 nm, its electronic transitions become discrete and quantized (see Figure 1.2), comparable to atoms rather than bulk semiconductors with their continuous density of states. Further, these discrete transitions exhibit a drastic size dependence, resulting in fundamental properties, such as the bandgap energy and the radiative rate, which can span across enormous ranges within the same chemical composition simply by tuning the nanoparticle size. This size dependence is nothing inherently unique to semiconductors. As the size of any material is reduced, a transition will occur where size-dependent variations in electrical and optical properties begin to be observed.[5] At any given temperature, this size transition merely occurs for semiconductors in a much larger size regime than any other material.

When an electron in a semiconductor is excited with sufficient energy, it moves into the conduction band and leaves behind a vacancy in the valence band. A valence electron can thermally hop into the vacancy, filling one empty state while creating a new one. This hopping motion is equivalent to a classical particle with a positive charge moving in the valence band, so the vacancy is called a hole and treated as a positively charged quasiparticle.[1] Being oppositely charged, the free electron in the conduction band and free hole in the valence band experience an attractive Coulomb interaction that can bind them together to form a bound electron-hole pair called an exciton. Since the Coulomb attractive force provides a stabilizing energy balance, the exciton has a lower energy than its unbound constituents. This interaction is analogous to the binding of one electron and one proton to form a neutral hydrogen atom. As such, it is convenient to use similar nomenclature and mathematical equations that are used to calculate properties about a hydrogen atom to describe an exci-

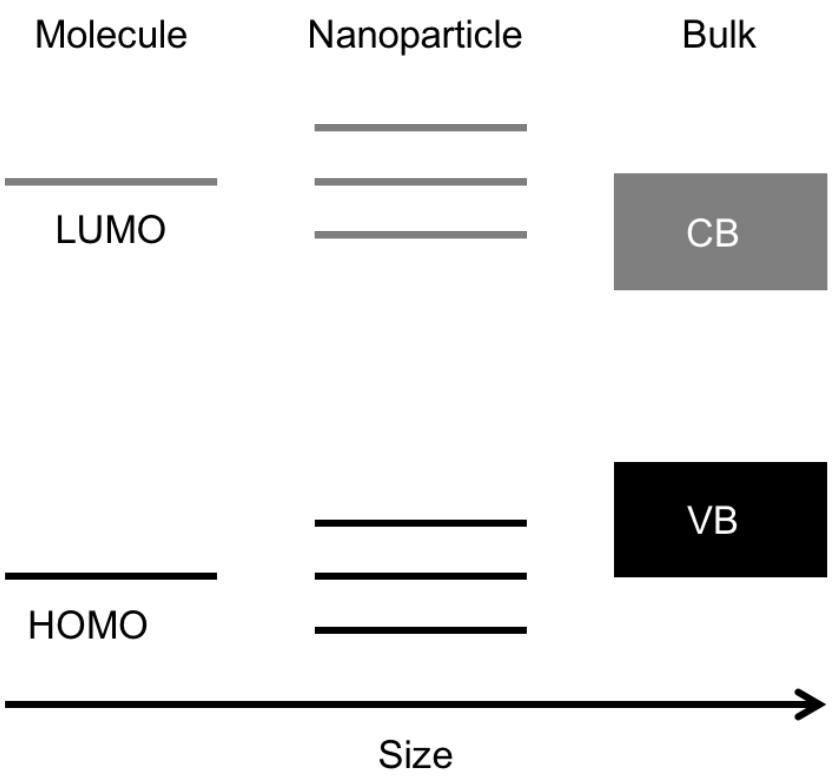

Figure 1.2: Energy level spacing of a semiconductor material, demonstrating the difference in electronic structure for three different size regimes: molecular orbitals for a molecule, bands for a bulk semiconductor, and an intermediate structure for nanoparticles.

ton. For example, the most probable spatial separation of an electron and hole, the Bohr exciton radius, a_{ex}, can be calculated using a modified Bohr model equation:

$$a_{ex} = \frac{\epsilon_0 \epsilon_r h^2}{\pi \mu e^2} \tag{1.1}$$

where ϵ_0 is the vacuum permittivity, ϵ_r is the relative permittivity or dielectric constant of the material, h is Planck's constant, e is the electron charge, and μ is the reduced mass of the electron-hole pair. This is equivalent to:

$$a_{ex} = \frac{a_0 \epsilon_r}{\mu / m_e} \tag{1.2}$$

where a_0 is the Bohr radius, the orbital radius between the electron and proton in a hydrogen atom, equal to $\epsilon_0 h^2 / \pi m_e e^2 = 0.529$ Å. The most common semiconductors have a Bohr exciton radius on the order or $\sim 1 - 10$ nm.[6] When a semiconductor material is confined to sizes comparable to or smaller than its Bohr exciton radius, the exciton becomes spatially

confined in a manner similar to the particle-in-a-box quantum mechanical problem. The boundaries of the box, defined by the potential energy of the system (e.g., infinite potential energy outside of box and zero inside), enforce boundary conditions that the wavefunction of a particle inside the box must satisfy. These boundary conditions lead to the quantization of allowed energy levels for the particle, where the energy scales as $E \propto 1/L^2$ with the length of the box. Likewise, when charges are spatially confined within a semiconductor nanoparticle, the allowed energy levels for the nanoparticle become quantized and scale with the radius as $E \propto 1/R^2$.

An effective mass model developed by Brus offers a suitable starting point to predicting the energy levels of a confined semiconductor.[7] In this model, the energy of the lowest excited state in a semiconductor nanocrystal (NC) confined in all three dimensions is given by:

$$E_g = E_{g\,(bulk)} + \frac{h^2}{8R^2}\left(\frac{1}{m_e} + \frac{1}{m_h}\right) - \frac{1.8e^2}{4\pi\epsilon_0\epsilon_r R} + \frac{e^2}{R}\overline{\sum_{k=1}^{\infty}\alpha_k\left(\frac{S}{R}\right)^{2k}} \tag{1.3}$$

The first term is the bulk semiconductor bandgap energy that begins to be modified by the latter terms when R approaches a_{ex}. The second term, as described above, is the kinetic energy of localization and represents the energetic penalty of spatially confining charges within a potential barrier. This dominant term is responsible for the general trend that the bandgap energy of a semiconductor NC increases with decreasing NC radius. The last two terms are related to the potential energy inside the NC (potential energy assumed to be infinite outside the NC). The Coulombic interaction (third term) between the electron-hole pair, screened by the crystal lattice, is an attractive interaction that lowers the energy. Lastly, the final term has the smallest contribution and derives from the interaction of one charge with the polarization created by the other charge.

This elementary model works well for weakly confined NCs where $R \sim a_{ex}$ but breaks down in the strongly confined regime where $R \ll a_{ex}$. More complex models have been derived by incorporating non-spherical particle shapes, surface energy levels, *j-j* spin-orbital coupling and band mixing, and electron-hole correlation - the latter becomes crucial at very small sizes. The effective mass model treats the charges as moving independently but in reality, the electron and hole will try to reside near each other to maximize their Coulomb attraction and the polarization term pushes both charges towards the center of the NC; both of these lead to a correlated increase in the localization kinetic energy. Irrespective of the exact relationship between the bandgap energy and size, the overall outcomes of confining a semiconductor to the nano scale include quantized energy levels, a discrete electronic density of states, and a concentration of oscillator strength to just a few transitions.[5] The electronic structure of semiconductor nanoparticles as well as their enhanced surface-to-volume ratio result in charge carrier dynamics that significantly differ from those in bulk semiconductors.

Assuming no bias or other external force is applied to affect charge carriers after an above-bandgap excitation in semiconductors, the carriers will proceed to relax back down to the ground state via several relaxation pathways. In bulk semiconductors, an above-bandgap optical excitation initially creates a non-equilibrium distribution of hot electrons and holes. The hot carriers exchange energy and rapidly thermalize to a Fermi-Dirac equilibrium distribution by collisional scattering among themselves ($\sim$ few fs). On this ultrafast timescale, the electronic system has thermalized but remains at a much higher temperature than the lattice. Excitons can also be formed during this fast electronic thermalization timescale. The hot carrier distributions continue cooling down through scattering with lattice phonons ($<$ ps), the quantum unit of a collective crystal vibration.[8] The carrier cooling times depend on the effective mass of the carriers and the amount of energy imparted to them initially. The initial photoexcitation energy for an electron and hole, E_e and E_h respectively, obey the relation:[9]

$$E_e + E_h = \hbar\omega_L - E_G \tag{1.4}$$

where ω_L is the laser frequency and E_G is the bandgap energy. The effective mass of the hole is typically larger than the electron, so that $E_h < E_e$. As a result, following carrier-carrier scatting, holes will relax to the band edge more quickly since they have less energy to dissipate and because they are more massive.[9] Once the conduction and valence band edges have been populated, further relaxation can occur through a range of radiative and nonradiative mechanisms. Radiative recombination can occur where an electron and hole recombine through the emission of a photon, also called fluorescence or photoluminescence (PL). Since the timescale for radiative recombination (ns to μs) is much longer than the carrier-phonon relaxation time, emission typically occurs at the band edge. Nonradiative recombination, where the excited carriers relax back to the ground state without the emission of a photon, can be much faster (100s of ps). As such, nonradiative decay can occur from the band edge following carrier-phonon thermalization, or hot carriers can undergo nonradiative recombination to the ground state before thermalization.

There are several different pathways for nonradiative recombination. Auger nonradiative recombination is a three-body process where an electron-hole pair transfers its energy to a spectator charge. The spectator charge can undergo an intraband transition then relax back to the band edge, or if it has sufficient energy, it can escape the semiconductor;[10] the latter is referred to as Auger ionization. Nonradiative phonon-assisted electron-hole recombination can also rapidly depopulate the excited band edge states without photon emission. Lastly, trap-assisted recombination can lead to efficient nonradiative relaxation. Defects in the semiconductor crystal lattice can exist, such as vacancies, interstitial and substitutional impurities, dislocations, or dangling bonds (see Figure 1.3), that interrupt the otherwise perfect crystallinity. These defects can form energy levels within the semiconductor bandgap that can efficiently localize charge carriers. This localization process is referred to as charge carrier trapping, and depending on the nature of the trap state and its energy level, it can

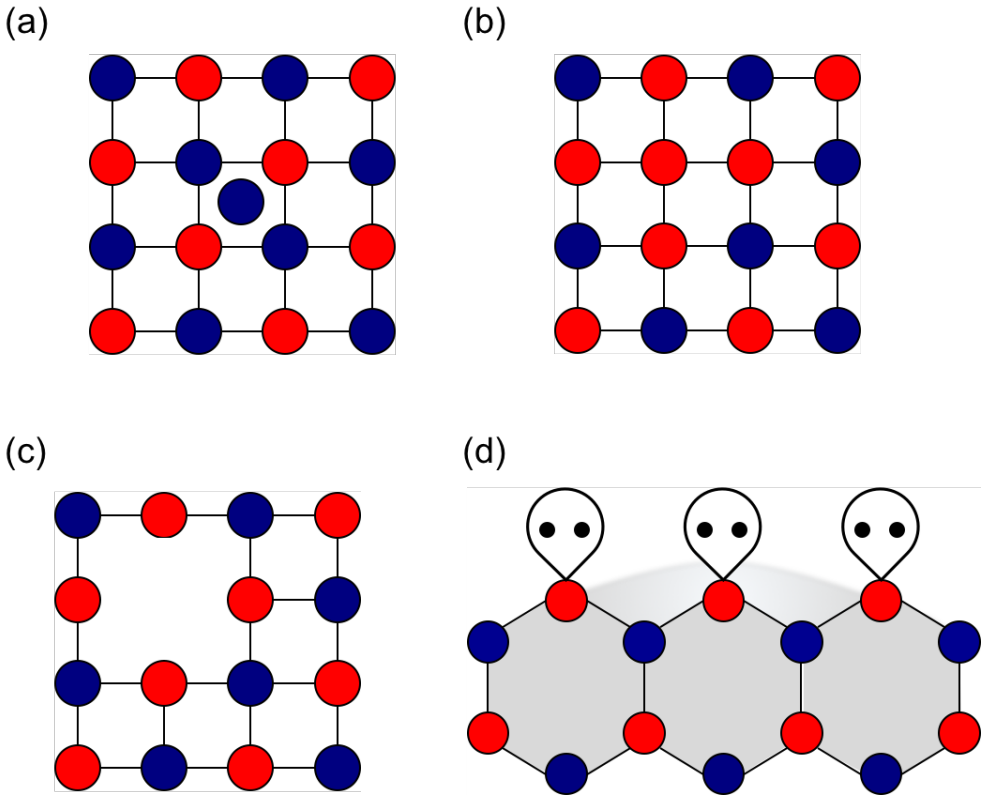

Figure 1.3: Schematic examples of types of defect states in semiconductors: (a) interstitial impurity, (b) substitutional impurities, (c) vacancy, (d) dangling bond at surface.

strongly facilitate non-radiative recombination. Shallow traps, usually classified as those lying between $0 - 10\ kT$ of the nearest band edge, can affect carrier mobility; however, deep traps at energies $> 10\ kT$ from the nearest band edge can capture charges even more efficiently and accelerate non-radiative recombination (see Figure 1.4).

In bulk semiconductors, the charge carriers strongly couple with the lattice and cause hot carriers to rapidly relax to the band edges. Subsequently, nonradiative relaxation dominates due to the high density of electronic and phonon states for bulk materials.[11] The charge carrier relaxation dynamics are quite different in semiconductor nanoparticles due to their unique electronic structure. The following discussion focuses primarily on semiconductor NCs, although it broadly pertains to the other nanoparticle geometries as well. The electronic energy levels in semiconductor NCs are discrete and separated by energies that are an order of magnitude greater than phonon energies.[11] As a result, hot carrier relaxation was initially expected to be much slower in NCs than in bulk semiconductors, a prediction referred to as the phonon bottleneck.[10–12] Many experimental studies, however, have observed that hot carrier cooling in NCs occurs at a comparable rate to bulk materials (sub-ps), a

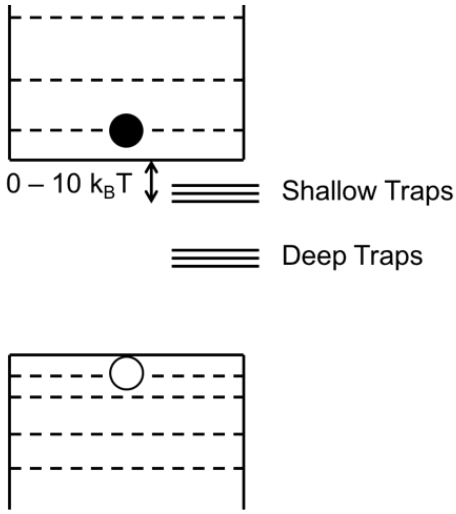

Figure 1.4: Schematic illustrating shallow versus deep traps within the bandgap of a semiconductor NC.

result that was initially perplexing.

The energy spacing of the valence states is reduced compared to the conduction states due to the heavier effective mass of holes. Hot holes are able to cool by coupling to longitudinal-optical (LO) phonon modes; in contrast, electron-LO phonon scattering should be too slow in semiconductor NCs to rapidly cool down hot electrons. Furthermore, the relationship between electron relaxation rates and NC volume contradicts the trend expected if electron-phonon relaxation dominated: the electron relaxation rate is approximately inversely proportional to the NC volume.[12] A decrease in NC volume leads to larger energy spacing and therefore a greater number of phonons are required for heat dissipation. As such, a phonon-mediated electron relaxation mechanism in NCs would predict hot electron cooling rates that decrease with decreasing NC size. Hot electron relaxation in NCs instead occurs via a three-body electron-hole-phonon interaction involving a confinement-enhanced energy transfer of the electron's excess energy to a hole, with subsequent fast hole relaxation via phonon-coupling.[13]

Charge carrier trapping is also enhanced in NCs compared to bulk semiconductors. The large surface-to-volume ratio of NCs means that a significant proportion of atoms are sensitive to the surface, where many of the defects lie. Section 1.3 expands on the effects of trap states on the recombination dynamics of semiconductor NCs. Likewise, Auger processes are greatly enhanced in quantum-confined semiconductor NCs, mostly due to the strengthening of Coulomb interactions when the charge carriers are spatially confined.[14] Lastly, confinement also greatly increases the overlap of electron and hole wavefunctions, which in turn, increases the radiative recombination rate. Figure 1.5 summarizes the charge carrier relax-

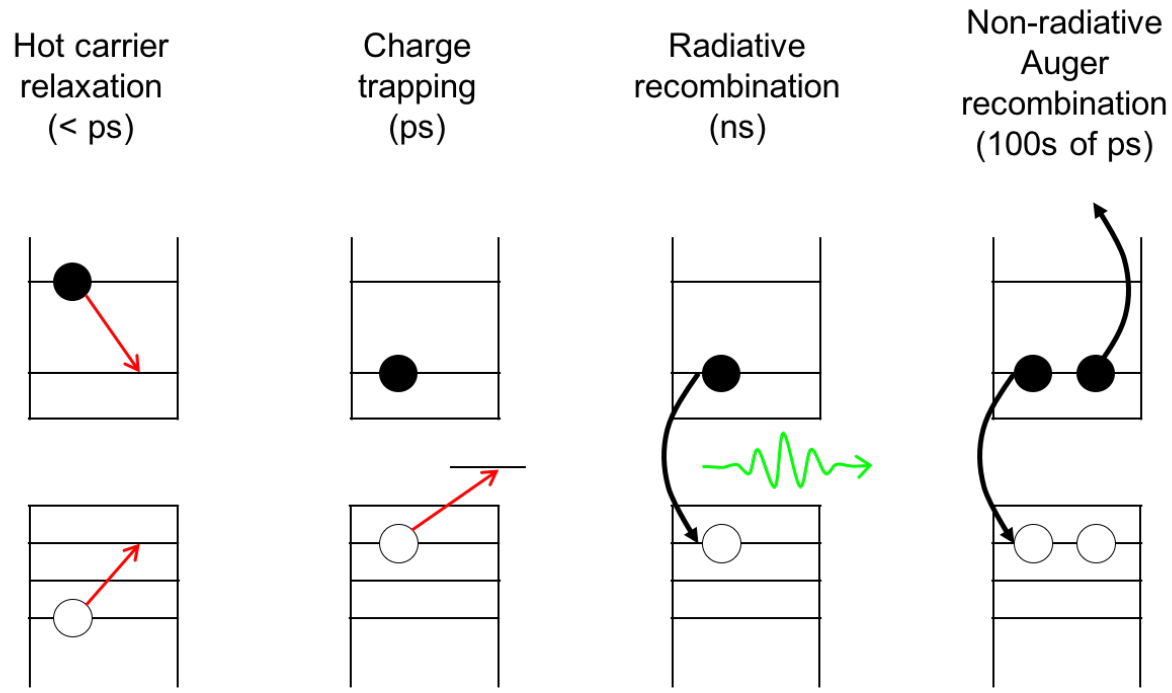

Figure 1.5: Schematic of charge carrier relaxation dynamics in semiconductor NCs illustrating (a) hot carrier relaxation, (b) charge trapping, (c) radiative recombination, and (d) nonradiative Auger recombination.

ation pathways in semiconductor NCs.

1.1.2 Superior Properties Compared to Bulk Solids

The unique electronic structure and charge carrier dynamics in semiconductor nanostructures lead to numerous advantageous properties compared to bulk semiconductors. Arguably the most notable quality is their tunability. As described above, semiconductor nanostructures exhibit discrete optical transitions that can be tuned with size. Solution-phase synthesis techniques can provide facile control over size, as well as shape, crystal structure, and monodispersity, all of which offer additional means of optical and electronic tunability.

Analogous structures to junctions in bulk semiconductors can be engineered in semiconductor NCs to tune and optimize their charge carrier dynamics for a particular application. Figure 1.6 shows four different types of structures - a core-only NC that consists of one semiconductor material, and three examples of core/shell structures that consist of one semiconductor material surrounded by a shell of another semiconductor material. Surface passivation is usually always preferable since it will reduce surface defects and therefore non-

radiative trap-assisted recombination. In the most common core/shell structure, the Type-I configuration, the core is encapsulated by a wider bandgap semiconductor to passivate the surface and eliminate any dangling bonds, and localize both carrier wavefunctions in the core. This type of structure is preferable in applications that require a maximal radiative recombination and PLQY, as greater wavefunction overlap will lead to larger radiative recombination rates. An inverted Type-I heterostructure involves a narrower bandgap material for the shell and enhances carrier extraction, which is useful in sensitized solar cells. Type-II heterostructures involve a core/shell interface that has staggered bandgaps such that both valence and conduction band edges of one material are higher in energy than the other. In this configuration, one charge carrier will be localized in the core, and the other in the shell, depending on the precise arrangement. In Figure 1.6d, the hole would be localized in the core, while the electron would reside more in the shell. Charge separation is encouraged in this type of junction, making it of interest to photovoltaic devices. Passivation of the shell surface with a molecular ligand that contains donor (HOMO) or acceptor (LUMO) levels within the semiconductor bandgap can also lead to efficient charge transfer and separation.

Besides the immense tunability offered by semiconductor NCs, their optical properties are often superior to their bulk counterparts as well. The discreteness of the electronic energy levels in NCs results in very narrow PL linewidths even at room temperature (< 100 meV), and the increased radiative recombination rate due to improved wavefunction overlap leads to high room-temperature PL quantum yields (PLQYs). Narrow linewidths coupled with high PLQYs make semiconductor NCs ideal to use as PL dyes and sensors in imaging and tracking applications, and as emitters or filters in light-emitting diodes and displays. The efficiency of Auger processes due to enhanced Coulomb interactions in NCs can strongly quench multi-excitonic emission. This makes semiconductor NCs promising candidates for single photon sources that are required in photonic quantum technologies (e.g., photonic quantum entanglement) and quantum information science (e.g., quantum computation and quantum cryptography).[15] Carrier multiplication is another Auger-type process that has demonstrated higher efficiencies in NCs than bulk semiconductors. When a NC is excited with an energy $\geq 2E_g$, the hot carriers can recombine in a collision-like Auger process to excite another electron and hole. One exciting application for carrier multiplication is the possibility of boosting the efficiency of NC-based photovoltaics; however, this requires a rapid extraction of the charge carriers before they decay via other Auger processes.[16]

The emergence and dominance of semiconductor technology in our modern world was made possible from an ongoing understanding of fundamental solid state physics and the electrical and optical properties of bulk semiconductors. The advent of semiconductor nanostructures and the continued development of nano-based applications and devices, likewise, will rely on a continuously improving fundamental understanding of charge carrier dynamics in semiconductor nanostructures and how their behavior differs from bulk solids.

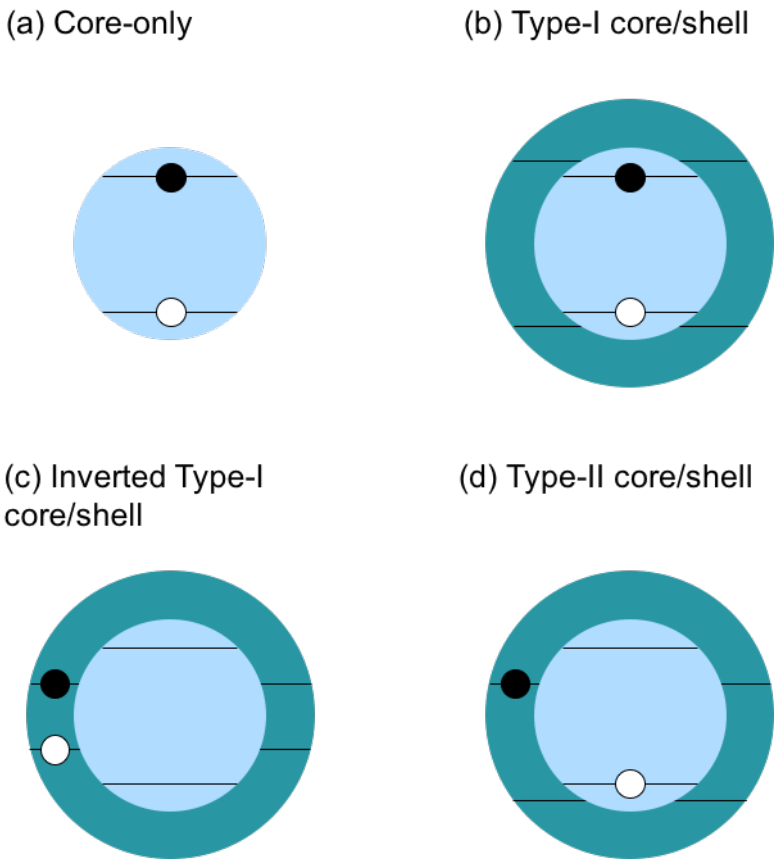

Figure 1.6: (a) Core-only NC consisting of only one semiconductor material, and (b)-(d) Core/shell heterostructures consisting of one semiconductor core encapsulated by another semiconductor shell: (b) Type-I core/shell, (c) inverted Type-I core/shell, and (d) Type-II core/shell structures.

1.2 Single Particle Studies of Semiconductor Nanostructures

1.2.1 Advantages of Single Particle Experiments

An extremely valuable experimental technique for studying charge carrier dynamics in semiconductor nanostructures is single particle spectroscopy. Single particle experiments represent the ultimate detection sensitivity, where a signal arising from one isolated particle can be distinguished from the background and measurement noise. By capturing a signal from one particle at a time, the signal averaging that is inherent to ensemble experiments can be avoided. In statistical mechanics, the ergodic hypothesis states that the time-averaged value of a certain property for a single member of an ensemble is equal to the instanta-

neous ensemble average of that property.[17] In a system where every single member of the ensemble is absolutely identical, the ergodic hypothesis consequently implies that a single particle measurement is not necessary to study the properties of a system. However, rarely do such perfectly homogeneous systems exist, especially in chemical or biological systems. Whether the inhomogeneity is due to differences in the members of an ensemble or arises from a measurement time that is shorter than some dynamic fluctuations, the ergodic hypothesis becomes irrelevant and a property of a single member studied over time is not equal to the ensemble average.[17] The removal of ensemble averaging, in turn, reveals important information about the system that is otherwise obscured.

For instance, an ensemble experiment produces an average value of a physical property. When many individual particles are probed one at a time, a frequency histogram of the distribution of the property can also be obtained.[18] A distribution will always contain more information than a single average value on its own. It can provide information about the heterogeneity of a sample, or the existence of multiple subsets in a distribution that could be due to different conformational states, for example. The observation of dynamic fluctuations that are averaged out in ensembles is another key motivation for single particle experiments. The precise behavior of a fluctuating property could be entirely unique to each member of an ensemble, such that an ensemble experiment could never reveal the rich nature of the fluctuations. An example of these kinds of fluctuations is the intermittent PL signal observed in a single semiconductor NC, which will be discussed in Section 1.3. Alternatively, the fluctuations could exist in a similar manner for each member of an ensemble undergoing the same time-dependent series of events, but observing the series of events on the ensemble level would require precise synchronization of many particles to ensure their trajectories are all in phase.[19] Single particle experiments avoid the need for synchronization, permitting, for example, observations of a single enzyme molecule during its catalytic cycle, or the conformational dynamics of DNA, RNA, and other macromolecules. Lastly, the local environment surrounding each single particle in an ensemble is often unique, especially in chemical and biological systems. If a single particle is sensitive to its nanoenvironment, it can act as a local reporter, which is very useful in sensing applications.[18]

1.2.2 Signal-to-Noise Ratio

There is great potential to gain new information from a single particle, but isolating its signal amidst the background noise is a technological challenge. Many components of an experimental setup can contribute to the background signal, including sample impurities, inherent background noise from the detectors used, radio-frequency interference from the surrounding environment, and any other unwanted signal from the various experimental components used. In order to obtain any meaningful information, the signal must be larger than the fluctuations in the background. In other words, the signal-to-noise ratio (SNR) must be greater than unity. There are several methods that are presently available to ensure that SNR > 1,

but by far the most routinely achievable and widespread method is through the detection of the PL emitted from an optically excited single particle, a feat that was only achieved at room temperature relatively recently in 1990.[20] The emission of PL from a semiconductor nanoparticle, as described in Section 1.1, is caused by the radiative recombination of an excited electron-hole pair. More generally, fluorescence or PL emission can occur for any material after the absorption of photons. It is one form of spontaneous emission where an excited state transitions to a lower energy state, emitting energy in the form of a photon. PL detection is ideal for single particle experiments due to its sensitivity to the environment, and since it can appear as a bright signal against a dark background through the simple use of optical filters. Further, reducing the observation volume and rejecting out-of-plane background signal drastically improves the SNR, and an experimental technique already exists for PL detection that can achieve these tasks, confocal microscopy, which is described further in Chapter 2.

The SNR of the PL emitted from a single particle, in counts per unit time, is given by:

$$\begin{aligned} SNR &= \frac{\text{PL signal}}{\sqrt{\text{PL signal+background noise}}} \\ &= \frac{DQN_{abs}}{\sqrt{DQN_{abs} + C_B P_0 + N_D}} \end{aligned} \tag{1.5}$$

where D is the setup's detection efficiency, Q is the sample's quantum yield, N_{abs} is the number of absorbed photons, C_B is the background counts per incident power (P_0, and N_D is the number of detector dark counts per second.

The PL signal can be very intuitively understood as the product of the number of photons absorbed by the sample, N_{abs} (at low intensities well below the saturation intensity), the likelihood that absorbed photons will then be emitted, which is equal to the quantum yield, Q, and the detection efficiency of the setup, D. N_{abs} depends on both the intrinsic properties of the single particle, how strongly it absorbs light, given by the wavelength-dependent absorption cross-section or equivalently the extinction coefficient, as well as the excitation conditions, how intense the light is and whether it is a pulsed or continuous light source. For a semiconductor material excited with pulsed excitation, $N_{abs} = N_{ex}$, the average number of excitons absorbed per excitation pulse. Q is entirely dependent on the sample, deriving from the intrinsic radiative rate, Γ, and the sum of all nonradiative rates, k_{nr}:

$$Q = \frac{\Gamma}{\Gamma + \sum k_{nr}} \tag{1.6}$$

The last component of the numerator in Equation 1.5, the detection efficiency D, will depend on the microscope optics as well as the quantum efficiency (QE) of the detectors used. The

QE of standard detectors used is $\sim 50\%$, and the optical losses at mirrors, filters, and lenses are minimal. The dominant cause of lowering D is the collection efficiency of the objective lens:

$$\frac{1}{2}\left(1-\sqrt{1-(NA/n)^2}\right)=\frac{1}{2}\left(1-\cos\alpha\right) \tag{1.7}$$

where NA is the numerical aperature of the objective, n is the refractive index of the objective (or immersion medium if immersion objective is used), and α is the semi-aperture angle of the objective.[21] For example, for the primary 1.3-NA oil immersion objective used in most of the experiments summarized in the subsequent chapters, the collection efficiency is just under 25%. One way to increase the amount of PL that is collected is to double the collection angle by placing two objectives nose-to-nose (called 4π-microscopy).[21]

The discrete nature of photons emitted by a single particle gives rise to the form of the SNR in Equation 1.5. Photons are discrete particles that are emitted randomly (i.e., at unpredictable times), and as such, their emission from a single particle and subsequent detection are dictated by Poisson statistics. In a Poisson distribution, the uncertainty in counting a number of random events is the square root of the counted number.[22] The noise caused by fluctuations in the number of discrete events is called shot noise. If no other sources of noise were present in the PL signal from an individual particle, the optical signal would be shot-noise or photon-noise limited and Equation 1.5 would become $SNR=\sqrt{\text{PL signal}}$. In reality, it is difficult to eliminate all other sources of background noise. The detector itself will contribute some background noise, mostly from thermal excitation of carriers, when it is simply operating but with the PL signal (or, the excitation laser) blocked. These dark counts, N_D, represent the lowest counts that the detector can exhibit. Any other noise that does not originate from the PL of the single particle contributes additional background counts, C_B. Sources can include impurities in the sample, emission from the substrate or sample holder, scattered excitation light, or unblocked light from other sources such as any room lights. The use of several high-quality optical filters, careful sample preparation, and dark enclosures will help to reduce C_B.

The background noise and detection efficiency of an experimental setup will be roughly the same across different samples, whereas the PL signal can widely vary depending on the sample and excitation conditions used. An ideal single particle sample would be one that has a strong absorption at the excitation wavelength, a large PLQY, and does not rapidly photobleach. Semiconductor nanostructures exhibit these qualities, and therefore, single particle experiments with a SNR > 1 can be successfully carried out on semiconductor nanostructures and have proven to be a very valuable tool. The removal of ensemble averaging has revealed a wealth of interesting and informative phenomena about confined semiconductors, examples of which will be expanded upon throughout this thesis. One such phenomenon, PL blinking, provides a strong motivation for studying the PL of a single semiconductor NC.

Section 1.3 will discuss how such PL measurements can be used to understand charge carrier dynamics in semiconductor NCs.

1.3 Photoluminescence Blinking in Individual Semiconductor Nanocrystals

1.3.1 Photoluminescence Blinking in Molecules

Photoluminescence intermittency or blinking refers to the observation of a single emitter's PL emission exhibiting a non-uniform intensity over time (called a PL trajectory here, sometimes referred to as a blink trace). Periods of bright PL are spontaneously interrupted by dark periods of low PL intensity, even under constant illumination, often resembling a random telegraph signal, see Figure 1.7. This behavior is smoothed out when an average PL signal is collected from an ensemble, and therefore the phenomenon is only directly detectable on the single particle level. PL blinking was first observed in semiconductor NCs in 1996, shortly after the synthesis of bright NCs was possible.[23]

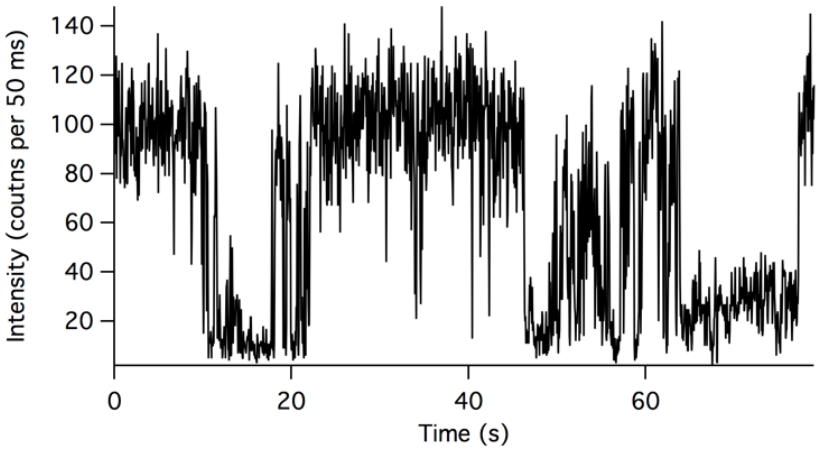

Figure 1.7: Sample PL trajectory of a single semiconductor NC, displaying large fluctuations in the PL intensity over time.

Before that, when it became technically feasible to measure the PL from a single molecule, the first room-temperature observations of PL blinking in dye molecules were achieved in 1994 using near-field optical microscopy techniques. Single rhodamine 6G molecules on a silica surface displayed intermittent PL signals, which at the time was attributed to small orientation changes causing the molecule's dipole orientation and therefore absorption and emission rates to fluctuate.[24] Single sulforhodamine 101 molecules dispersed on a glass surface were also observed to suddenly fluctuate at levels above the noise, an observation that

was postulated to be caused by spectral diffusion.[25] Since these early experiments, PL blinking has been observed in all types of fluorophores including many other single molecules, fluorescent proteins, polymer segments, molecular crystals, organic molecules in polymers, as well as in semiconductor nanoparticles.[26]

The physical mechanisms responsible for blinking differ between types of single molecule systems. For instance, PL fluctuations in molecular crystals are caused by triplet-state blinking. Bright periods of emission occur when the crystal relaxes from the excited singlet state to the ground state radiatively through fluorescence. Upon intersystem crossing to a metastable triplet state, the crystal remains dark until the ground state recovers, usually through phosphorescence (see Figure 1.8). Other types of quantum jumps between a bright state and a nonfluorescent state or metastable shelf state have also been observed for frequency-trapped single ions and molecular impurities embedded inside crystalline matrices.[27] The nature of the underlying kinetics responsible for PL blinking can be uncovered by separating the PL trajectories into bright and dark states (also referred to as 'on' and 'off' states, respectively), then plotting a histogram of the frequency of on durations, $P(\tau_{on})$, and off durations, $P(\tau_{off})$. These are herein referred to as probability distributions; more detail regarding this analysis method is given in Chapter 2. For triplet-state blinking and any kind of quantum jumping, the on state switches to an off state at a single non-fluctuating rate (intersystem crossing rate, k_{int}) and as a result, the $P(\tau_{on})$ distribution will exhibit single-exponential kinetics: $P(\tau_{on}) \propto \mathrm{e}^{-k_{int}t}$. Likewise, if the recovery to the ground state, k_{rec}, occurs at a constant rate then the $P(\tau_{off})$ distribution will also exhibit single-exponential kinetics: $P(\tau_{off}) \propto \mathrm{e}^{-k_{rec}t}$.

1.3.2 Photoluminescence Blinking in Nanocrystals

Several other explanations have been frequently invoked to account for any non-exponential PL blinking behavior that has been observed, including chemical changes, rotational or other orientational changes, conformational changes in macromolecules, and changes in the surrounding environment. In the first observation of PL blinking in semiconductor NCs, a mechanism based on Auger recombination of a charged NC was proposed but not mathematically developed.[23] Efros and Rosen subsequently expanded on the proposed mechanism and performed Monte Carlo simulations to reproduce PL trajectories that exhibited the apparent two-state PL blinking observed.[28] The simulations were based on a system of rate equations involving the following sequence of events:

(i) An electron-hole pair is optically excited and radiatively recombines (NC=on)

(ii) The NC is ionized thermally or via Auger autoionization (NC switches from on $\rightarrow$ off)

(iii) The ejected charge carrier localizes in a long-lived deep trap in the surrounding matrix, leaving behind a charged NC core; the excitations that follow result in nonradiative Auger recombination of a trion that quenches the emission (NC=off)

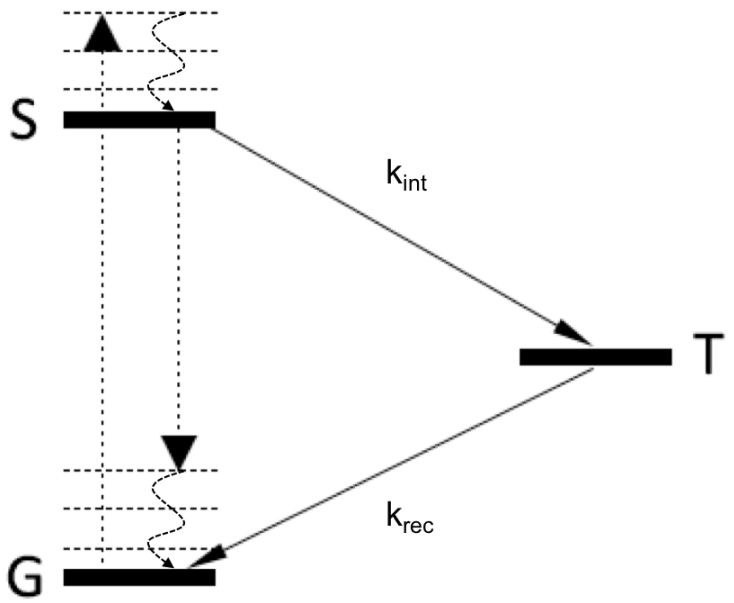

Figure 1.8: Energy level diagram of a single molecule that can display triplet-state blinking. G = singlet ground state; S = singlet excited state; T = triplet excited state; k_{int} = intersystem crossing rate; k_{rec} = triplet recovery rate.

(iv) The ejected charge carrier thermally returns to the NC (NC switches from off → on)

The key aspects of this model are that Auger recombination of a trion is responsible for the dark state, and the dark durations are dictated by the lifetime of the trapped charge. This model, while straightforward and intuitive, is inconsistent with the nature of the PL blinking that had been observed in semiconductor NCs. Involving only a single trap state, the model predicts exponential decay kinetics for both the bright and dark durations (i.e., analogous to triplet-state blinking); in contrast, it was clear even from the initial reports that the distributions of both states were highly nonexponential.[23] A few years after these early observations of blinking, it was discovered that when plotted on a semilogarithmic scale, the distributions of dark and bright times showed extensive curvature.[29] If the probability distributions of the off and on times followed exponential kinetics, the distributions would appear linear on a semilogarithmic scale. This provided strong evidence of the nonexponential behavior of the PL blinking kinetics in single NCs. It turned out that the probability distributions of both the off and on times could be well characterized by an inverse power law function:

$$P(\tau_i) \propto \tau_i^{-\alpha} \ (i\text{=off/on}) \tag{1.8}$$

where the value of α, the power law exponent, is typically $1 - 2$.[30] Several modifications to this original proposed model as well as entirely new theoretical models have been proposed to try to account for this unique power law behavior, and it remains an active area of fun-

damental research.

First of all, a power law function simply involves one quantity that varies as the power of another, $f(x) = ax^k$. There are numerous examples of power laws, in physical and mathematical relationships, and both natural and anthropogenic phenomena. In thermodynamics, phase transitions can be described by power law relationships where the scaling parameters are called critical exponents. Power law scaling is pervasive in nature, showing up in many natural geological events. For example, the durations of volcanic eruptions follows a power-law distribution, even worldwide for different volcanic environments.[31] As an example of an anthropogenic event, the electrical blackout size versus frequency in national high-voltage power grids follows a power law distribution.[32]

The origin of power law dynamics depends entirely on the situation being considered. As it pertains to PL blinking in semiconductor NCs, a power law distribution indicates that there is no characteristic timescale for the on or off times. The frequency at which a particular duration occurs scales with the length of that duration. Further, averages cannot be robustly defined since they explicitly depend on the measurement capabilities and the time window (i.e., the fastest and slowest events that can be recorded).[27] Since single on $\rightarrow$ off and off $\rightarrow$ on rates would lead to exponential kinetics for the on-time and off-time probability distributions, respectively, the observation of power law kinetics for both reveals that the switching mechanisms do not occur at single, constant rates.

Broadly, there are two classes of models that have been proposed to account for this fact. While many details regarding the proposed mechanisms may differ, there is one universal theme in common between all proposed models: PL blinking in single semiconductor NCs is related to charge carrier trapping at defects in the lattice, at the surface, or external to the NC. In one class of models, Auger recombination of a charged NC remains the cause of the diminished PL in the off state, and the NC is still proposed to remain off until it is re-neutralized. To rationalize the power law behavior, the mechanisms by which the NC switches from on $\leftrightarrow$ off differ from the original model proposed by Efros and Rosen.

An exponential density of trap states within the NC could exist, requiring energy activation for a trapped charge to escape. Using an Arrhenius approach, the rate of thermal activation would vary exponentially with the energy depth of a trap state. This scheme predicts a power law distribution for the off times but not the on times, since the net rate that the NC switches from on $\rightarrow$ off is still given by a single rate, the sum of all individual trapping rates.[27] Likewise, an exponentially distributed manifold of extrinsic trap states could exist that charges can access due to the exponential drop-off in their wave functions. The trapped charges can recover via quantum mechanical tunneling, where the rate of recovery depends exponentially on barrier height (from WKB theory).[27] Once again, a power law emerges only for the off times, and as a mathematical consequence of averaging an exponential process over an exponentially distributed set of values.[33] Many variations of these mechanisms can

account for the power law distributed off times. To predict power law kinetics for the on times, these models have been extended to include some form of diffusion, such as a fluctuating tunneling barrier height, a spatial diffusion of a trapped charge, or diffusions of the energy levels involved.[27]

In the second class of models, a hole is predicted to become trapped for a very short lifetime, then recombine nonradiatively with the conduction band electron before thermalizing. These models do not require long-lived traps and do not involve Auger recombination as the cause of a dim PL off state. To account for the power law behavior, the trapping rates fluctuate in time and a NC will remain off for the duration that the trapping rate is faster than the radiative recombination rate. One way that the trapping rate has been proposed to fluctuate is through a discrete number of surface sites that can switch between active and inactive configurations, resulting in fast trapping rates when many sites are in their active conformation and slow trapping rates when most are inactive.[34]

While the off periods have typically been found to obey the simple power law given in Equation 1.8 (on the time scale of most experiments), the on periods can be fit to an exponentially truncated power law:

$$P(\tau_i) \propto \tau_i^{-\alpha} e^{\tau_i/\tau_c} \tag{1.9}$$

where the truncation time, τ_c, is the time at which the power law kinetics cross over to exponential kinetics (example trace in Figure 1.9). The exponential truncation indicates that the on $\rightarrow$ off process at long on durations either occurs at a single rate, or the distributed rate process saturates at long on durations. An exponential truncation is directly predicted in some models proposed to explain PL blinking, while others only explain the power-law behavior at short on durations and assume an additional single-rate process such as Auger ionization occurs at long on durations.

The preceding discussion is only intended to offer a brief summary. There are a number of excellent, comprehensive reviews that provide a more detailed summary of PL blinking observations and proposed mechanisms in semiconductor NCs.[10,30,33,35] In summary, PL detection of a single, isolated semiconductor NC is an extremely informative method for studying charge carrier dynamics, in particular charge carrier trapping as it directly relates to the intermittent PL signals observed for a single particle. Chapter 2 will provide experimental details regarding how the PL from a single semiconductor nanostructure is acquired in practice.

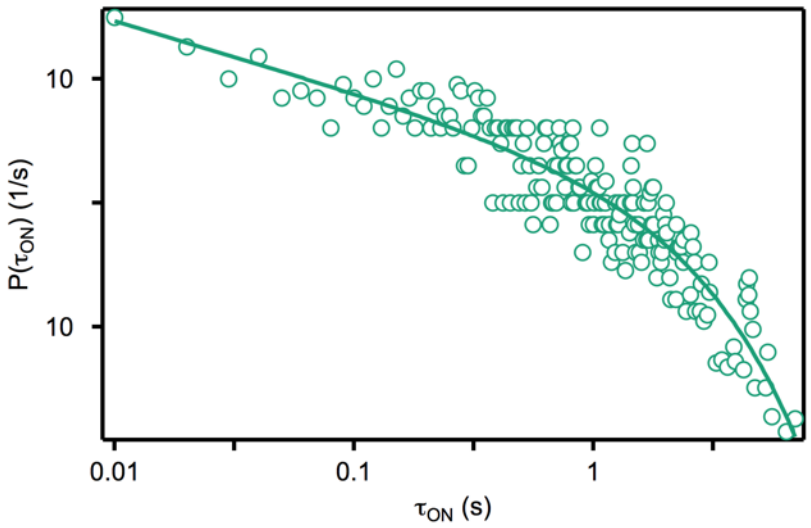

Figure 1.9: Example on-state probability distribution, following exponentially-truncated power law dynamics.

Chapter 2

Experimental Methods for Photoluminescence Detection of Single Nanostructures

2.1 Experimental Apparatus

The photoluminescence (PL) detection of a single, isolated semiconductor nanoparticle requires an excitation source, an excitation volume containing a single particle, detectors sensitive to the PL from a single particle, and a sufficient signal-to-noise ratio (SNR). An experimental apparatus that meets these requirements is accomplished using the four major components illustrated in Figure 2.1: a tunable, pulsed laser system, a confocal microscope, a sample with isolated particles, and detectors with high quantum efficiency. Each component is described in detail in this chapter: Section 2.1.1 introduces the laser system and includes several technical suggestions for maintaining and working with the system, Section 2.1.2 presents an overview of the microscope, Section 2.1.3 describes the single particle sample preparation, and Section 2.1.4 discusses the detectors used for time-resolved and spectral measurements.

2.1.1 Tunable Pulsed Laser System

The laser system used in the subsequent chapters (Figure 2.2) consists of a commercial, Ti:Sapphire regenerative amplifier (RegA 9000, Coherent) seeded by a modelocked Ti:Sapphire oscillator (Mira 900, Coherent), which are both pumped by a 532 nm diode-pumped solid-state laser (Verdi-V18, Coherent). The output of the amplifier (800 nm, 200 fs, 300 kHz) is aligned into an optical parametric amplifier (OPA 9400, Coherent) to generate the second harmonic (400 nm) and tunable visible excitation ($500 - 700$ nm).

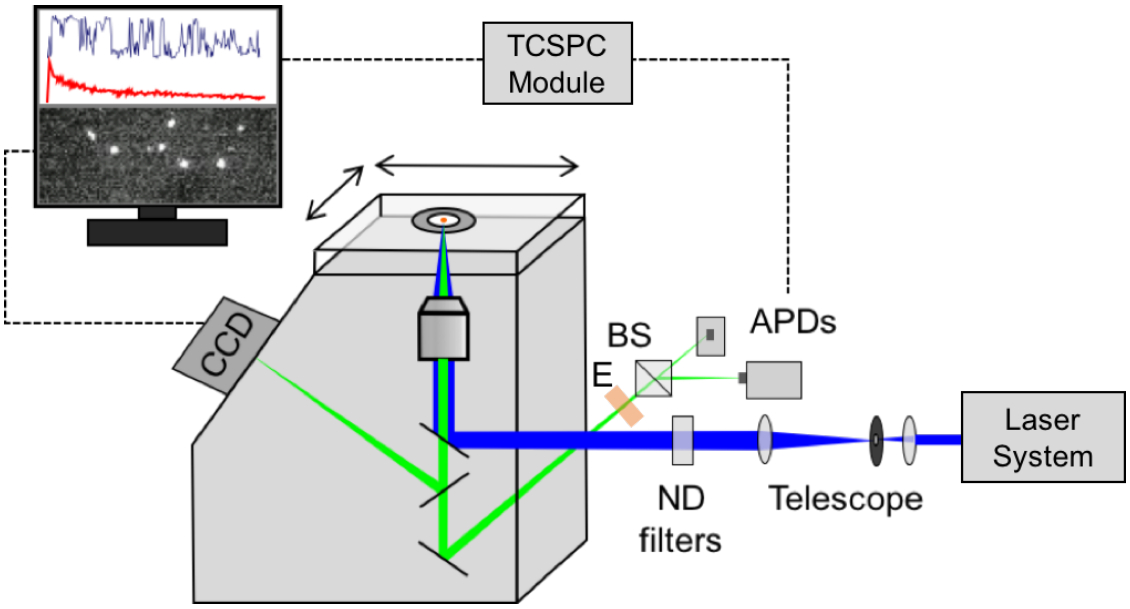

Figure 2.1: Schematic of experimental apparatus. CCD=charge-coupled device; TCSPC=time-correlated single photon counting; E=emission filter; BS=beamsplitter; APDs=avalanche photodiodes; ND=neutral density.

A single chiller (T255P, Coherent) cools the pump laser baseplate and Ti:Sapphire crystal holders in the oscillator and amplifier. The control units for the oscillator and amplifier are powered on at all times; this enables the entire laser system to be turned on/off with the chiller and pump laser power supply, both of which include RS-232 communication ports for remote operation.

The Verdi laser is used to pump the Ti:Sapphire crystal in the Mira oscillator and produce continuous wave (CW) lasing at a central wavelength of 800 nm. To create a pulsed output, passive modelocking is initiated by rapid cavity length changes (facilitated by a shaking glass plate butterfly), which leads to multiple longitudinal modes lasing simultaneously. This leads to high power fluctuations capable of producing an instantaneous high peak intensity (i.e., a pulse) that can initiate an optical Kerr effect in the crystal. The pulse then focuses and narrows from the Kerr lens and passes unattenuated through an aperture slit. Since a Kerr lens is only formed in the Ti:Sapphire crystal when the light intensity is sufficiently high, the beam diameter is reduced for high intensity modelocked pulses but not for the lower intensity CW beam. The slit clips the CW beam but allows a pulse to pass uninterrupted, which then experiences lower round trip losses than the CW beam and forms the dominant modelocked output. A 76 MHz pulse train is formed by sampling this circulating pulse using an output coupler. To achieve a sub-200 fs pulse width, negative chirp is introduced using a two-pass prism pair that compensates for the positive chirp introduced by self-phase mod-

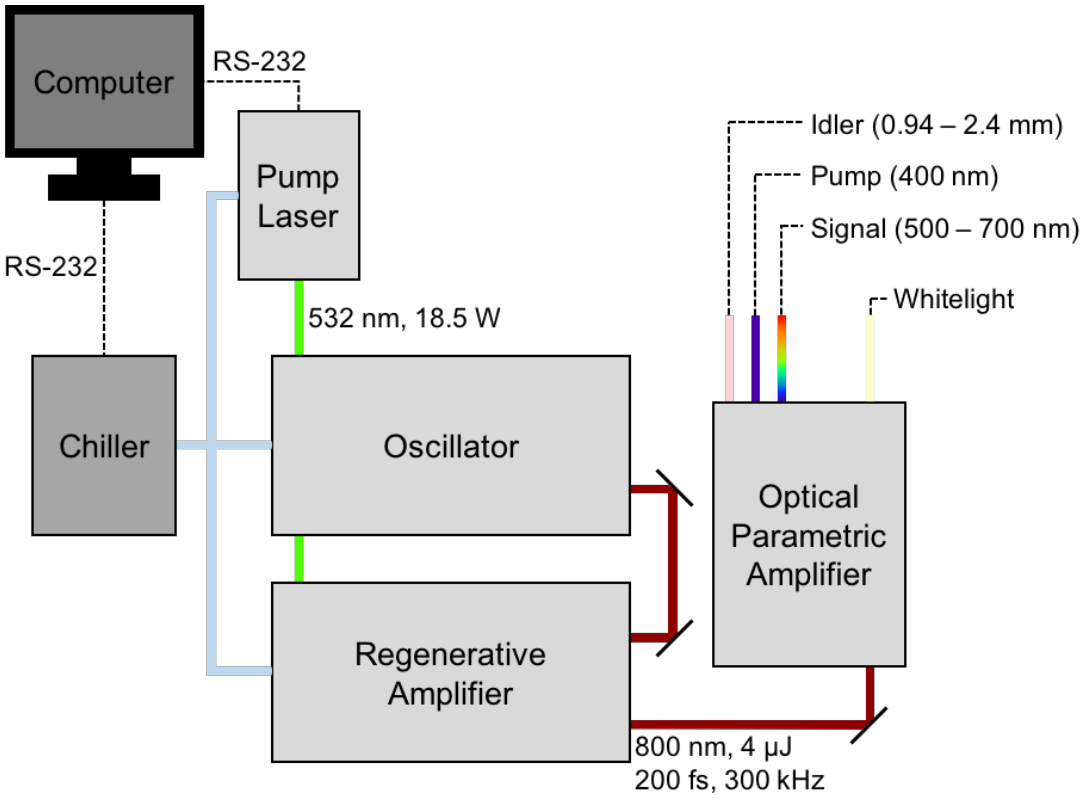

Figure 2.2: Schematic of the laser system layout. The output characteristics of the pump laser and amplifier are summarized, and the four outputs from the optical parametric amplifier are labeled.

ulation in the crystal and group velocity dispersion (GVD) in the various dispersive elements.

The Ti:Sapphire crystal in the RegA amplifier is also CW-pumped by the Verdi and seeded by the Mira. Two acousto-optic modulators facilitate the amplification of a single Mira pulse: a Brewster angled TeO_2 Q-switch and a Brewster angled TeO_2 cavity dumper (CD) plate, with acousto-optic transducers matched to respond to 80 MHz and 380 MHz RF excitation, respectively. When the Q-switch is turned on, it partially diffracts the cavity beam to hold off spontaneous lasing until the Ti:Sapphire crystal has built up the maximum stored energy. The Q-switch is turned off suddenly and the CD injects a single seed pulse from the oscillator into the RegA cavity. The single pulse is amplified over $\sim 19 - 25$ roundtrips through the crystal, reaches a maximum energy, and is ejected by the CD. The Q-switch is then turned back on, and the crystal allowed to store energy again for amplification of the next pulse. Since lasing builds up from the seed, the amplified Q-switched pulse inherits the pulse characteristics of the Mira; however, the Q-switch stretches each pulse to ~ 40 ps for safe energy extraction, introducing second and third order dispersion that must be corrected.

A single holographic grating four-pass pulse compressor is used for this purpose. A four-pass grating configuration compensates for the second order dispersion (i.e., positive GVD) while a compressor relay lens corrects for third order dispersion. Pulses are compressed back down to $150 - 200$ fs after being amplified about 400 times to 4 μJ. Figure 2.3 shows a characteristic spectrum of the RegA output centered at 800 nm, with a $\sim 9 - 14$ nm bandwidth, an average power of $1.1 - 1.2$ W, and a repetition rate of 300 kHz.

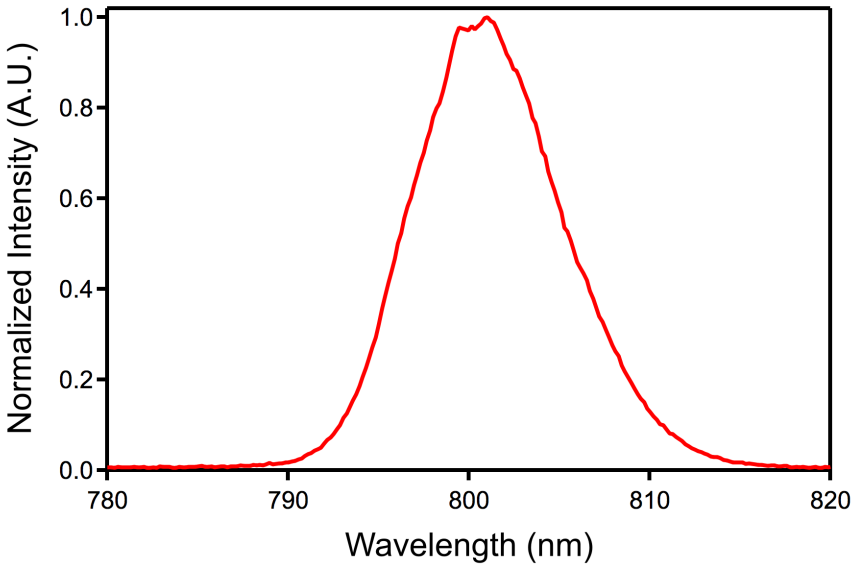

Figure 2.3: Characteristic output spectrum from the RegA amplifier, with a central wavelength at ~ 800 nm.

The RegA output is aligned into the OPA, where 75% of the beamline is used to produce 400 nm light via second harmonic generation in a 1 mm thick Type I β-barium borate (BBO) crystal, and 25% is used to generate a whitelight continuum via self-phase modulation in a 3 mm thick sapphire plate. A second 1 mm thick Type I β-BBO crystal is pumped by the 400 nm light and seeded by a portion of the whitelight signal to amplify the strength of the signal frequency, in a process called parametric amplification.

All three optical processes that occur in the OPA are nonlinear optical phenomena, meaning the medium to which an optical field is applied responds in a nonlinear manner to the strength of the field. At low field intensities, the induced polarization (dipole moment per unit volume) in a dielectric material, $P(t)$, can be approximated to be linearly proportional to the applied electric field, $E(t)$:

$$P(t) = \epsilon_0 \chi^{(1)} E(t) \tag{2.1}$$

where ϵ_0 is the permittivity of free space and $\chi^{(1)}$ is the linear or first-order susceptibility. At high intensities, this approximation is insufficient as higher order terms become relevant. The polarization can be expanded in a power series of the applied field strength:

$$\begin{aligned} P(t) &= \epsilon_0[\chi^{(1)}E(t) + \chi^{(2)}E^2(t) + \chi^{(3)}E^3(t) + ...] \\ &\equiv P^1(t) + P^2(t) + P^3(t) + ... \end{aligned} \tag{2.2}$$

where $\chi^{(2)}$ and $\chi^{(3)}$ are the second- and third-order nonlinear optical susceptibilities. The time-varying polarization components can act as sources of new components of the electromagnetic field, leading to the generation of radiation at new frequencies.[36] For example, in noncentrosymmetric crystals where $\chi^{(2)} > 0$, an incident electromagnetic field oscillating at a fundamental frequency w can generate a second-order polarization:

$$P^{(2)}(t) = 2\epsilon_0\chi^{(2)}EE^* + \epsilon_0\chi^{(2)}E^2\mathrm{e}^{-i2wt} + \epsilon_0\chi^{(2)}E^2\mathrm{e}^{+i2wt} \tag{2.3}$$

that leads to the radiation of an electromagnetic field oscillating at twice the fundamental frequency, $2w$. This frequency doubling process is called second-harmonic generation (SHG) and is represented schematically in Figure 2.4a. SHG can also be visualized as an instantaneous exchange of photons, as depicted in Figure 2.4b, where two photons of frequency w are destroyed while one photon of frequency $2w$ is simultaneously created. In the OPA, an SHG process is used to produce 400 nm light from 75% of the 800 nm fundamental input.

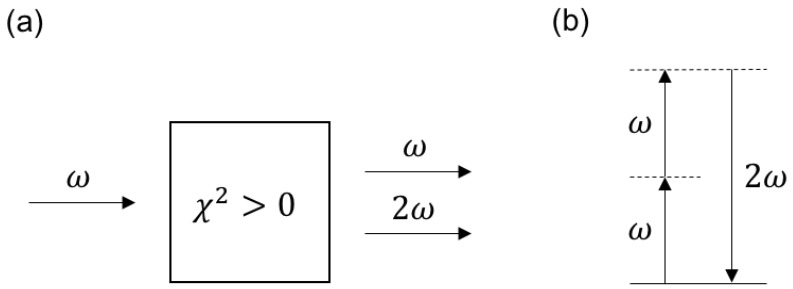

Figure 2.4: (a) Schematic of SHG interaction, and (b) photon exchange involved in SHG.

The remaining 25% of the fundamental is used to produce whitelight through self-focusing (SF) and self-phase modulation (SPM). In the presence of a third-order nonlinearity and high field intensities, the refractive index is represented as:

$$n = n_0 + n_2 I \tag{2.4}$$

where n_0 is the low-intensity, linear refractive index, I is the time-averaged intensity of the incident light, and the nonlinear refractive index term can be related to the third-order nonlinear susceptibility:

$$n_2 = \frac{3}{4n_0^2\epsilon_0 c}\chi^3 \tag{2.5}$$

A beam of high-intensity laser light passed through a material with $n_2 > 0$ induces a refractive index variation within the material, leading to a larger refractive index in the center than the edges and causing the beam to focus as if the material were a positive lens. This SF process is the same mechanism by which Kerr-lens modelocking occurs in the Mira oscillator. The SF collapse of the laser beam causes the refractive index to increase even further to the extent where SPM occurs. SPM changes the instantaneous phase of a pulse by an amount related to the nonlinear refractive index:

$$\phi_{NL}(t) = -n_2 I(t)\omega_0 L/c \tag{2.6}$$

which leads to a rapid frequency sweep from the IR (leading edge) to the UV (trailing edge). Due to the time response of the nonlinearity, the leading edge of the pulse does not experience SF or SPM as much as the trailing edge, resulting in a frequency conversion that favors shorter wavelengths. Schematics of the SF and SPM processes are shown in Figures 2.5a and b, respectively.

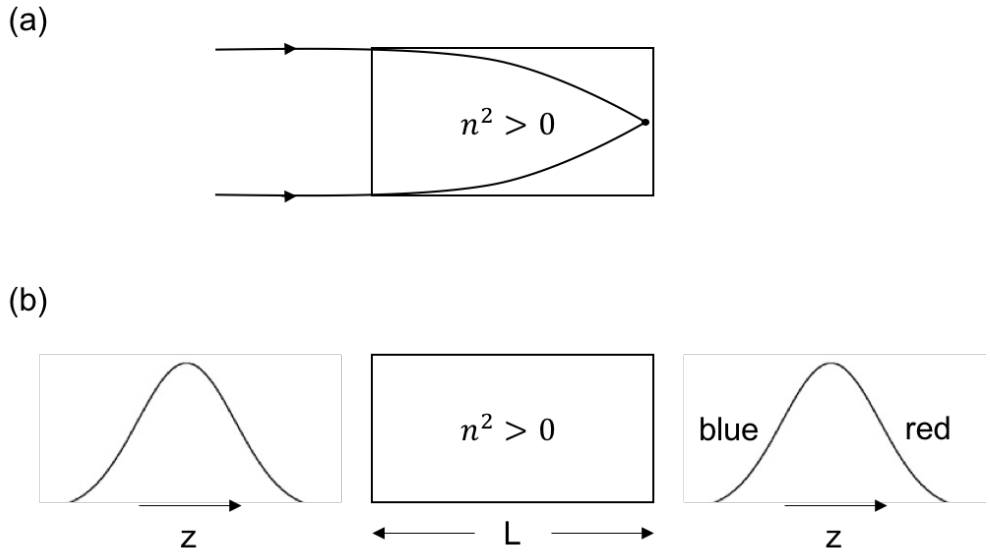

Figure 2.5: (a) Illustration of SF effect on the propagation of light. (b) Illustration of the frequency sweep caused by SPM.

The generated whitelight continuum is then mixed with the SHG light in another nonlinear crystal to amplify a frequency portion of the whitelight. This process is referred to as optical parametric amplification, which is an example of difference-frequency generation (DFG), the

nonlinear interaction of an optical field consisting of two different frequency components with a medium where $\chi^{(2)} > 0$. The second-order polarization that describes DFG takes the form:

$$P^{(2)}(w_3 = w_1 - w_2) = 2\epsilon_0 \chi^{(2)} E_1 E_2^* \tag{2.7}$$

In fact, four different frequency components are present in the nonlinear polarization created from two different incident frequencies; however, typically only one component will dominate based on phase-matching conditions.[36] In an OPA, the SHG beam is called the pump, w_p, and the portion of the whitelight that is overlapped with the SHG beam in the mixing crystal is called the signal, w_s. The nonlinear interaction generates a third frequency that corresponds to the difference w_p-w_s and is called the idler, w_i. The signal and idler waves increase in power at the expense of the pump. By tuning the portion of the whitelight continuum that overlaps with the SHG beam, the wavelength of the amplified signal can be tuned between $500 - 700$ nm and the idler between $0.94 - 2.4$ mm (see Figure 2.6). The tunable visible output from the OPA has a narrow bandwidth typically < 5 nm and an average power of $25 - 50$ mW, see Figure 2.7.

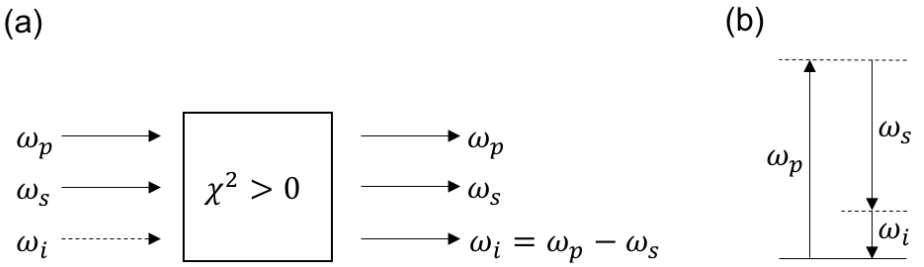

Figure 2.6: (a) Schematic of OPA interaction, and (b) photon exchange involved in OPA.

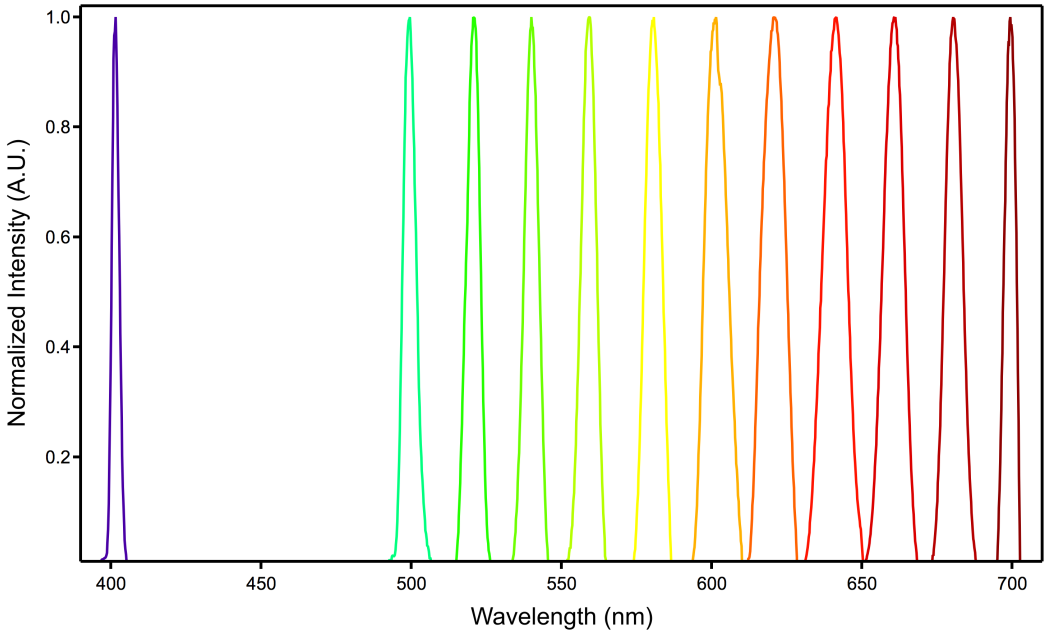

Figure 2.7: Example OPA output spectra, including SHG pump beam at 400 nm and tunable OPA signal beam from $500 - 700$ nm.

Technical Suggestions

(a) *Chiller Maintenance*

The chiller used in the laser system is a water-air chiller that couples directly to the Verdi baseplate. Given the large hose diameter and lack of a coupling barb, clogging in the baseplate chiller lines has not been an issue in this experimental setup. However, to cool the Ti:Sapphire crystals, smaller diameter hoses couple to the metal crystal holders via small metal barbs. A reduced, and in some cases negligible, flow rate through a crystal holder can occur if the barb is partially or completely blocked. The metal heat sink can no longer dissipate the heat effectively, leading to the holder and then the crystal heating up. The performance of the oscillator or amplifier would decrease, and irreversible damage to the Ti:Sapphire crystals could even occur. The chiller used (T255P, Coherent) has a flow rate of only ~ 0.3 L/min and typically cannot push past a clog at the barbs; therefore, a method for manual de-clogging at the barbs is required.

The temperature of the metal crystal holders is regularly checked, and if a holder is hot, the chiller and hose lines are emptied. The crystal holder hoses can be disconnected at the baseplate; note, this should be carried out with caution to avoid water contamination on the nearby optics. A wire can then be inserted and pushed through the hose and then the barb or just the barb if the hose is also clogged and needs to be cut. The use

of a pipecleaner, for example, to clean out the chiller hoses and push past a clogged barb, can be effective since it can be easily inserted through the hose and the fabric helps clean the inside of the hose. There is a risk of pipecleaner fabric coming off the wire and exacerbating the clogging issues, so this method is only carried out if flushing is not effective. To flush the hoses and push past any barb clog, a 5 mL syringe filled with distilled water is plunged into one hose end near the crystal holder, and the water is carefully collected out of the other. Repeated flushing in both directions is typically sufficient to clean dirty hoses and clogged barbs.

(b) *Remote Operation*

The T255P chiller and Verdi power supply can be turned on remotely via their RS-232 communication ports, decreasing wait-time for the laser system to stabilize before performing experiments. Terminal commands can be used directly (commands provided in the instrument manuals) or an instrument communication program such as Labview can be used. The computer desktop can then be accessed on a user's personal device using a remote desktop application.

(c) *Red Schott Glass*

When aligning the Mira or RegA, a $\sim$ 1 cm strip of red Schott glass is often used for visualizing the beam in place of a white card. The glass partially scatters 800 nm light, making the beam visible. More importantly, the glass will not burn at high powers (3 W is the highest average power obtained during alignment) like a white card. Appropriate protective laser eyewear should be worn and an IR viewer used to avoid the scattered reflections off the glass.

(d) *Pulse Width Reduction*

Short pulses are necessary to produce high peak intensities for pumping the OPA, but the excitation pulse width does not limit the instrument response function (IRF) of the setup described in this chapter. An autocorrelation to routinely measure and reduce the pulse width is therefore unnecessary. Instead, the quality of the whitelight and the power of the SHG out of the OPA are used as proxies for pulse width. The white central portion of the whitelight should be minimized in size and appear as white as possible and not yellow. A concentric, rainbow pattern around the whitelight, predominantly appearing as blue and red coronas, should also be visible. This is referred to as conical emission and has been theorized to be due to four-wave mixing or from spatial SPM during continuum generation.[37]

(e) *Simple OPA Alignment*

OPA alignment using the alignment tools is typically not necessary. Instead, the first pass of the whitelight through the mixing crystal is directed out of the OPA and onto the center of a target. A small amount of SHG leaks through the second dichroic mirror; by blocking the whitelight, this can be seen and aligned onto the target. Then with the

mixing crystal angle and first pass delay stage set for the same wavelength, the delay stage is adjusted until a flash of amplified signal is seen (580 and 530 nm work well for this purpose). If no flash is observed, a short focal length lens can be placed in front of the first pass signal to expand the beam. A small change in color or structure of the beam due to the emergence of an amplified signal can now be visualized more easily with the expanded beam. The same process can be carried out for the second pass signal at the output of the OPA.

(f) *Beamwaist Measurement*

Section 2.1.2 explains why the beamwaist of the excitation laser should be equal to or larger than the objective back aperture. A measurement of the beamwaist is helpful to ensure it is sufficiently expanded for overfilling the objective; it is also useful for calculating the power transmitted through the objective aperture if a short working distance objective makes measuring the transmitted power difficult. The equation used to calculate the power of a Gaussian beam transmitted through a circular aperture is:

$$P(r,z) = P_{0,z}(1 - \exp^{-2r^2/w(z)^2}) \tag{2.8}$$

where r is the aperture radius and $w(z)$ is the Gaussian beam radius (referred to as the beamwaist here) where the intensity falls to $1/e^2$ of its peak value. This equation can be used to calculate the power transmitted through the objective once the Gaussian beamwaist is known. It can also be taken advantage of to actually measure the beamwaist, by measuring the power of an incident beam through apertures of known radii. A useful way of doing this in practice is by closing an adjustable iris down over drill bits of precisely known diameters. A series of $5-6$ drill bits is sufficient to obtain a good fit to Equation 2.8, and extract an experimental value for $w(z)$. Figure 2.8 provides an example of a curve fitting procedure to experimentally measured $P(r,z)$ and r values.

2.1.2 Widefield and Confocal Fluorescence Microscope

The tunable output or the 400 nm output of the OPA is aligned into a Keplerian telescope with a pinhole at the focus of the first lens. The telescope is used to expand the excitation beam so that the back aperture of the objective can be overfilled and a near diffraction-limited resolution achieved. In a plane perpendicular to propagation (z axis), the laser beam has a Gaussian intensity distribution, $I(r,z) = I_{0,z}\exp^{-2r^2/w(z)^2}$, where r is the radial coordinate and $w(z)$ is the Gaussian beamwaist. In contrast, the profile of a light source directed into an objective would ideally be that of a plane wave, with constant illumination intensity in the transverse direction. This is because the diffraction-limited resolution of an objective depends on its numerical aperture (NA), $res_{x,y} = \lambda/2NA$ and $res_z = 2\lambda/NA^2$, where the NA rated by the objective manufacturer is based on an incident plane wave. The lower edge intensities of a Gaussian profile lower the effective NA of the objective, decreasing the transverse and axial resolutions. The Gaussian laser beam is therefore expanded to overfill

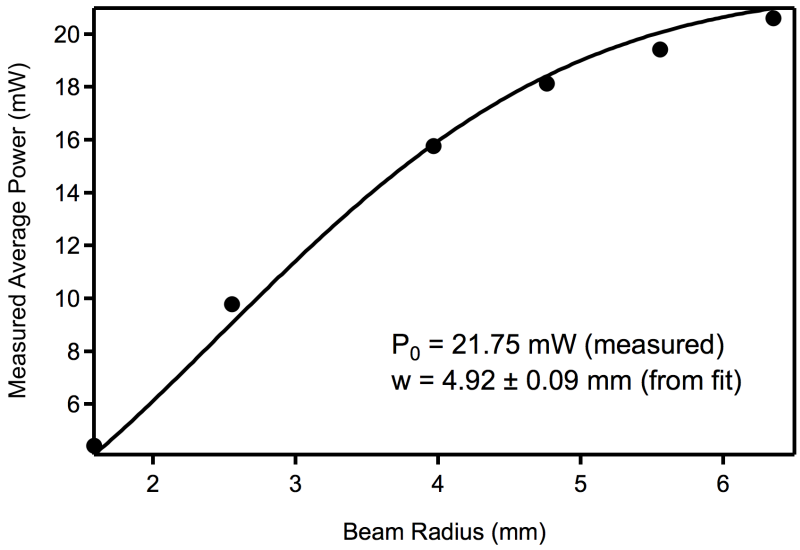

Figure 2.8: Curve fitting to power transmitted through a circular aperture data to extract a measurement of the Gaussian beamwaist.

the objective aperture so that only the central, relatively flat portion of the beam (within the $1/e^2$ beamwaist) is focused through the objective. An experimental method for measuring the beamwaist is presented in Section 2.1.1.

The power of the excitation source transmitted through to the sample is reduced when the objective back aperture is overfilled, but given the low excitation powers required for these experiments (nW range), this is not problematic. Figure 2.9 shows the Gaussian profiles for four different overfill factors, $F = w(z)/r$, for a $r = 2$ mm aperture. This corresponds to the radius of the back aperture of the primary objective used in the experiments described here. As the size of the beamwaist relative to the aperture is increased, the beam profile of the transmitted light flattens out and becomes more plane-wave like. For example, the edge intensity of a beam with $F = 1$ is 14% of the maximum intensity; this is compared to a $F = 4$ beam that has an edge intensity that is 88% of the maximum. In the experiments described here, an F value > 2 is deemed reasonable ($w(z) > 4$ mm, see Figure 2.8).

The expanded laser beam is aligned by a periscope into the back entry port of an inverted Olympus IX71 microscope, which is used in an epifluorescence scheme. The excitation light is reflected from a dichroic mirror - a longpass filter at a 45° angle of incidence - and focused onto the sample by an objective. An optically excited nanoparticle emits isotropically, and a portion of the PL is back-collected by the same objective. The red-shifted PL passes through the dichroic and is directed towards a detector. Additional longpass and bandpass filters are used to further eliminate any residual excitation light as well as any other light outside

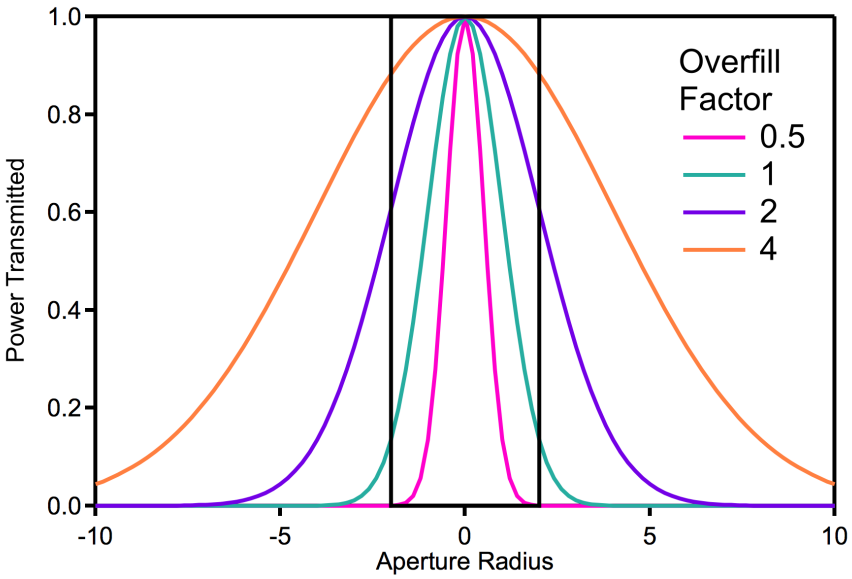

Figure 2.9: Gaussian profiles of beams with four different beamwaists, labeled by overfill factor. The black rectangle represents a $r = 2$ mm radius aperture, and the curves within the rectangle represent the portion of each Gaussian beam that would be transmitted through the aperture.

the desired emission regime. Widefield or confocal microscopy can be used, depending on the application. A widefield configuration is used to image a large sample area at once, which is useful for collecting the PL from many isolated nanoparticles simultaneously, or for illuminating a single large particle. A large focal spot size is achieved by focusing the excitation beam onto the back aperture of the objective to significantly underfill the aperture and decrease the resolution, see Figure 2.10a. In Chapters $3-4$, a widefield scheme using a charge-coupled device (CCD) (EXvision, Super Circuits) is used to determine and set the focus of the objective to the sample plane (i.e., find the nanoparticles), and manually move the sample stage to an area of the substrate that has a good coverage of dispersed particles without any obvious aggregates. A confocal scheme, as described below, is then used for data acquisition. In Chapter 5, widefield microscopy is also used for data acquisition to ensure complete illumination over isolated nanowires that have lengths > 10 μm.

In confocal microscopy, the expanded and collimated excitation beam overfills the back aperture of the objective, and near diffraction-limited resolution is accomplished. Another key difference from widefield microscopy is the use of excitation and emission pinholes to eliminate out-of-plane fluorescence and increase the SNR. The pinhole in the expanding telescope (150 μm diameter) serves as the excitation pinhole, whereas the apertures of the detectors (50 μm diameter) used for confocal measurements (described in Section 2.1.4) act as the emis-

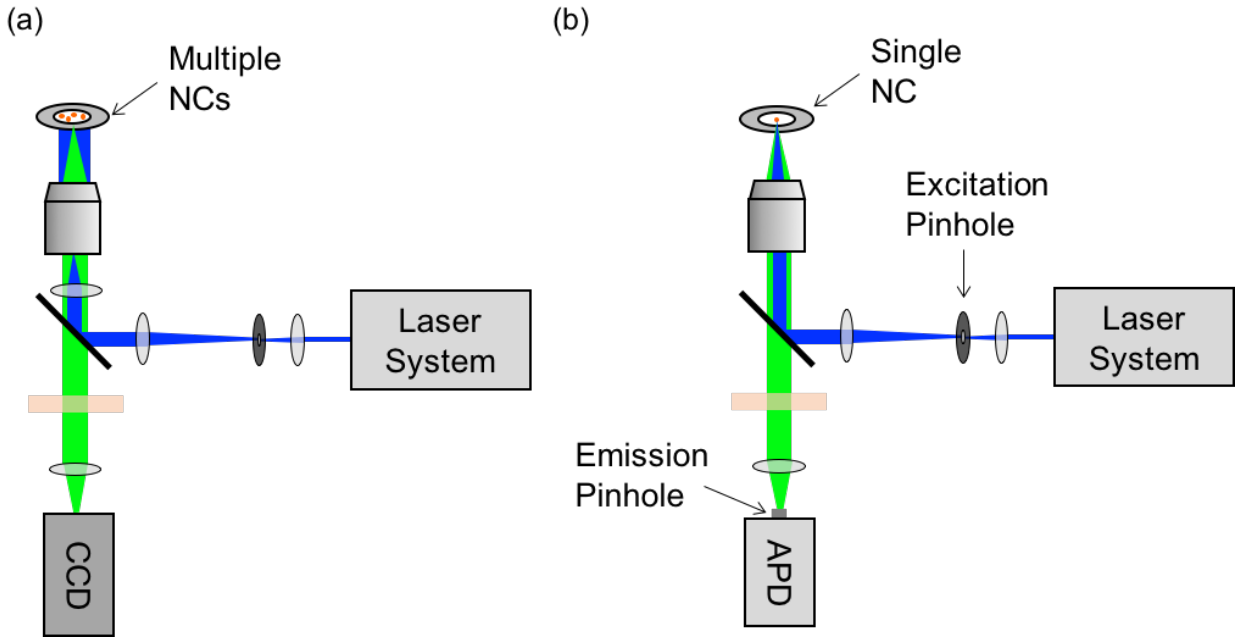

Figure 2.10: (a) Schematic of widefield microscopy configuration where the excitation beam is focused onto the objective back aperture. (b) Schematic of confocal microscopy configuration where the excitation beam is collimated towards the objective back aperture.

sion pinholes. Any PL signal that originates from a focus above or below the sample plane will not be aligned through the emission pinhole and is thus eliminated. This configuration is effective in decreasing the noise from background fluorescence, and as such, it is used to collect PL from a single particle when the highest SNR possible is optimal. In addition to the manual stage used for coarse alignment, the microscope is equipped with a 2D piezoelectric scanning stage (PI 517, PI) for scanning up to a 100 μm area, and piezoactuators (AE0505D16F, Thorlabs) driven by a single-axis piezo controller (MDT694A, Thorlabs) for optimizing the Z-focus. Isolated particles can be found with a raster scan, and the PL from a single particle can then be collected by repositioning the stage on the particle of interest. A schematic illustrating a confocal microscopy scheme is shown in Figure 2.10b.

In the subsequent chapters, the primary objective used is an oil immersion objective with a magnification of 100× and a numerical aperture (NA) of 1.3. Low autofluorescence immersion oil (refractive index n=1.518) is added to the front lens cover of the objective to match the refractive index of the objective glass (n $\sim$ 1.5) to the substrate (n $\sim$ 1.5, described in Section 2.1.3), rather than the lower-index of air (n $\sim$ 1) in the surrounding medium. This prevents refractive scattering of the excitation and emission light.

2.1.3 Single Particle Sample Preparation

The microscopy setup described in Section 2.1.2 requires a dilute concentration of particles to be dispersed on an appropriate substrate and mounted to the scanning stage above the objective. As the back side of the substrate faces the objective and the particles are dispersed on the front side, to separate the particles from the immersion oil, the substrate used must be optically transparent at the relevant wavelengths. The substrate must also have a thickness that matches the working distance of the objective; the excitation light can then be focused through the substrate to the particles, with the immersion oil spreading out on the back side of the substrate. UV-grade fused silica coverslips with high UV and visible transmission, and a 170 μm thickness that matches the working distance of the 100×, 1.3 NA objective, are ideal substrates. The refractive index of the coverslips used, n=1.470 at 400 nm, is slightly lower than the immersion oil and objective front cover, but is sufficient for these experiments.

To clean the coverslips prior to use, they are first submerged in a 1% solution of a glass cleaning detergent (Hellmanex II) in millipore water and sonicated at 80°C for 30 min. After being rinsed with millipore water, the coverslips are then submerged and sonicated for an additional 30 min at 80°C in millipore water. A final rinse and the coverslips are dried using nitrogen, rinsed with the same solvent to be used for the nanoparticle dilution solutions, and dried again with nitrogen. Nanoparticle solutions are made by subsequent dilutions of a stock solution with the desired solvent, typically to picomolar concentrations. A dilute solution is then drop-casted or spin-casted onto a clean coverslip, followed by a solvent rinse, and gentle drying with nitrogen or heat.

2.1.4 Detectors for Time-Resolved and Spectral Measurements

For time-resolved measurements, the emission PL is focused onto two avalanche photodiodes (APDs) (PDM-50, Micron Photon Devices) using short focal length lenses. APDs are photodiodes operated at high reverse bias voltages, just above the Zener breakdown, such that a large internal electric field develops across the depletion region. When free carriers are created from the absorption of photons, they are strongly accelerated in the electric field and undergo high-energy collisions with neutral atoms. This results in the generation of secondary carriers in a process called impact ionization. The secondary carriers are likewise accelerated in the strong electric field and can undergo further impact ionization. The resultant gain of this avalanche effect renders APDs capable of detecting low light levels, down to single photon counts, making them ideal detectors for single particle experiments. The APDs are mounted on three-axes manual micrometer stages for facile alignment, and separated by a 50/50 non-polarizing beamsplitter. The purpose of using two identical APDs is explained in Section 2.3.1.

For the spectral measurements described in Chapter 5, the emission PL is directed to a

monochromator (Spectro Pro-300i, Acton) with a liquid nitrogen CCD (7346-0001, Roper Scientific) cooled to 77 K. A 1200 grooves/mm grating with a 300 nm blaze angle provides a spectral resolution of 0.06 nm.

2.2 Data Acquisition

This section provides an overview of the data acquisition procedures for the experimental setup described in the preceding section. Section 2.2.1 describes the alignment and characterization of the laser excitation source, while Section 2.2.2 gives an overview of the single photon counting technique used.

2.2.1 Alignment and Characterization

The chiller is first turned on and allowed to stabilize at 18.5°C. This can be completed remotely, as can the following step - powering on the pump laser. After a short warm-up time ($\sim$ 1 hr), the Mira, RegA, and OPA are sequentially optimized:

(a) *Mira Optimization*

The modelocked output power is maximized using the pump and end mirrors. If the Mira is not modelocked, the CW power is instead maximized, then modelocking procedures are followed. If the output power is too low and the optics have not been cleaned recently, the optics are cleaned with anhydrous methanol. The temperature of the Ti:Sapphire crystal holder is checked and the chiller hoses and barbs flushed if the holder is hot (see Section 2.1.1). If the power is still too low, the Mira is realigned.

(b) *Rega Optimization*

The output power is maximized using the pump mirrors, the injection and ejection timing controls are adjusted to maximize the power and optimize the seed pulse build-up (injection) and dumping (ejection), and the Mira seed is aligned for optimal overlap. Iteration through these steps is carried out. If the output power is too low and the optics have not been cleaned recently, the optics are cleaned with anhydrous methanol. The temperature of the Ti:Sapphire crystal holder is checked and the chiller hoses and barbs flushed if the holder is hot (see Section 2.1.1). If the power is still too low, the RegA is realigned.

(c) *OPA Optimization*

The whitelight is optimized by iterating between the RegA compressor grating position and the beam steering into the OPA. The SHG pump power is optimized during grating positioning and by rotating the SHG BBO crystal angle to achieve optimal phase-matching conditions. The OPA signal power at the desired output wavelength is then

maximized by rotating the OPA BBO crystal angle to achieve optimal phase-matching conditions, and tuning the first- and second-pass delay stages.

Once the laser system is optimized, the OPA output beam is aligned through the telescope and into the microscope. The beamwaist is measured (described in Section 2.1.1) if any changes to the optical path occurred since the previous measurement. The average power, P_{avg}, is measured just before the microscope using a power meter with a minimum power detection limit and resolution in the nW range (OP-2 VIS, Coherent). The actual power transmitted through to the sample plane is calculated using Equation 2.8 and the beamwaist measurement. Two variable neutral density filters are used to adjust the excitation power as needed. If the beamline into the microscope needs to be aligned, a tube lens with an iris target replaces the objective and an iris is placed at the back entry port. When the beamline is aligned through both irises, the beam will be appropriately centered through the objective.

The full-width-at-half-maximum (fwhm) laser beam area of the focal spot is determined by taking a small scan ($\sim 1-2$ μm) of a single particle. A cross-section of the particle PL yields an intensity profile that can be fit to a Gaussian distribution. The fwhm diameter is related to the Gaussian beamwaist by $2w(z) = \frac{\sqrt{2}D_{fwhm}}{\sqrt{\ln 2}}$, and the spot size area is then calculated as $A = \pi D_{fwhm}^2/4$. The excitation intensity at the sample plane is equal to $I_{ex} = (P_{avg} \times P_{loss})/A$. An example measurement is demonstrated in Figure 2.11. Note, if the particles of the sample to be measured are not bright or stable enough for spot size calculations, micron-sized fluorescent beads are used for this purpose instead. Often the average number of excitons excited per pulse is an important experimental parameter. This can be calculated using the characterization measurements detailed above as well as a few additional parameters: $\langle N_{ex} \rangle = \ln 2 \times \frac{I_{ex}\,\sigma_{abs}}{E\,\Gamma_{rep}}$. Γ_{rep} is the laser repetition rate, E is the photon energy of the excitation light, and σ_{abs} is the absorption cross-section of the sample.

With the excitation source aligned and excitation conditions characterized, a 100 μm raster scan is completed using the scanning x-y piezo stage. The SNR of the nanoparticles is maximized through small Z-adjustments to the focus and filtering of the emission directed to the APDs. The stage is centered at each particle of interest and a technique called time-correlated single photon counting (TCSPC) is used to acquire PL data.

2.2.2 Time-Correlated Single Photon Counting

TCSPC is a powerful tool used to record the arrival times of individual photons. A repetitive, precisely timed signal, such as an excitation laser pulse train, is used as a timing reference; in the experiments described here, a 5% pick-off signal from the RegA is sent to a photodiode for the timing reference. Each pulse can be thought of as a start button on a stopwatch. The electronic response of a detector (e.g., an APD) due to the detection of a fluorescence photon then acts as the stop button. Each start-stop time difference is measured by fast electronics and corresponds to a single shot detection event. By accumulating start-stop times

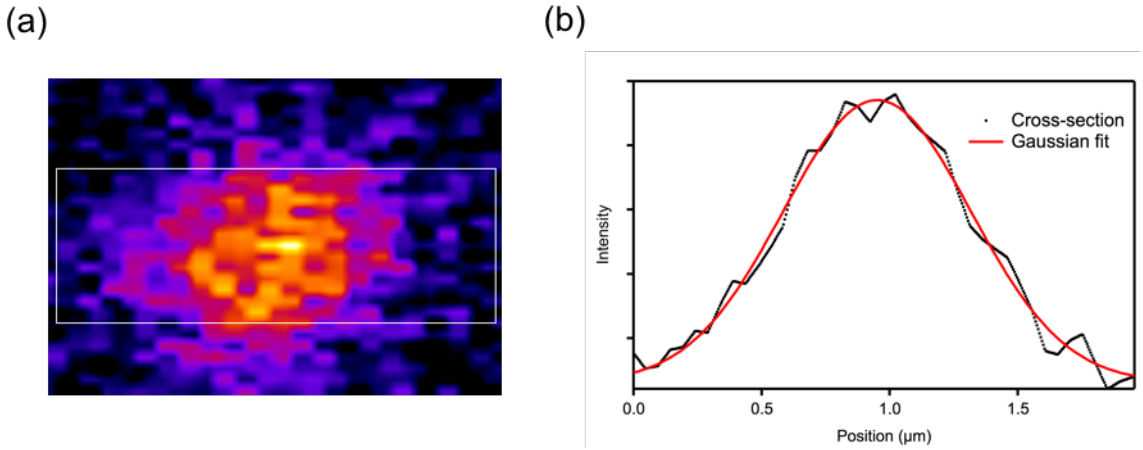

Figure 2.11: Excitation focal spot size measurement. (a) Small confocal scan of a single particle. (b) The cross-section profile (black) from the selection in the white rectangle in (a), fit to a Gaussian distribution (red).

over many excitation and emission cycles and constructing a histogram of all the single shot times, excited state decay lifetimes can be extracted.[38] These microscopic start-stop times are labeled as microtimes (t_1, t_2) in Figure 2.12. It is also possible to record the macroscopic arrival times of each photon with respect to the beginning of an experiment. These times are depicted in Figure 2.12 as macrotimes, which can be used to reconstruct a PL trajectory over time.

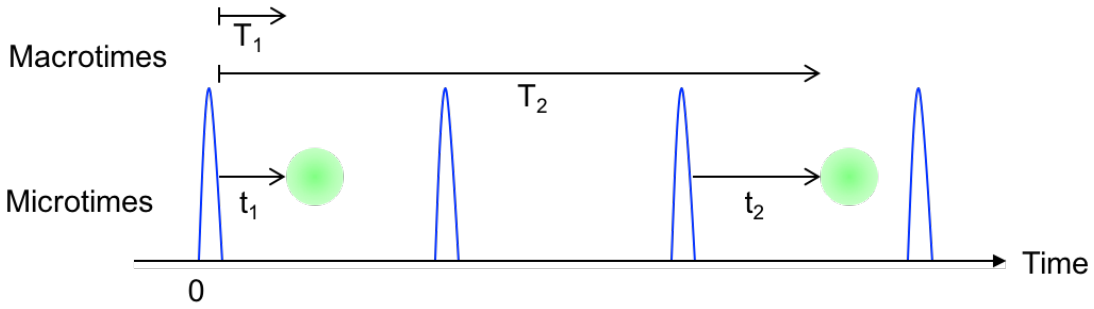

Figure 2.12: Schematic of start-stop microtimes and macrotimes recorded in a typical TCSPC measurement.

The TCSPC module used in this experimental setup (PicoHarp 300, PicoQuant) has two channels, one for the response signal and one for the synchronization signal (timing reference). To record simultaneous measurements from more than one detector, a four channel router (PHR 800, PicoQuant) is used in conjunction with the TCSPC module. The laser intensity

is adjusted so that the probability of detecting one photon per excitation pulse is low. This ensures that no photon absorption events are missed within the dead time of the detectors.

2.3 Data Analysis

The final section of this chapter summarizes the data analysis carried out to extract meaningful information from the collected raw data. By using the TCSPC technique to time-tag every single detected photon, measurements of second-order photon correlations, time-resolved PL, and PL trajectories can be obtained simultaneously. Section 2.3.1 presents an overview of a second-order photon correlation, Section 2.3.2 describes time-resolved PL decays, and Section 2.3.3 summarizes two methods for analyzing PL trajectories.

2.3.1 Photon Correlation

The use of two identical APD detectors in the experimental setup described here is for the purpose of measuring the second-order correlation function, $g^2(t, t+\tau)$:

$$g^2(t, t+\tau) = \frac{P_2(t, t+\tau)}{P_1(t)P_1(t+\tau)} \tag{2.9}$$

where $P_2(t, t+\tau)$ is the joint probability for photon counts on one detector at time t and the other detector at time $t+\tau$, normalized by the probability for two independent counts.[39] By measuring the coincidental photon counts at both detectors with a time difference τ, a histogram of coincidence counts versus τ can be obtained. The behavior of this $g^2(\tau)$ histogram, in particular at a $\tau = 0$ time delay, reveals the nature of the light source. For a coherent light source such as a laser, the emitted photons follow Poissonian statistics and $g^2(\tau) = 1$ for all τ. Classical light from thermal sources or an ensemble is emitted in photon bunches where $g^2(\tau) \geq 1$ and $g^2(0) \geq g^2(\tau)$. A single quantum emitter, in contrast, cannot emit two photons arbitrarily close together in time since a finite amount of time is required for the emitter to relax from its excited state to ground state (dictated by the excited state lifetime, usually on the order of nanoseconds).[17] This is referred to as photon antibunching and it is characteristic of light that has sub-Poissonian statistics. As the time delay approaches zero, corresponding to the simultaneous detection of photons on both detectors, $g^2(0) = 0$. This is true for the case of a single photon state, but more generally, $g^2(0) = 1 - 1/n$, where n is the photon number state. A single photon state (i.e., a single exciton state in a semiconductor NC) with $n = 1$ results in $g^2(0) = 0$ as stated above. A double photon state (i.e., a biexciton state) with $n = 2$ results in $g^2(0) = 0.5$; however, this assumes that every double photon state emits two photons. In NCs, Auger nonradiative decay of a biexciton state is very efficient and occurs orders of magnitude faster than the radiative decay of each exciton. Therefore, $g^2(0) = 0.5$ can be considered the maximum attainable value for a single particle, and particles with $g^2(0) > 0.5$ can be neglected from further analysis.

The time delay between excitation pulses of the laser system used here (3.4 μs) is orders of magnitude longer than the average delay between an excitation pulse and an emitted photon (ns). As a result, a coincidence count histogram will show peaks spaced by the laser period, with a small or negligible peak at time zero if the particle is a single emitter, as shown in Figure 2.13. One detector would be sufficient for a correlation measurement if the detector dead time were much shorter. Typical of any APD, the detectors used here have a dead time of 77 ns, preventing the detection of multiple photons within < 77 ns on the same detector. A Hanbury Brown-Twiss setup is used instead where the emission photons are split using a 50/50 beamsplitter onto two APDs (or more generally, any photo-sensitive detectors) and a cross-correlation between the two detectors is carried out (Equation 2.9).[40]

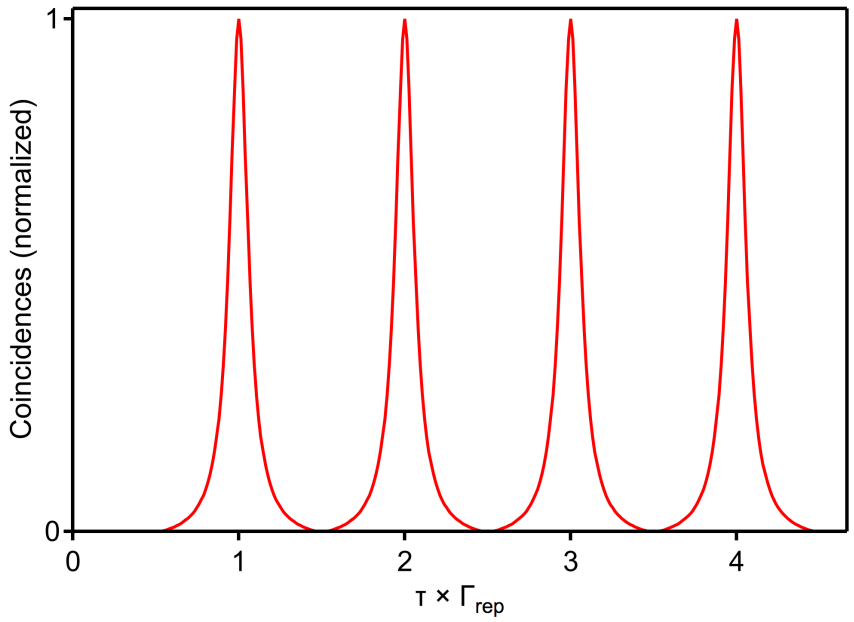

Figure 2.13: Schematic of antibunching effect measured by a second-order photon correlation.

2.3.2 Time-Resolved Photoluminescence

A histogram of the accumulated microtimes described in Section 2.2.2 is called a time-resolved PL (TRPL) measurement. A TRPL trace captures the kinetics of an excited state decaying back to a ground state. For example, a single decay rate from one initial state to a final state would result in a TRPL intensity ($I(t)$) decay that follows a single exponential:

$$I(t) = I_0 \mathrm{e}^{-t/\tau} \tag{2.10}$$

where I_0 is the intensity amplitude at $t = 0$ and τ is the lifetime, the average time of an excited state. The lifetime is the inverse of the total excited state decay rate, i.e., the sum of

all rates that depopulate the excited state.[19] This could, for instance, include the radiative decay rate, Γ_{rad}, as well as numerous pathways for nonradiative decay, k_{nr}:

$$\tau = \frac{1}{\Gamma_{rad} + \sum k_{nr}} \tag{2.11}$$

$$I(t) = \sum_{i=1}^{n} \alpha_i \mathrm{e}^{-t/\tau_i} \tag{2.12}$$

A monoexponential decay is only observed when one excited state decays directly to the ground state at a rate that does not fluctuate over time. Multiexponential decay, see Equation 2.12, is often observed and can arise from several different sources. A multiexponential decay observed for an ensemble of nanoparticles could be due to three possible causes: (a) the ensemble is heterogeneous and monoexponential lifetimes differ between particles in the ensemble, (b) the decay process is multiexponential for each individual particle, or (c) the decay for each particle is instantaneously monoexponential but fluctuates over time.[41] A lifetime measurement of a single nanoparticle is extremely valuable since it allows the cause of ensemble multiexponential decays to be ascertained. It should be noted that a single nanoparticle TRPL measurement time-averaged over the entire TCSPC measurement time cannot distinguish between cases (b) and (c) above. A multiexponential TRPL decay in a single NC has been attributed to fluctuating nonradiative rates leading to fluctuating monoexponential lifetimes that when averaged over time result in a multiexponential lifetime.[41] Conversely, the fast decay time in biexponential decays of single NCs have also been assigned to the decay of multiexcitons.[42]

2.3.3 Analysis of Photoluminescence Trajectories

A plot of the macrotimes described in Section 2.2.2 will result in a PL trajectory. As introduced in Chapter 1, the PL trajectories of single NCs display macroscopic fluctuations that can be investigated to infer mechanistic information about the underlying charge carrier dynamics. To extract kinetic information, a PL trajectory can be separated into a series of bright (on) and dark (off) durations, which can be accumulated into probability distributions. To deal with the Poissonian counting noise of the raw photon arrival times, the macrotimes can be averaged together in time bins typically between $1 - 100$ ms. A PL trajectory with a higher SNR is then produced, which can be separated into intensity levels by applying a threshold level to the trajectory, see Figure 2.14. There are several methods for selecting a threshold level. One approach involves constructing a histogram of the PL intensities, from which a center threshold value can be selected (either by visual inspection or through a more rigorous fitting of the peaks to Gaussian distributions).[43] Another approach is to set the threshold equal to $1 - 3$ standard deviations above the average intensity of the lowest intensity state.[30] Regardless of the type of threshold set, this is referred to in this work as the bin and threshold analysis method.

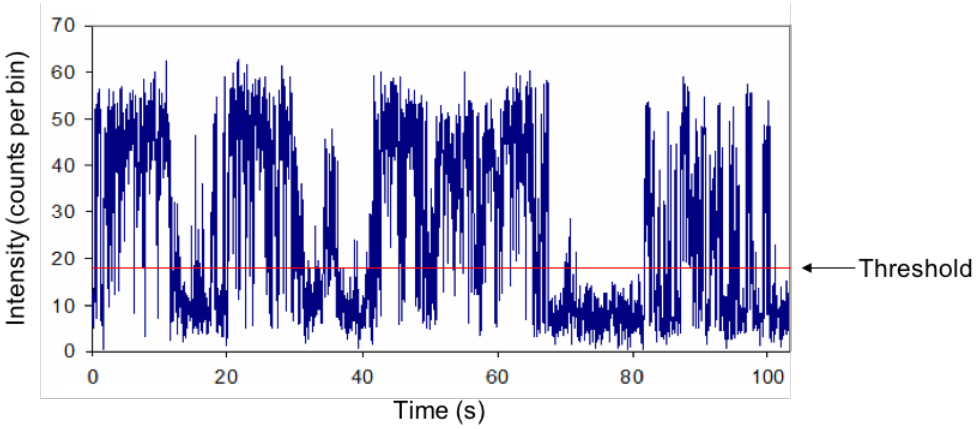

Figure 2.14: Binned PL trajectory separated into two intensity levels by a set threshold.

Once a threshold has been set, the PL trajectory can be sorted into on and off durations, and histograms of the frequency of durations can be obtained. These probability distributions can be weighted by the average time difference to the next longest and shortest durations, in order to take the limited measurement time into account.[27] This results in probability distribution densities:

$$P(\tau_i) = \frac{2N_{\tau,i}}{(\tau_{i+1} - \tau_i) + (\tau_i - \tau_{i-1})} \tag{2.13}$$

that can be plotted versus the on and off durations to yield important kinetic information about the charge carrier dynamics.

The bin and threshold method for analyzing PL trajectories is a simple and fast method that is most commonly used in the field. However, due to several issues that arise from binning photon counts and manually selecting a threshold, several other analysis methods have been developed to process TCSPC photon arrival times. One such method, called changepoint analysis, provides a quantitative and statistically robust way of accounting for every photon count recorded. The number and location of intensity changes can be found, and a PL trajectory consisting of a statistically determined number of intensity levels, that is free of time binning, can be reconstructed. Probability distributions for each intensity level can be extracted and further analyzed in the same manner as distributions extracted using the bin and threshold method. The changepoint analysis method is described in more detail in Chapter 3, where it provides a further functionality of eliminating the commonly used assumption that a PL trajectory of a single NC consists of only two states.

Chapter 3

Using Changepoint Analysis to Understand the Bias in Traditional Analysis Methods of Photoluminescence Blinking in Nanocrystals

3.1 Summary

The photoluminescence (PL) intermittency of single CdSe/CdS nanocrystals (NCs) with different shell sizes is studied using the conventional bin and threshold method and the statistically more rigorous method, changepoint analysis (CPA). The on-state truncation time (τ_c) is a critical value used to interpret the dynamics of charge trapping in single NCs; however, changing the bin size and threshold in PL trajectories significantly modifies τ_c. Herein, the CPA method is used to minimize the bias that binning and thresholding introduces. 12 out of 17 NCs are observed to exhibit more than two intensity levels and the τ_c values of individual levels are found to differ from the values obtained when the levels are combined, i.e., when one assumes there is only one on and one off state as in the conventional bin and threshold method. For instance, one NC has τ_c values of 0.5 (0.1) and 2.0 (0.2) s from two different intensity levels, whereas when the levels are combined into only one on state, τ_c is found to be 7 (1) s. The CPA method is found to be more suitable for studying

multilevel emission in NCs than the conventional bin and threshold method.

3.2 Introduction

There have been a substantial number of studies regarding the fluctuations of emission intensity, known as photoluminescence (PL) intermittency or blinking, in single colloidal semiconductor nanocrystals (NCs), and various models describing the underlying charge carrier trapping kinetics of PL blinking have been proposed.[30,44,45] To analyze blinking in NCs, a time series of emission intensities, referred to here as a PL trajectory, is constructed traditionally by binning the arrival times of emitted photons and setting a threshold to distinguish on and off states. Probability distributions for durations of on states and off states can then be obtained. Studies have shown that the probability distributions ($P(\tau_i)$) of the on and off time durations follow an exponentially truncated power law, $P(\tau_i) \propto \tau_i^{-\alpha} e^{\tau_i/\tau_c \text{ or } \tau_d}$, where blinking frequency can vary over 6 orders of magnitude in time.[26,46] A truncation time or the time constant corresponding to rapid fall-off from power-law behavior is observed for both on (τ_c) and off (τ_d) probability distributions, and the power-law exponent (α) is typically observed to be less than 2.[47]

Although the bin and threshold analysis is the most commonly used method for evaluating the kinetics of blinking in NCs, recent papers have raised the point about its unavoidable bias.[43,48–50] In this method, binning is necessary to reduce Poisson counting noise and to isolate emission states; however, the choice of bin time introduces an artificial time scale to the measurement, and depending on the bin time, certain information can be lost or favored. For instance, a longer bin time is incapable of detecting fast events whereas a shorter bin time prevents an accurate separation of emission states.[48] According to the work of Crouch et al., changing the bin size from 1 to 100 ms was shown to increase the on-state truncation time from 0.6 (0.1) to 1.2 (0.4) s in one sample NC.[43] One approach to address this issue is to directly incorporate photon binning into blinking models,[51,52] but since this approach must be carried out within each individual model, its broad applicability is restricted. Rather than requiring theoretical models to incorporate externally imposed time scales into detailed kinetic schemes, another strategy would be to process photon arrival times via a bin-free, model-free analysis method. Toward this goal, Watkins and Yang developed a quantitative and statistically robust method called changepoint analysis (CPA).[48]

Unlike binning and thresholding where the probability distributions are derived from averaging the number of photons, CPA accounts for every photon count recorded. In the CPA algorithm, a generalized likelihood ratio test is used to identify intensity changepoints. The probability that the observed data contain an intensity changepoint is calculated and compared to the probability that there was no changepoint. From this, the locations of where the changepoints occur throughout a PL trajectory can be found. Along with the position, a confidence region for the position of the changepoint (the possible range of the position)

and confidence level (how certain the location is) are obtained.[48] Lastly, using the Bayesian information criterion, various detected changepoints are clustered into a finite number of discrete intensity levels. As a result, both the number and location of intensity changes are found, and a PL trajectory that is free of binning can be reconstructed. Alternative bin-free analyses do exist that are either based on power spectral densities[26,53,54] or autocorrelation functions.[49,55] These methods can be very fast, enabling large sample sizes to be investigated, but typically they cannot be used to independently extract on and off state kinetics. A recent autocorrelation analysis was able to determine both on and off power-law exponents by making use of a few assumptions including that all NCs in a batch of data have identical exponents.[49] Since it is beneficial to investigate the bias associated with binning and thresholding without restricting the kinetics of each NC (power-law exponents, number of intensity levels), CPA is the most suitable bin-free analysis method to employ in the current study.

In this chapter, the kinetics of PL blinking in single CdSe/CdS core/shell NCs consisting of two different shell thicknesses were analyzed. Blinking in this material has largely been found to deviate from the characteristic binary behavior often reported for CdSe NCs capped with ZnS shells.[26,56–59] The blinking kinetics were first examined using the bin and threshold method to identify any bias such a method introduces. Subsequently, CPA was carried out and the number of intensity levels determined. The τ_c values of individual levels are compared to the truncation times calculated by assuming the presence of only two levels, and a discrepancy is found between τ_c values.

3.3 Experimental Methods

The CdSe/CdS nanocrystals used in this work were synthesized following an adaptation of a procedure previously detailed by Chen et al.[60] The core size was 3.7 (0.26) nm, and the shell thickness was either 11.9 monolayers (MLs) for the 12 (1.3) nm NCs or 4.3 MLs for the 6.8 (0.3) nm NCs, where 1 ML = 0.35 nm. TEM, optical absorption and PL spectra, and quantum yield information for the two samples are summarized in Figure 3.1. Dilute NC solutions were drop-cast onto fused silica coverslips to achieve dispersed samples with concentrations < 0.01 NC/μm^2. The samples were mounted in a modified Olympus IX71 inverted confocal microscope, equipped with piezoelectric x-y (PI 517) and z (home-built from Thorlabs AE0505D16F) stages for alignment and focus.

The second harmonic (400 nm) of the output of a Coherent RegA 9000 amplifier (800 nm, 200 fs, 300 kHz) seeded by a Coherent Mira 900 oscillator was used as the pulsed excitation source. The 400 nm light was transmitted through neutral density filters to achieve a low probability of exciton formation per pulse ($\langle N_{ex} \rangle \approx 0.005$) and focused by a $\times$100, 1.3 NA oil-immersion objective (Nikon PlanFluor) onto the sample surface. The PL from individual NCs was collected in an epifluorescence scheme, filtered by a dichroic (Semrock Di405) and short-pass and long-pass filters, and focused onto two avalanche photodiodes (MPD

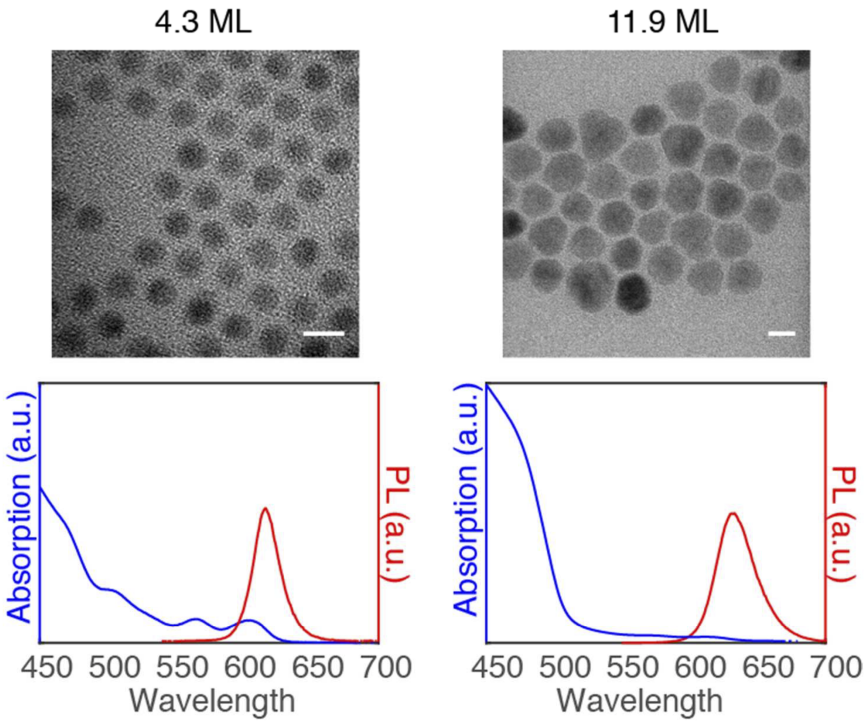

Figure 3.1: TEM, absorption and PL spectra of the two NC sizes used in the study. The 4.3 monolayer (ML) sample has a total diameter of 6.8 ± 0.3 nm, and quantum yield of 70% measured with an integrating sphere. The 11.9 ML particles have a total diameter of 12 ± 1.3 nm and quantum yield of 85%. Both TEM scale bars are 10 nm.

PDM-50 series) in a Hanbury-Brown and Twiss setup. The photodiodes were input to a time-correlated single photon counting (TCSPC) module (PicoQuant PicoHarp300/PHR 800) with an overall instrument response of ∼30 ps.

Photon arrival times were recorded for 10 min via TCSPC for all NCs. The 17 NCs analyzed in this study were selected on the basis of displaying the best photon antibunching in a second-order intensity correlation (zero time-delay peak area < 0.1 subsequent three peaks, see Figure 3.2) to ensure all NCs were isolated particles. For the bin and threshold analysis, PL trajectories were produced by choosing bin sizes of 10, 50, and 100 ms. To separate into a series of on and off durations, a threshold was set to be just above the off-state peak by analysis of the intensity histogram.

The PL trajectories were then separated into on and off durations, and weighted probability distributions, $P(\tau_i)$, were obtained by weighting the occurrence of a given on or off duration, $N_{\tau,i}$, by the average time difference from the next longer and shorter durations:

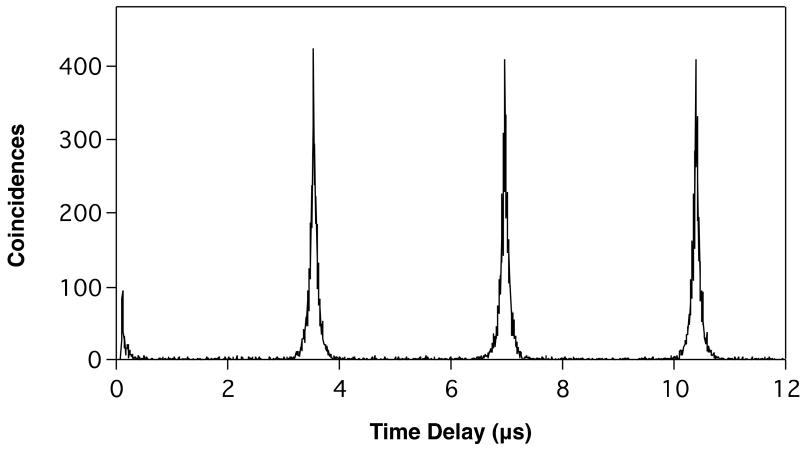

Figure 3.2: Second-order intensity correlation of a single NC displaying photon antibunching.

$$P(\tau_i) = \frac{2N_{\tau,i}}{(\tau_{i+1} - \tau_i) + (\tau_i - \tau_{i-1})} \tag{3.1}$$

For both bin and threshold and CPA methods, fitting of the probability distributions to truncated and nontruncated power laws was carried out in Igor Pro using a nonlinear least-squares fitting procedure.

3.4 Results and Discussion

The blinking kinetics of 17 CdSe/CdS core/shell NCs are studied, of which 8 (NC1-8) were 6.8 (0.3) nm in diameter and 9 (NC9-17) were 12 (1.3) nm. The probability distributions obtained from binning and thresholding the 17 PL trajectories are first examined to understand the inherent bias that this method introduces. It is assumed that each trajectory consists of two intensity levels: a low, background-PL level below a threshold referred to as an off state and a high PL, above-threshold on state. It was found that increasing the bin size generally led to a larger measured on-state truncation time τ_c, while increasing the threshold always decreased this truncation time. These findings are in agreement with the theoretical study of Frantsuzov et al.[34] and the experimental results of Crouch et al.[43] and Qin and Guyot-Sionnest.[56] The on-state probability distributions of NC10 obtained for various bin and threshold settings are shown in Figure 3.3 to illustrate these trends, and the τ_c and τ_d values for all 17 NCs are summarized in Table 3.1.

Next, the CPA method is used to analyze blinking in this sample of NCs, where the two-level assumption (employed in the previous method) can be relaxed and the artificial time scale introduced from binning and thresholding removed. As a result, 12 out of 17 NCs had more

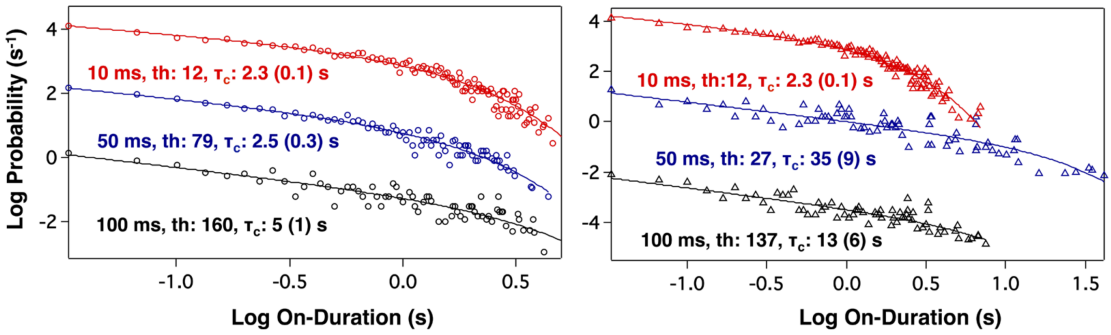

Figure 3.3: Results of changing bin size and threshold in NC10. Red, blue, and black curves represent on-state probability distributions and corresponding changes in τ_c using 10, 50, and 100 ms bin times, respectively. Circles and triangles represent different threshold locations (noted as th). The traces have been vertically offset for clarity.

Table 3.1: τ_c/τ_d Values of On/Off States Obtained Using the Bin and Threshold Method for Various Bin Sizes.

NCs	**On-State τ_c (s)**			**Off-State τ_d (s)**		
	10 ms	**50 ms**	**100 ms**	**10 ms**	**50 ms**	**100 ms**
1	1.06 (0.06)	1.8 (0.2)	1.4 (0.1)	2.7 (0.9)	0.7 (0.4)	0.4 (0.1)
2	0.83 (0.06)	3.3 (0.4)	14 (6)	-	-	-
3	1.02 (0.07)	1.5 (0.2)	2.1 (0.3)	5 (2)	-	-
4	5.6 (0.4)	6 (1)	5 (1)	8 (3)	3 (2)	-
5	4.1 (0.4)	16 (6)	11 (2)	-	10 (3)	13 (6)
6	0.65 (0.03)	6.7 (0.9)	5.1 (0.8)	3 (1)	0.9 (0.7)	0.4 (0.1)
7	2.4 (0.2)	20 (7)	12 (4)	16 (13)	-	-
8	1.0 (0.06)	1.6 (0.2)	1.6 (0.2)	8 (3)	9 (4)	-
9	26 (4)	23 (9)	-	0.5 (0.2)	-	-
10	2.3 (0.2)	2.5 (0.3)	5 (1)	-	-	-
11	4.9 (0.3)	4.6 (0.6)	4.1 (0.6)	1.7 (0.5)	-	-
12	2.8 (0.2)	2.8 (0.3)	4.2 (0.9)	-	-	-
13	1.1 (0.06)	1.8 (0.2)	3.1 (0.4)	-	-	-
14	0.97 (0.05)	1.3 (0.2)	4.2 (0.6)	0.4 (0.1)	-	-
15	4.7 (0.3)	3.6 (0.7)	3.0 (0.8)	11 (7)	-	3 (2)
16	1.09 (0.06)	3.3 (0.4)	11 (2)	-	-	-
17	2.3 (0.2)	-	-	-	-	-

than two CPA intensity levels (herein, intermediate intensity levels are referred to as gray states) as summarized in Table 3.2.

Table 3.2: Number of Intensity Levels in the Measured NCs as Found Using CPA

6.8 nm NCs	no. of levels	12 nm NCs	no. of levels
1	2	9	2
2	2	10	3
3	2	11	3
4	2	12	3
5	3	13	3
6	3	14	3
7	3	15	4
8	4	16	5
		17	5

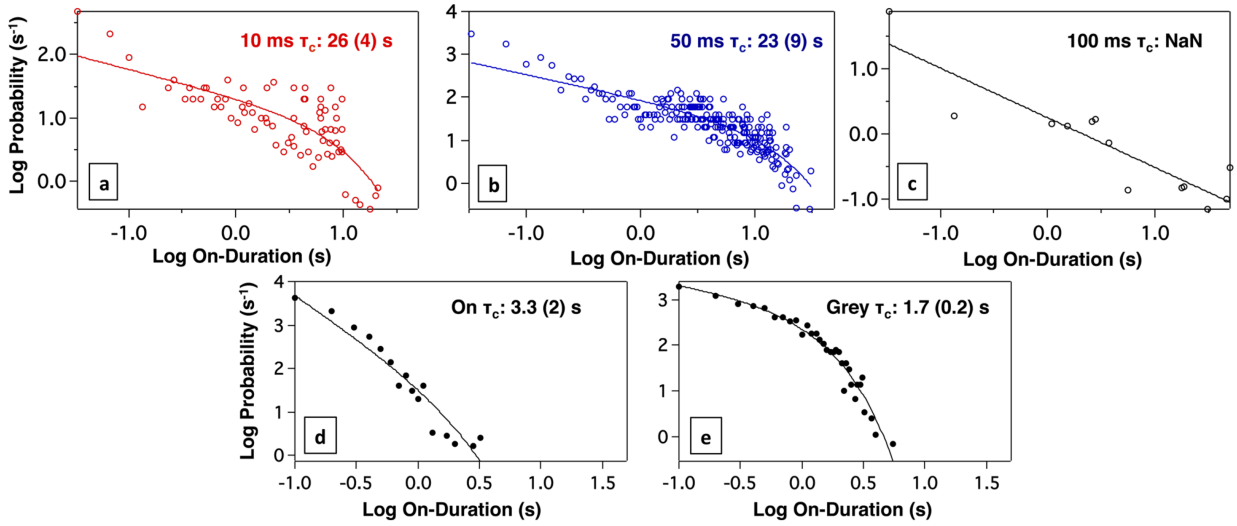

Figure 3.4: (a), (b), and (c) are the bin and threshold method on-state probability distributions of NC9 for bin sizes 10, 50, and 100 ms, respectively, and (d) and (e) are the CPA probability distributions of two different levels with intensities of 2432 and 1748 cps, respectively.

In comparing the bin and threshold results to those from CPA, a significant discrepancy in τ_c values is apparent. As an example, using the threshold method and a 100 ms bin time, the on-state probability distribution of NC9 cannot be fit to a truncated power law (Figure 3.4a), while τ_c is 23 (9) and 26 (4) s for 50 and 10 ms bin times, respectively (Figures 3.4b and 3.4c, respectively). Expectedly, τ_c is dependent on the choice of bin size. Using the CPA

method, NC9 is found to have an on state with an intensity of 2432 cps (counts per second) and a τ_c of 1.7 (0.2) s and a gray state with an intensity of 1748 cps and a τ_c of 3.3 (2) s (Figures 3.4d and 3.4e, respectively), where the lowest level is assigned as a gray state due to its high intensity counts. There are two distinct differences between the analysis methods: (a) the truncation times obtained using CPA are different from the bin and threshold values regardless of bin size, and (b) although there are two intensity levels for both methods, the ratio (1.4) between the two CPA intensity levels is too small and the lowest intensity level too high above the background PL for it to be considered an off state.[57] In fact, in 15 NCs the intensity difference between the off and on states is on average 5.0 (1.0). Since 1.4 is significantly smaller than 5.0 (1.0), the lowest intensity is assigned to be a gray state rather than an off state even though there are two CPA levels.

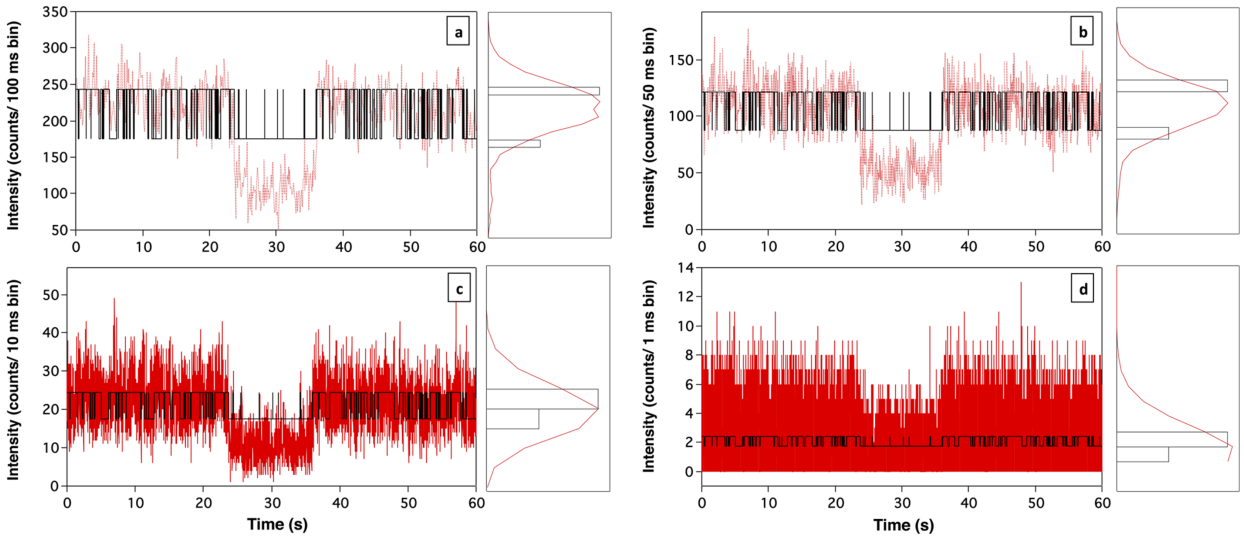

Figure 3.5: PL trajectory of NC9 with bin size (a) 100, (b) 50, (c) 10, and (d) 1 ms, where the red trace is the bin and threshold trajectory and the black is the CPA trajectory, with the corresponding normalized intensity histograms for both methods. The CPA intensities are multiplied by the bin size used in the bin and threshold method for more facile comparison.

In order to understand the origin of this discrepancy, a section of the NC9 PL trajectories analyzed by both methods is evaluated (Figure 3.5). To facilitate the comparison of the PL trajectories and histograms between the two methods, the CPA intensities (in cps) are normalized by multiplying by the bin size (in s) used for the bin and threshold method. In this sample 100 ms-binned trajectory, there is one section from 22 to 35 s where there is a distinct mismatch between CPA and binning and thresholding (Figure 3.5a). However, as the bin size decreases from 100 to 50 ms (Figure 3.5b) and then to 10 ms (Figure 3.5c) and 1 ms (Figure 3.5d), this discrepancy tends to diminish. This section is most likely a false off state, arising from averaging photons over a specific bin time and assuming that

the lowest intensity is an off state and anything above a set threshold is an on state; i.e., when a threshold is set for NC9, the 22-35 s section will be considered an off state and the rest will be considered on states. In comparison, CPA does not have such a predetermined assumption, and although NC9 has two intensities, the typical two level-assumption (on/off states only) is not invoked and NC9 is found to have one on-state level, one gray state, and no off state.

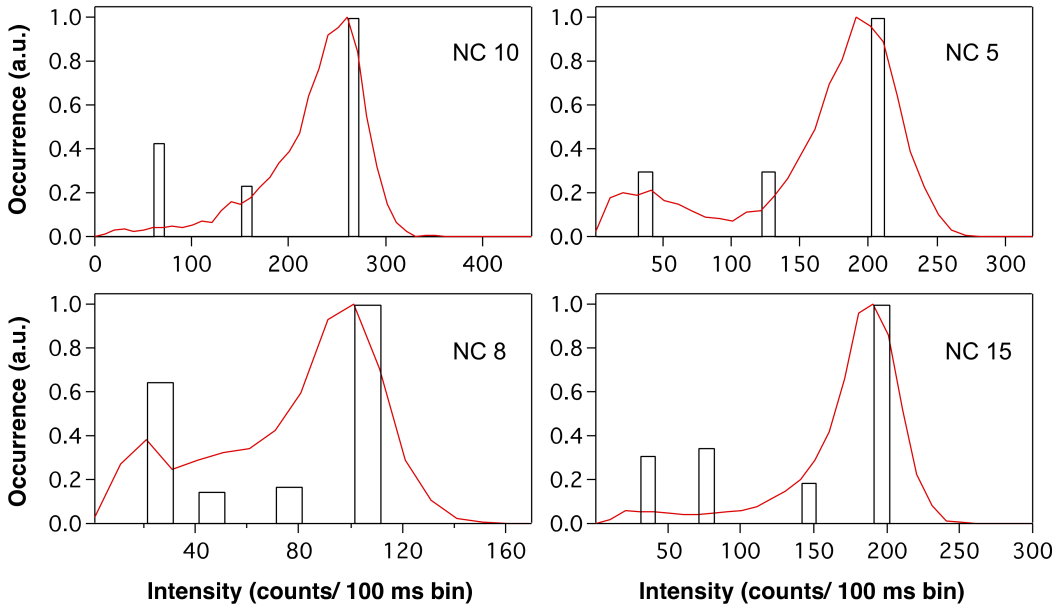

Figure 3.6: PL intensity histograms from binned PL trajectories (red), overlaid with CPA intensities derived using the CPA cluster algorithm (black).

In contrast to the CPA method, avoiding the two-level assumption when using a bin and threshold analysis proves to be difficult. Decreasing the bin size provides the highest resolution of time scales,[50] but as bin size decreases it becomes more challenging to distinguish levels in intensity histograms. For instance, though the ratio between bright and gray state intensity levels stays the same at 1.4 for the CPA method, it becomes questionable where to set the threshold for bin sizes of 10 and 1 ms (Figures 3.5c and 3.5d) in the bin and threshold trajectories. A similar issue is encountered with increased bin sizes. When the 100 ms intensity histograms of NCs 5, 8, 10, and 15 are compared to those obtained using the CPA method (Figure 3.6), the bin and threshold histograms appear to have more than two intensity levels, presumably composed of multiple Gaussian curves with maxima centered near the CPA intensity levels. However, choosing the number of Gaussian curves the histogram should be fit to is ambiguous, and thus both the number and location of intensity levels cannot be reliably obtained using this method. For these reasons, it is often assumed that there are only two intensity levels, where the lowest intensity is considered the off state

and anything above is considered an on state.

Due to the aforementioned challenges, a closer look is taken at NCs that displayed multiple intensity levels using CPA; the two-level assumption is evaluated in the absence of any pre-imposed time scale by utilizing the ability to obtain probability distributions for each CPA intensity level. For each multilevel NC, the τ_c values from the probability distributions of individual CPA levels and the τ_{c_comb} values from combining the gray and on-state probability distributions are compared. For instance, NC15 has a total of four levels: an on state, an off state, and two gray states. When the probability distributions are fit for each individual level, the highest three intensity levels of 1961, 1411, and 773 cps have corresponding τ_c values of 2.0 (0.2), 0.5 (0.1), and 1.61 (0.04) s; however, when only one on-state level is assumed and the individual probability distributions are combined, the resulting truncation time (τ_{c_comb}) increases to 7 (1) s. A general trend is apparent that when a two-level assumption is made, the truncation time tends to increase, with the actual magnitude of difference depending on the particular NC. Table 3.3 summarizes the τ_{c_comb} values from combined levels and the ratio $\Delta = (\tau_{c\_comb}/\tau_c)$, which is always ≥ 1. Figure 3.7 illustrates this trend, where the black circles representing the τ_{c_comb} are consistently larger than the red circles representing the τ_c values of the individual levels. It should be noted that it is reasonable to observe a longer τ_c when intensity levels are combined. As an example, within a 5 s window containing two levels, one level may be 3 s in duration and the other level 2 s; when these are combined into one level with a 5 s duration, the probability distribution will contain longer on-state durations and therefore a longer truncation time.

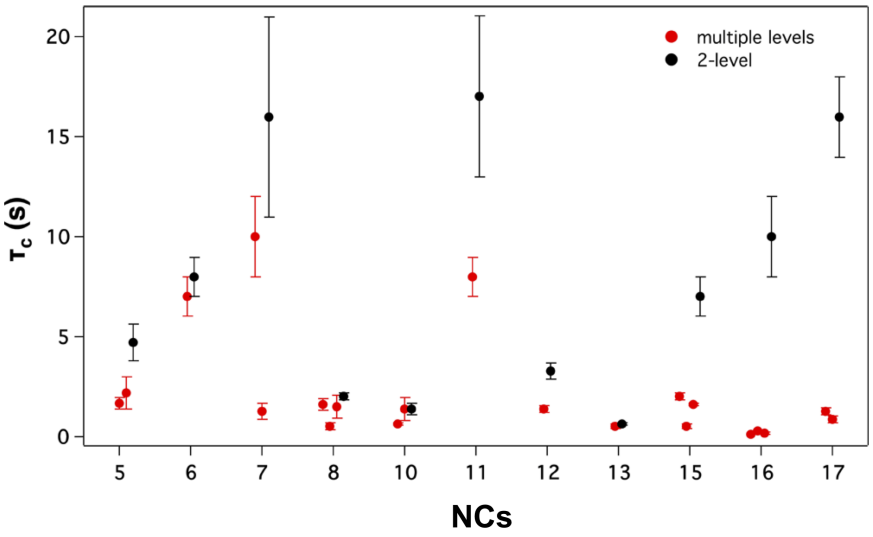

Figure 3.7: Truncation times, τ_c, of individual emission levels (red circles) and combined levels, τ_{c_comb} (black circles). The error bars represent the standard deviation.

Table 3.3: τ_c Values of Individual CPA Levels with Corresponding Intensity Counts Compared to the τ_{c_comb} Values from Combined Levels and the Ratio, Δ, Equal to τ_{c_comb}/τ_c^a

6.8 nm NCs	**intensity (cps)**	τ_c **(s)**	τ_{c_comb} **(s)**	Δ
1 on	997	1.1 (0.1)	-	-
2 on	836	3.0 (0.2)	-	-
3 on	1234	0.8 (0.1)	-	-
4 on	1096	2.0 (0.2)	-	-
5 on	2086	1.7 (0.3)	4.7 (0.9)	2.8 (0.3)
5 gray	1259	2.2 (0.8)	-	2.1 (0.4)
6 on	664	7 (1)	8 (1)	1.1 (0.2)
7 on	791	10 (2)	16 (5)	1.6 (0.4)
7 gray	414	1.3 (0.4)	-	12.3 (0.4)
8 on	1082	1.6 (0.3)	2.0 (0.2)	1.2 (0.2)
8 gray	797	0.5 (0.2)	-	4.0 (0.4)
8 gray	450	1.5 (0.6)	-	1.3 (0.4)
12 nm NCs	**intensity (cps)**	τ_c **(s)**	τ_{c_comb} **(s)**	Δ
9 on	1748	3.3 (2)	-	-
9 gray	2432	1.7 (0.2)	-	-
10 on	2684	0.65 (0.06)	1.4 (0.3)	2.2 (0.2)
10 gray	1571	1.4 (0.6)	-	1.0 (0.5)
11 on	1153	8 (1)	17(4)	2.1 (0.3)
12 on	2220	1.4 (0.2)	3.3 (0.4)	2.4 (0.2)
13 on	3452	0.5 (0.1)	0.62 (0.07)	1.2 (0.2)
14 on	4330	0.46 (0.08)	-	-
14 gray	3420	0.27 (0.06)	-	-
14 gray	2169	0.11 (0.02)	-	-
15 on	1961	2.0 (0.2)	7 (1)	3.5 (0.2)
15 gray	1411	0.5 (0.1)	-	14.0 (0.2)
15 gray	773	1.61 (0.04)	-	4.3 (0.1)
16 on	3525	0.13 (0.02)	10 (2)	76.9 (0.2)
16 gray	2858	0.30 (0.07)	-	33.3 (0.3)
16 gray	1917	0.21 (0.07)	-	47.6 (0.4)
17 on	2218	1.3 (0.2)	16 (2)	12.3 (0.2)
17 gray	1895	0.9 (0.2)	-	17.8 (0.2)

[a]The CPA intensities are derived using the CPA cluster algorithm.[48]

Assuming that the bias arising from binning and thresholding blink traces is largely eliminated with CPA, there still exists uncertainty as to whether these multiple levels have real physical origins, meaning they arise from different emissive states. In order to evaluate such an issue, both the validity of the CPA method with respect to detecting multiple levels and the physical origin of these levels must be understood.

CPA uses an algorithm called Bayesian information criteria (BIC) (also known as xs criterion):[48]

$$\mathrm{BIC} = 2\mathcal{L}_G - (2n_G - 1)\ln N_{cp} - N_{cp}\ln N \tag{3.2}$$

to determine the number of levels, where N_{cp} is the number of changepoints, N is the total number of photons, and $\mathcal{L}_G$ is the log-likelihood, evaluating how accurately the n_G or the number of states represents the original data. The n_G that gives the maximum BIC value represents the most likely number of levels that are contained in the trajectory. The performance of BIC increases with the number of changepoints detected; for instance, with 500 changepoints detected, the accuracy of CPA exceeds 90%. However, the absolute value of the uncertainty increases as the number of levels increases. As an illustration of the effect of N_{cp} and number of levels on the accuracy (or uncertainty), for trajectories with two levels, the absolute uncertainty is less than 3% when the N_{cp} is 50, and for those with six levels the uncertainty is less than 5% when N_{cp} is 500. The uncertainty is always less than 5% for the data reported considering the N_{cp} detected in the 17 NCs is ≥ 695.

Despite this ability to quantify the absolute uncertainty, there exists ambiguity in detecting all the changepoints due to the choice of the correct parameters for the acceptable level of false positives in hypothesis tests, as stated in the work of Houel et al.[49] and Watkins and Yang.[48] False positives refer to the detection of changepoints that do not correspond to real states. An allowed value of false positives must be selected to maximize the efficiency of detecting all changepoints while minimizing the detection of false changepoints.[49] In order to address this issue, different values of allowed false positives are input into the CPA analysis, and the reconstructed CPA trajectories are cross-correlated to those obtained from a minimum binning approach. Briefly, the minimum bin approach, where there is at least one photon in each bin, is selected as it gives the highest time resolution and widest range of time scales, comparable to CPA.[50] The two PL trajectories are cross-correlated with a zero time delay, and a cross-correlation coefficient is calculated. The highest cross-correlation coefficient represents the closest match between the CPA trajectory and minimal binning approach. In this study, the values 0.01 and 0.95 for detecting false changepoints and the confidence interval, respectively, gave the largest cross-correlation coefficient. These values can be interpreted as a 1% probability of detecting false changepoints among a number of N detected changepoints and a 95% confidence that the true changepoint lies in the calculated confidence region. Different scenarios of these values for various systems of number

of photons detected and intensity ratios between levels have been previously demonstrated.[48]

Having addressed the accuracy of the CPA method in detecting multiple levels, possible explanations for the physical origins of multiple intensity levels can be reviewed. Gray state emission has been observed in several studies, although the conclusions on what gives rise to an intermediate emissive level have varied.[26,41,56–59,61–63] Two early studies attributed the appearance of a gray state in CdSe/CdS NCs to positive trions created via electron ionization[57] or electron surface trapping,[59] on the basis of the electron being delocalized across the NC core and shell while the hole remains localized in the core. Conversely in the same material, Qin and Guyot-Sionnest assigned the gray state to negative trions formed from hole trapping to shallow surface states, based on the similarity between the negative trion lifetime and the gray state lifetime.[56] A subsequent experiment engineered deep hole traps using CdSe/CdS seeded rods with PbS tips; upon introduction of the deep hole trap, the appearance of gray state emission at the expense of the on state was attributed to negative trions.[58]

There are additional models that propose origins for gray states that are not due to trions. For example, a charge-tunneling and self-trapping (CTST) model recently proposed by Osborne and Fisher provides an origin for the gray state that is shell thickness dependent.[63] In the CTST model framework, the bright and gray states in thin-shelled NCs arise from surface-charged ionized exciton states and mixed contributions including the neutral, emissive core-exciton state, respectively. With increasing shell thickness, the modulation depth between the surface-charged states and the neutral emissive state increases as the surface-charged exciton states become quenched relative to the latter. As a result, the gray and bright intensity levels become further separated and are more easily resolved with increasing shell thickness. This finding is consistent with the results presented here: all of the nine 12 nm NCs exhibited resolvable gray state emission while only four out of eight of the 6.8 nm NCs did the same.

The multiple recombination center (MRC) model attributes blinking to a fluctuating nonradiative rate. Specifically, fluctuations are proposed to occur in the hole trapping rate via surface quenching centers that can switch between active (high hole trapping rate) and inactive (low hole trapping rate) conformations; hole trapping to the recombination centers (RC) is then followed by nonradiative recombination.[34] The MRC model can naturally predict a continuous distribution of intensities, and an observation of increased gray states in thicker shelled NCs could be expected. As the shell thickness is increased, surface RCs are placed further away from the localized hole in the NC core, which leads to a decrease in the trapping strength of RCs in the active conformation. The MRC model has been able to account for high, medium, and low intensity levels in CdSe/CdS NCs through the combination of one weak RC and a few strong RCs.[26] It is reasonable to expect a higher number of these weak RCs relative to strong ones as shell thickness is increased, and thus one would expect, within the MRC model framework, to observe more gray states in thicker shelled NCs. The average number of emission states for the 12 (1.3) nm NCs, 3.4, is indeed larger than that of the 6.8

(0.3) nm NCs, 2.6.

While the MRC result was obtained using a power spectral density analysis, the previous referenced works relied on the bin and threshold method. Gray state emission was observed in binned intensity histograms with small bin sizes (<10 ms), with the gray state peak vanishing when the binning time is increased. However, even if gray states can be detected in intensity histograms using small bin sizes, investigating their kinetics remains very challenging since the gray state kinetics may be unresolved from the on-or off-state kinetics depending on the choice of bin and threshold. In addition, as was pointed out previously, a statistically rigorous assignment of the number and location of emissive states using the bin and threshold method is ambiguous. While in previous experiments that analyze gray states via the bin and threshold method, the gray state probability distribution was found to follow exponential or stretched exponential kinetics,[56,58,59] in this CPA study, gray states were observed to exhibit power-law kinetics similar to the on and off states. As an accurate description on the origins of gray states relies largely on the ability to fit probability distributions while avoiding biases associated with binning and thresholding, the CPA method offers a reliable and robust means to detecting and elucidating the kinetics of gray state emission in single NCs.

3.5 Conclusions

In this study, changepoint analysis was used to study the biases associated with analyzing the kinetics of PL blinking in semiconductor NCs. It is a commonly used assumption that there is one on and one off state when using the bin and threshold method. Using CPA, most NCs studied here contain more than one on and one off state, prompting a re-evaluation of the two-level assumption. The truncation time (τ_c) from the probability distributions of individual levels is observed to be significantly different than the τ_c obtained using the two-level assumption. The performance and validity of the CPA method are evaluated, and the physical origins of gray state emission are discussed. In the NCs investigated in this work, the two-level assumption is found to be invalid, and multilevel emission could be more accurately studied using the CPA method in place of the more traditional bin and threshold method.

Chapter 4

Excitation Intensity Dependence of Photoluminescence Blinking in $CsPbBr_3$ Perovskite Nanocrystals

The content and figures in this chapter are reprinted or adapted with permission from N.A. Gibson, B.A. Koscher, A.P. Alivisatos, and S.R. Leone, "Excitation Intensity Dependence of Photoluminescence Blinking in $CsPbBr_3$ Perovskite Nanocrystals," J. Phys. Chem. C., **2018**, 122, 12106-12113.

4.1 Summary

Perovskite semiconductors have emerged as a promising class of materials for optoelectronic applications. Their favorable device performances can be partly justified by the defect tolerance that originates from their electronic structure. The effect of this inherent defect tolerance, namely the absence of deep trap states, on the photoluminescence (PL) of perovskite nanocrystals (NCs) is currently not well understood. The PL emission of NCs fluctuates in time according to power law kinetics (PL intermittency, or blinking), a phenomenon that has been explored over the past two decades in a vast array of nanocrystal (NC) materials. The kinetics of the blinking process in perovskite NCs have not been widely explored. Here, PL trajectories of individual orthorhombic cesium lead bromide ($CsPbBr_3$) perovskite NCs are measured using a range of excitation intensities. The power law kinetics of the bright NC state are observed to truncate exponentially at long durations, with a truncation time that decreases with increasing intensity before saturating at an intensity corresponding to an average formation of a single exciton. The results indicate that a diffusion-controlled electron transfer (DCET) mechanism is the most likely charge trapping process, while Auger autoionization plays a lesser role. The relevance of the multiple recombination centers (MRC) model to the results presented here cannot be ascertained, since the underlying switching mecha-

nism is not currently available. Further experimentation and theoretical work are needed to gain a comprehensive understanding of the photophysics in these emerging materials.

4.2 Introduction

Semiconductor nanocrystals (NCs) have many optical and electronic properties that are unique from, and often superior to, their bulk counterparts. These include discrete, size-tunable optical transitions, narrow photoluminescence (PL) line widths, high photoluminescence quantum yields (PLQYs), and facile solution-based syntheses. This has motivated both fundamental research into these materials as well as the development of NC-based devices and applications. Numerous compositions can be routinely synthesized and have been extensively researched, typically for the II-VI, III-V, and IV-VI families of semiconductors. Recently, ionic perovskite semiconductors have emerged as promising materials for incorporation into optoelectronic devices such as solar cells,[64–66] light-emitting diodes (LEDs),[67,68] and lasers,[69–71] and several inorganic and hybrid organic-inorganic perovskite nanostructures have been successfully synthesized.[72,73] Inorganic cesium lead halide, $CsPbX_3$ (X = Cl, Br, I), perovskite NCs exhibit composition-tunable narrow emission lines and high PLQYs even in the weak electronic confinement regime and without a passivating shell.[73] Metal chalcogenide NCs such as CdSe, in comparison, must be engineered with a passivating semiconductor shell, good ligand coverage, and at sizes comparable to or smaller than the Bohr exciton radius to achieve high PLQYs.

In most covalently bound semiconductors like silicon, the valence and conduction bands originate from bonding-antibonding orbital pairs. The presence of defects, for example, vacancies, interstitials, and substitutions result in defect energy levels that can be located deep within the bandgap. These trap states open up nonradiative channels, by which the semiconductor can decay, decreasing the PLQY, among other effects. Lead halide perovskites, however, have an electronic structure that is inherently defect tolerant due to a lack of bonding-antibonding interaction between the valence and conduction bands.[74–76] While the valence band maximum originates from the strong antibonding interaction between the Pb 6s and X np atomic orbitals, the empty Pb 6p orbitals couple to form the conduction band minimum.[76] A defect tolerance emerges from this orbital interaction, in which most intrinsic defects result in shallow trap states and resonances within the bands. In $CsPbX_3$, intrinsic defects that do induce deep trap levels have high formation energies (>1.4 eV) and thus defect concentrations below 10^{-24}.[76] While these electronic structure explanations help to justify why lead halide perovskites exhibit a pronounced tolerance to defects, many questions still remain regarding how the absence of deep trap states affects carrier dynamics in perovskite NCs.

An important way to probe the effects of trap states on carrier dynamics is through PL measurements of single NCs. This is because the PL of a single NC fluctuates in time, directly

as a result of the interactions between charge carriers and trap states. This PL blinking in single NCs has been studied for two decades in many traditional NC materials and most extensively in CdSe. There is no single mechanism that can fully account for all the observations of PL blinking behavior, but blinking is consistently attributed to the interaction of charge carriers localizing at defect sites in the NC, at the surface, or external to the NC.[10,30] This charge carrier trapping can be beneficial in certain architectures of photodetectors such as photoconductors if only one type of carrier is localized, but it is undesirable for most optoelectronic devices. Charge trapping introduces nonradiative recombination pathways that are detrimental in LEDs, lasers, and imaging and tracking applications, and it decreases charge mobility and transport, which are crucial parameters in solar cells.

To understand how charge carrier trapping leads to PL blinking, photon counts are typically binned to create a time trajectory of PL intensity, which is then separated into bright,"on" periods and dark, "off" periods by applying a threshold level to the trajectory. The series of on and off durations are then used to calculate the corresponding probability distributions of the PL trajectory. In semiconductor NCs, the probability $P(\tau_i)$ of an on or off duration occurring follows a power law, $P(\tau_i) \propto \tau_i^{-\alpha}$, where α is the power law slope and scaling exponent. The off periods typically obey this simple power law on the time scale of most experiments, while the on periods can be fit to an exponentially truncated power law, $P(\tau_i) \propto \tau_i^{-\alpha} e^{\tau_i/\tau_c}$, where the truncation time, τ_c, is the time at which the power law kinetics cross over to exponential kinetics. The power law behavior of the on $\leftrightarrow$ off processes reveals distributed kinetics that have no characteristic time scale. The exponential truncation indicates that either the on $\rightarrow$ off process at long on durations occurs at a single rate or the distributed rate process saturates at long on durations.

One class of proposed explanations to account for PL blinking kinetics is based on photoinduced charging. Upon charging of the NC, subsequent excitation leads to nonradiative Auger recombination of a trion that proceeds orders of magnitude faster than radiative recombination, until the NC is reneutralized. Many models of this type have been developed, and typically, their main differences lie in the charging pathway that initiates the on $\rightarrow$ off process.[23,27,28,44,61,63,77] The most widely accepted pathway for photoinduced charging is Auger autoionization, in which one exciton in a biexciton or multiexciton state decays nonradiatively via an energy transfer to ionize one of the charge carriers of the second exciton.[23] Another mechanism that has been very successful in predicting observed PL blinking behavior is the diffusion-controlled electron transfer (DCET) model.[78] Here, the PL suppression (off state) is again attributed to Auger recombination of a trion; the on $\rightarrow$ off transitions are not due to Auger autoionization but are instead facilitated by electron transfer between two displaced Marcus parabolas, corresponding to the neutral and charged NC states. Finally, since several experiments have revealed that Auger trion recombination cannot explain all PL blinking phenomena, such as a lack of correlation between PL intensity and lifetime[45] and the low PLQY of the off state,[79–81] another set of mechanisms have been proposed that do not involve Auger recombination of charged NCs. These rely on trapping rates that fluc-

tuate with time and can involve a fast removal of a hole to a surface trap state[34,82] or direct trapping of hot electrons to a surface state,[45] followed by rapid nonradiative recombination.

The experimental PL blinking observations that contributed to the development of these theoretical frameworks have been based on semiconductor compositions of type III-V, IV-VI, and II-VI, with the majority being II-VI materials. How charge carrier trapping occurs in perovskite NCs and how it manifests itself in the PL of a single perovskite NC have not been well established. While several experiments have been carried out, the results have varied widely, and a clear picture has not emerged regarding how NCs without deep intrinsic trap states compare with more traditional semiconductor NC compositions.[83–89] In this work, PL trajectories of over 130 single In $CsPbX_3$ NCs are recorded over four excitation intensities (I_{ex}), without significant photobleaching throughout the total acquisition time for each. The probability distributions of the on and off durations are obtained, and the intensity dependence of the power law truncation times are considered in the context of PL blinking models. The on-state truncation time is found to initially decrease with excitation intensity, nonquadratically, until a saturation is reached when an average of a single exciton is formed per pulse. These observations indicate that an Auger autoionization mechanism cannot account for the power law truncation on its own, and the results point toward a DCET mechanism for the on $\rightarrow$ off trapping process.

4.3 Experimental Methods

Weakly confined $CsPbX_3$ NCs with an edge length of 10 $\pm$ 1.5 nm (Bohr exciton diameter of 7 nm[73]) were synthesized following a known procedure.[73] Recent Rietveld refinement and pair distribution function analyses of X-ray total scattering data confirm that the room temperature crystal structure of $CsPbX_3$ NCs is orthorhombic with the space group Pnma.[90] A dilute solution of the NCs in toluene was mixed with a 3% poly(methyl methacrylate)(PMMA)/toluene solution in a 1:1 ratio to help with dispersion and then drop-cast onto a UV-grade fused-silica coverslip. The coverslip was mounted in a modified Olympus IX71 inverted confocal microscope, equipped with a 2D piezoelectric scanning stage (PI 517) and z stage (home-built). Pulsed excitation at 400 nm was achieved by the second harmonic of the output of a Coherent RegA9000 amplifier (200 fs, 300 kHz) seeded by a Coherent Mira900 oscillator. The excitation light was focused through a 100×, 1.3 NA oil immersion objective (Nikon PlanFluor) onto the coverslip surface. Fluorescence was collected in an epifluorescence scheme using a dichroic mirror (Semrock, Di405) and several long-pass and band-pass filters and focused to two avalanche photodiodes (MPD, PDM-50 series) that were input to a time-correlated single photon counting (TCSPC) module (PicoQuant, PicoHarp 300).

All measurements were conducted at room temperature, in an ambient atmosphere, and within an average excitation intensity (I_{ex}) range of 2.5-17.7 W/cm^2. To determine I_{ex}, the

average excitation power was measured directly, and the focal spot size area (Area = $\pi D^2/4$, where D = diameter) was calculated from the Gaussian full width at half-maximum (fwhm) of representative emission spot size scans. The average number of excitons formed per pulse was calculated according to:

$$\langle N_{ex} \rangle = \ln(2) \times \frac{I_{ex}\, \alpha_{abs(\lambda=400\text{ nm})}}{E_{(\lambda=400\text{ nm})} \Gamma_{rep}} \tag{4.1}$$

where $E_{(\lambda=400\text{ nm})}$ is the energy of 400 nm excitation, and Γ_{rep} is the laser repetition rate. The absorption cross section, $\alpha_{abs(\lambda=400\text{ nm})}$, is the cross section for single photon absorption (1PA) at 400 nm.[47] Only 1PA events are assumed to occur under the excitation conditions used here. Two-photon absorption (2PA) has been studied at photon energies below the bandgap but not at photon energies that compete with ground-state 1PA.[91] The cross section for 2PA at 400 nm is likewise assumed to be many orders of magnitude smaller than the one-photon cross section, requiring very large peak intensities to compete with 1PA. A sequential two-photon process such as excited-state absorption (ESA) is another possibility, but the ESA cross section would need to be larger than the ground-state absorption cross section for this to occur. A pump-fluence dependence of the early-time (A) and late-time (B) time-resolved photoluminescence (TRPL) amplitudes confirms that one exciton is produced from one absorbed photon, which justifies the assumption that multiphoton absorption processes are negligible in these experiments.[42]

10 min TCSPC measurements were collected for over 130 NCs with ∼30 ps resolution, providing a PL trajectory, TRPL decay, and photon antibunching trace, simultaneously. The latter is obtained through the use of a Hanbury Brown and Twiss setup consisting of a 50/50 beamsplitter that separates the emission output onto two separate avalanche photodiodes.

4.4 Results and Discussion

The basic optical properties of the $CsPbX_3$ NCs investigated here are summarized in Figure 4.1. Ensemble absorption and PL spectra of the NCs dispersed in hexanes, normalized to the band-edge absorption and emission peaks, respectively, are shown in Figure 4.1a. The band-edge absorption peak is at 506 nm, and the PL peak is at 512 nm, with a narrow fwhm of ∼100 meV. The ensemble PLQY was ∼50%. A TRPL measurement for a single NC that is representative of the average is shown in Figure 4.1b. At the lowest I_{ex} used, all NCs decayed biexponentially with an average $\tau_1 = 1.8 \pm 0.6$ ns (A1 = 68%) and $\tau_2 = 6 \pm 1$ ns (A2 = 32%), within the range of previous reports at room temperature.[42] A lack of change in the decay times or amplitudes with increasing intensity is observed, which suggests that the faster component may be due to a trap-assisted recombination, while the slower component is likely band-edge recombination.

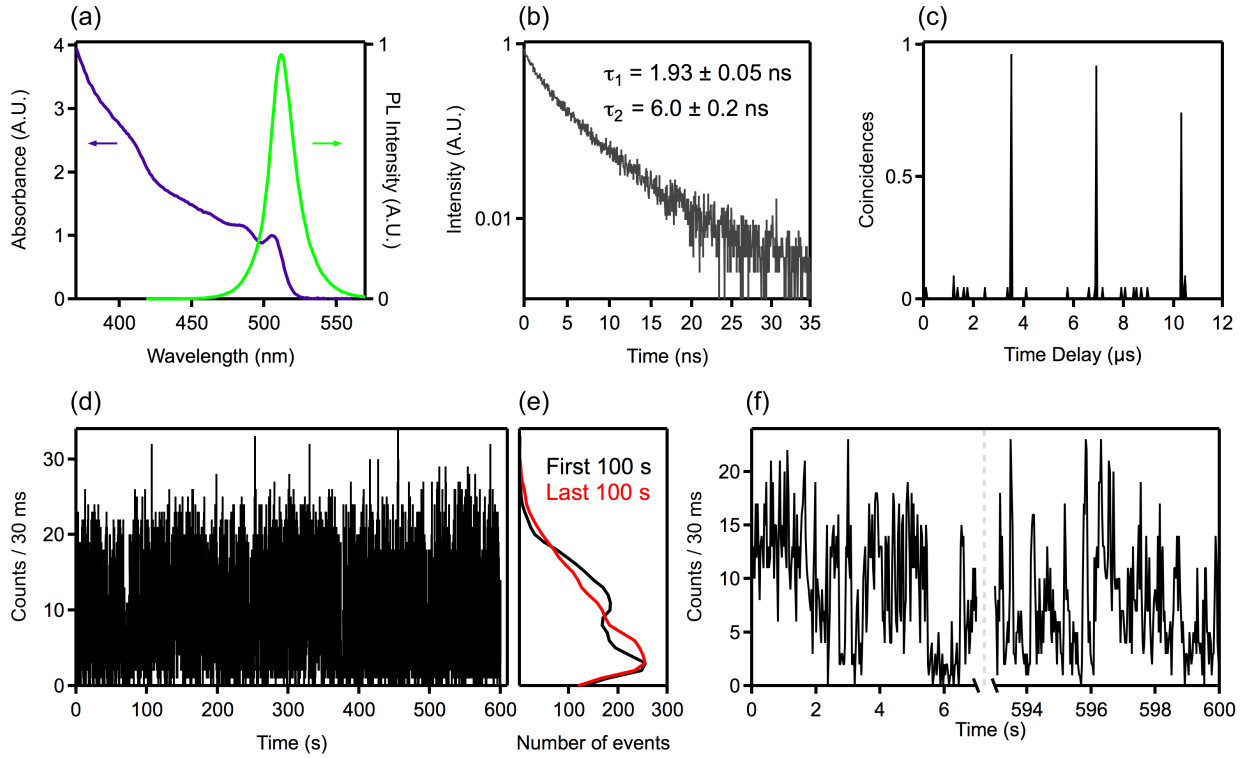

Figure 4.1: Optical properties of 10 nm $CsPbBr_3$ NCs. All single NC measurements were recorded using an intensity of 2.5 W/cm^2. (a) Absorption (purple) and PL (green) spectra of $CsPbBr_3$ NCs in hexanes. (b) Representative TRPL and (c) second-order intensity correlation for a single NC. (d) Full 10 min PL trajectory of a single NC binned at 30 ms with (e) the corresponding PL intensity histogram of the first 100 s (black) and last 100 s (red). (f) Same PL trajectory as in (d) showing only the first and last 7 s time intervals.

Single photon emission at room temperature was observed in single NCs, as evidenced by the lack of a coincidence peak at zero time delay (photon antibunching) in an example second-order intensity correlation function, $g_2(t)$ (Figure 4.1c). The zero time-delay peak, $g_2(0)$, is consistent with background noise at random delays, while delay times at intervals equal to the inverse laser repetition rate are due to photons detected from subsequent excitation cycles. To ensure all NCs investigated were individual particles, NCs with $g_2(0)$ 0.5 were discarded from further analysis.

The repetition rate of the laser used in these experiments, 300 kHz, is an order of magnitude lower than the 1-10 MHz rates often used in pulsed, single NC experiments. Combined with the femtosecond pulse durations used here in place of typical picosecond pulses, the resulting duty cycle, or active fraction of one laser period, is many orders of magnitude lower. This appears to be essential for acquiring PL trajectories of single NCs for long durations without

substantial photo-bleaching, presumably due to a sufficient time interval provided for the excited NC to fully relax between pulses.[92] A representative 10 min trajectory of a single NC binned at 30 ms, shown in Figure 4.1d, demonstrates the lack of PL bleaching over this time scale. Corresponding histograms of the PL intensity during the first and last 100 s are displayed in Figure 4.1e; notably, in about half of the NCs, the overall PL intensity counts do not significantly change, but lower emission intensities are observed to slightly increase in frequency, while the higher emission intensities slightly decrease in frequency between the first and last 100 s of the PL trajectory. The remaining NCs either demonstrate no distinguishable histogram change over time or a more substantial frequency shift. Any changes in the PL intensity histogram did appear to be permanent. A subset of the trajectory is shown in Figure 4.1f, which further illustrates the consistency in PL behavior throughout the acquisition time. In comparison, previous work using a 2 MHz excitation source reported significant bleaching in $CsPbBr_3$ NCs after less than 1 min of excitation.[86]

The results in Figure 4.1 are characteristic for NCs measured at the lowest I_{ex}. At higher I_{ex}, a small decrease in PL counts does accompany the frequency change between the first and last 100 s, and a larger portion of the NCs are completely photobleached in less than 10 min. The I_{ex} values used and the number of NCs analyzed at each intensity are summarized in Table 4.1 as well as the percentage of NCs that completely photobleached within the acquisition time. This includes a fairly small percentage of NCs at the lowest three intensities, but 17 of the 24 NCs excited at the highest intensity of 17.7 W/cm^2 experienced photobleaching within 10 min. Previous studies of lead halide perovskite NCs have observed photodegradation with an accompanying dynamical blueshift, attributed to a core-size reduction from surface destruction.[86,93] The measurements in this experiment were performed with a PMMA polymer encapsulation layer coated over the isolated $CsPbBr_3$ NCs, which is expected to act as a hydrophobic barrier and provide protection from water.[94] Thus, photodegradation at the highest intensities is expected to be caused by the opening of new, nonradiative sites as opposed to a water-assisted surface destruction.

Table 4.1: Excitation Intensities and Photobleaching Statistics of NCs Measured

I_{ex} **(W/cm^2)**	**Number of NCs**	**Photobleached <10 min (%)**
2.5	39	0
4.4	35	17
8.8	36	17
17.7	24	71

While the low repetition rate largely enables long acquisition times with minimal photobleaching, a drawback is a reduction in the overall PL counts per second. When the photon counts from the PL trajectories are binned at 30 ms, the peaks in the PL intensity histograms overlap significantly (see Figure 4.1e). This prevents the histograms from being reliably re-

solved into a distinguishable number of Gaussian peaks. As a result, the choice of a threshold value to separate the PL trajectories into on and off states becomes somewhat arbitrary and can greatly affect the resulting probability distributions.[43,95] The choice of bin time has also been found to affect the power law parameters, particularly the on-state truncation time.[43,95] To avoid binning and thresholding biases, changepoint analysis (CPA) was used instead to determine the number of intensity levels in each PL trajectory. The CPA algorithm uses a generalized likelihood ratio test to identify locations in the raw photon arrival times where intensity change points occur.[48] The Bayesian information criterion is used to cluster change points into a discrete number of intensity levels. With the number and location of intensity changes determined, a bin-free PL trajectory can be reconstructed. An example comparing the two analysis methods is shown in Figure 4.2 for a NC excited at 2.5 W/cm^2. Figure 4.3 provides additional examples of representative PL intensity histograms at each I_{ex}.

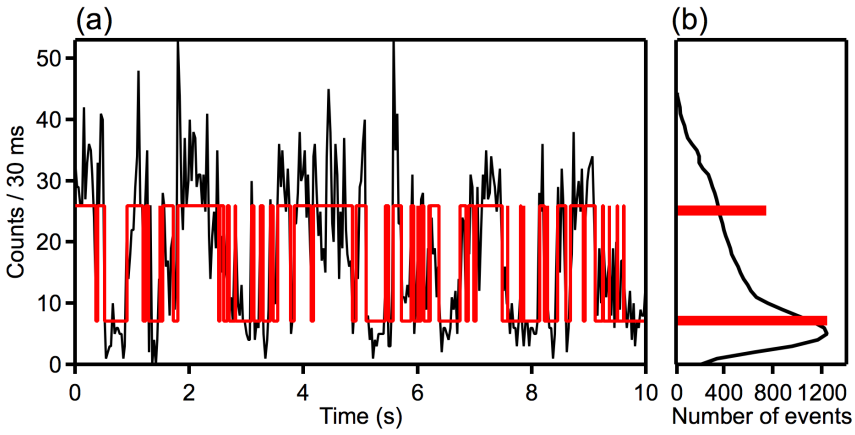

Figure 4.2: PL trajectories and histograms obtained using two different analysis methods for an NC excited at 2.5 W/cm^2. (a) 10 s of a PL trajectory binned at 30 ms in black, overlaid with corresponding CPA trajectory in red. (b) Intensity histograms for both methods.

Probability distributions were obtained using the CPA trajectories. The lowest intensity level is considered the off state, while the higher levels are considered on states. At the four I_{ex} used here, the average number of intensity levels detected using the CPA algorithm did not change ($\langle N_{levels} \rangle$ = 2.7 levels for 2.5, 8.8, and 17.7 W/cm^2; $\langle N_{levels} \rangle$ = 2.6 levels for 4.4 W/cm^2). As such, the probability distributions for all on-state levels were grouped together for improved statistics. On-state probability distributions from individual NCs that are representative across the range of excitation intensities are shown in Figure 4.4a. The probability distributions follow exponentially truncated power laws that truncate at earlier times with increasing excitation intensity. The truncation times, τ_c, for all NC probability distributions that could be reliably fit to a truncated power law are summarized in Figure 4.4b. The distribution of τ_c shifts toward smaller values with increasing I_{ex}.

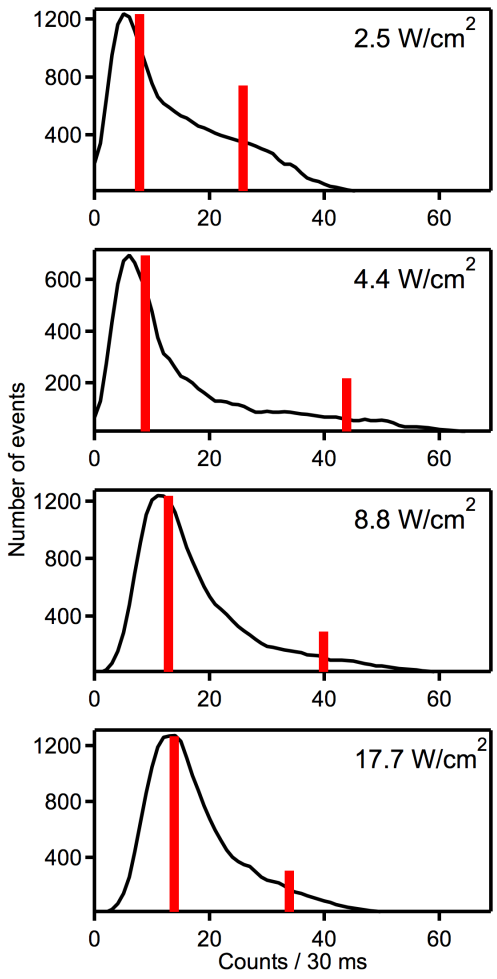

Figure 4.3: Representative PL intensity histograms at all four I_{ex} values used. The black curves correspond to PL intensity counts from trajectories binned at 30 ms. The red bars correspond to the clustered intensity levels obtained using the CPA method.

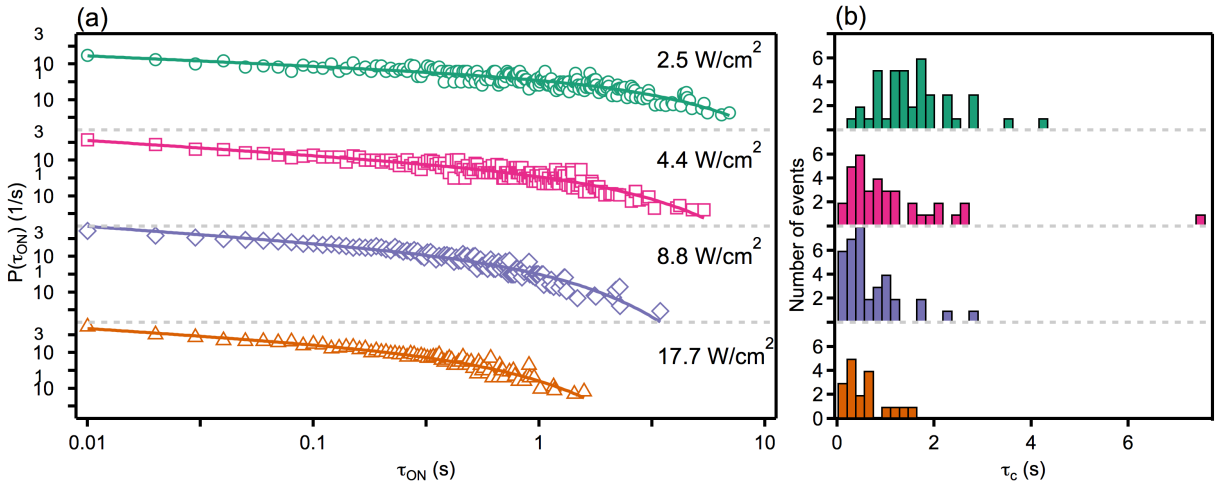

Figure 4.4: (a) Sample on-state probability distributions at each I_{ex} that follow truncated power laws. (b) Corresponding distribution of on-state truncation times for all NCs that could be fit to a truncated power law.

At all intensities used, the average power law slope (α_{on}) is < 1.2, indicating that on-state probability distributions of $CsPbBr_3$ NCs are observed to decay more slowly compared to chalcogenide NCs such as CdSe, where α_{on} is consistently between 1.2 and 1.8.[27,44,47,49] On-state truncation times vary more considerably in the literature due to their demonstrated sensitivity to various experimental conditions such as photon excitation energy, excitation intensity, dielectric constant of the surrounding media, and shell thickness. An experiment in which the photon excitation energy was identical to that used here, 650 meV above the bandgap, and the sample preparation was consistent (dilute solution of NCs mixed with PMMA/toluene), the average truncation time for CdSe/ZnS NCs was <0.1 s at an average exciton formation of $\langle N_{ex} \rangle = 0.28$.[47] In comparison, at $\langle N_{ex} \rangle = 0.3$ in this experiment, the average truncation time was 1.61 s. Broadly, a reduction in α_{on} and an increase in τ_c suggest that $CsPbBr_3$ NCs tend toward longer on durations than traditional NC materials such as CdSe.

The cause of the truncation of power law kinetics can be investigated by examining the intensity dependence of the truncation time in more detail. The average inverse truncation time, $1/\tau_c$, is displayed as a function of excitation intensity in Figure 4.5a. The x axis error bars include the error associated with measuring the average power and excitation spot size, while the gray shading in the y axis direction corresponds to the standard deviation in $1/\tau_c$. The data spread in $1/\tau_c$ can be partially attributed to the large sample size dispersity, as the absorption cross section of $CsPbBr_3$ NCs has been shown to vary linearly with the NC volume at 3.1 eV.[42] This is typical for NCs excited at energies far above the band-edge, as

the NC absorption spectrum converges into the bulk spectrum. Since the average number of excitons formed per pulse is proportional to the size-dependent cross section, changes in the NC volume directly propagate through to $\langle N_{ex} \rangle$.

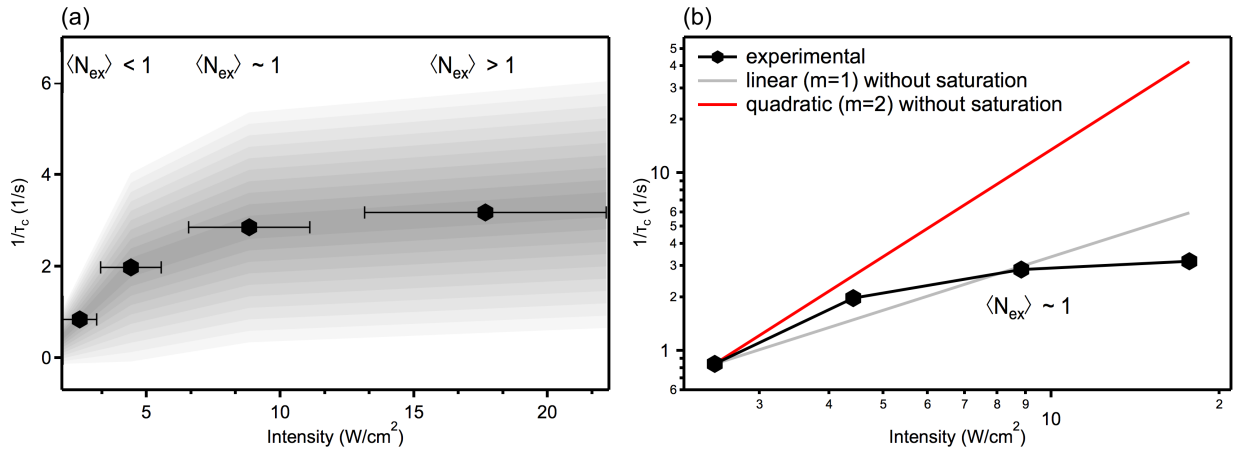

Figure 4.5: (a) Average inverse truncation time, $1/\tau_c$, at each I_{ex} used, with the error given by the gray shading. The regimes of excitation in terms of exciton formation are labeled. (b) Expected $1/\tau_c$ results shown without any saturation effect for a quadratic (red) and linear (gray) intensity dependence, shown with the experimentally measured values (black), on a logarithmiclogarithmic scale.

Therefore, the sample size dispersity is expected to be partially responsible for the large data spread at each intensity point in Figure 4.5a given that $1/\tau_c$ is dependent on $\langle N_{ex} \rangle$, which in turn is affected by the NC volume. Differences in the local dielectric environment surrounding each NC may be a contributor as well, namely the configuration of oleylammonium ligands and PMMA matrix surrounding each individual NC.

The average absorption cross section for 10 nm $CsPbBr_3$ NCs can be calculated using the volume scaling reported by Makarov et al.[42] A value of $\alpha_{abs}(\lambda = 400 \text{ nm}, 100 \text{ nm NC}) = 1.6 \pm 0.7 \times 10^{-14} \text{cm}^2$ is extracted, where the error takes into account the sample size dispersity of 15%.

This is comparable to an estimate obtained via scattering-corrected absorbance measurements, see Figure 4.6, using a double-beam UV-Vis spectrometer (purple curve), and solution concentrations determined by inductively coupled plasma optical emission spectrometry. To correct for scattering at shorter wavelengths, an integrating sphere with a white light source was used. The resulting absorption spectra (dashed red curve) include negative intensities in the PL region (green curve) due to the above bandgap light in the broadband source photo-exciting the NCs. Scattering-corrected absorption spectra are obtained (black curve)

by separating the PL from the absorption spectra, and averaging multiple spectra to smooth out the noise near and beyond 400 nm. The scattering-corrected and UV-Vis absorption spectra are compared to correlate the intensities and obtain an estimate of the extinction coefficient, which can then be converted into an absorption cross-section. Using this method, an absorption cross section estimate of $\alpha_{abs}(\lambda = 400 \text{ nm}, 100 \text{ nm NC}) = 2.1 \pm 0.2 \times 10^{-14} \text{cm}^2$ is obtained. With use of the former cross section value, which is deemed to be more reliable, the average numbers of excitons created per pulse at the four intensities used in this experiment are $\langle N_{ex} \rangle \approx 0.3, 0.5, 1,$ and 2, and the features in Figure 4.5a can then be grouped into two regions: an increase in $1/\tau_c$ with increasing intensity at $\langle N_{ex} \rangle < 1$ and a saturation near $\langle N_{ex} \rangle \approx 1$.

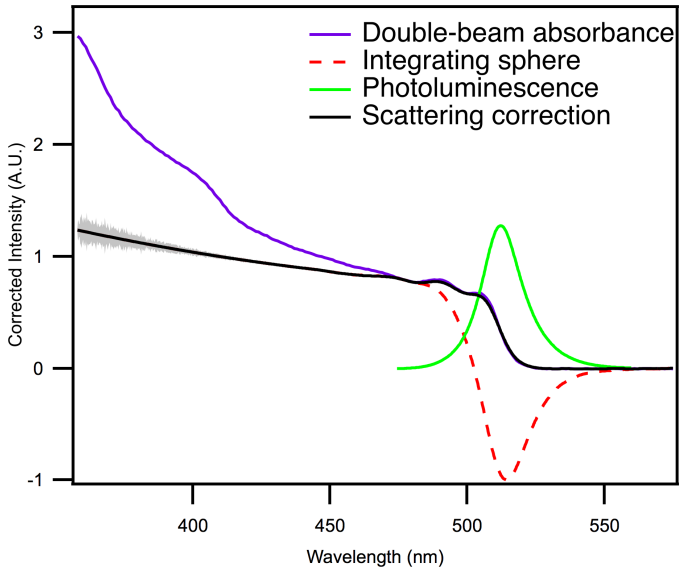

Figure 4.6: Spectral data used to estimate an absorption cross-section for 10 nm $CsPbBr_3$ NCs at 3.1 eV.

At the lowest intensities, extracting a precise value of m to determine the functional form $1/\tau_c \propto I_{ex}^m$ cannot be done with significance given there are only two data points; although, it does appear to be lower than m = 2. A quadratic dependence with m = 2, which has been observed experimentally in chalcogenide compositions, would suggest that the exponential truncation of power law kinetics is due to Auger autoionization of a biexciton, where the rate of biexciton formation scales quadratically with excitation intensity.[47,96] Conversely, the DCET model predicts a linear intensity dependence of the truncation time with m = 1,[78,82] which has also been observed experimentally.[44,97] Within the framework of the DCET model, a random walk along diffusing energy surfaces results in on↔off transitions when the neutral and charged energy surfaces intersect. The parabolic shape of the energy surfaces naturally

results in a saturation of the power law dynamics and leads to an exponential truncation, which is predicted to be inversely proportional to the diffusion time and thus to the intensity. The multiple recombination centers (MRC) model is a proposed mechanism that has successfully described the observed PL dynamics in NCs as well as nanorods, nanowires, and organic molecules in a glassy environment.[34,98] In the MRC model framework, a distribution of surface trap sites that randomly switch between active and inactive states gives rise to fluctuating trapping rates. While an intensity dependence is expected to exist, since the change in the trap conformation is assumed to be light-induced, the mechanism of this switching process has not been determined; therefore, the expected value of m and the expectation of any saturation of the truncation time is currently unknown for the MRC model. A physical underlying mechanism for the switching process would provide great insight into the relevance of this model to the results presented here, but as it is not presently available, the MRC model is excluded from further mechanistic considerations.

The expected results for both a linear and quadratic intensity dependence with no added saturation are shown in Figure 4.5b, along with the experimentally measured $1/\tau_c$ data. In the excitation regime of $\langle N_{ex} \rangle < 1$, it appears that $1 < m < 2$, which agrees with results reported at low intensities for $CsPbI_3$ NCs ($m = 1.3$).[86] This suggests that a combination of PL blinking mechanisms are responsible for the intensity-dependent results presented here. The role of multiexcitons cannot be ignored given the non-negligible probability of their formation (for example, 3% biexcitons per pulse at the lowest intensity used, calculated via a Poisson distribution[47]); however, if Auger autoionization was solely responsible for the power law truncation, a quadratic dependence with $m = 2$ should be observed. As the repetition rate used here allows NCs to be excited at even higher intensities without rapid photobleaching, a saturation can be observed in $1/\tau_c$ near $\langle N_{ex} \rangle \approx 1$. This behavior also contradicts what would be expected if the dominant mechanism were Auger autoionization, where such a substantial saturation should not occur until $\langle N_{ex} \rangle \approx 2$. Cordones et al. observed that CdSe/ZnS NCs exhibited a saturation in the off-state probability distributions at $\langle N_{ex} \rangle \approx 1$ and a saturation in the on-state truncation time at $\langle N_{ex} \rangle \approx 2$.[30] The DCET mechanism was invoked to explain the off-state saturation at a single exciton, while an Auger ionization mechanism was proposed to account for the on-state saturation at a biexciton.

In contrast, a DCET mechanism appears to be the likely trapping mechanism responsible for the on→off kinetics observed in $CsPbBr_3$ NCs. A small contribution from an Auger mechanism would account for the observed results at low intensities where $1 < m < 2$, but the dominant mechanism must be diffusion-based to account for the saturation behavior at $\langle N_{ex} \rangle \approx 1$. Furthermore, if Auger auto-ionization were assumed to be the only mechanism responsible for the on-state truncation, with the truncation time τ_c representing the lifetime for the ionization process, τ_c should be a function of the probability (based on Poisson statistics) of creating more than one exciton, $P(n \geq 2)$, as follows:

$$\tau_c = \frac{\Delta T}{P(n \geq 2)P(\text{ionize})} \tag{4.2}$$

where ΔT is the laser period and P(ionize) is the probability of ionization occurring. In Figure 4.7, the experimental τ_c values are plotted against $P(n \geq 2)$ along with the curve fit to the equation above. If Auger auto-ionization were the sole cause of the on-state truncation, τ_c should fall off much more rapidly than observed in these experiments.

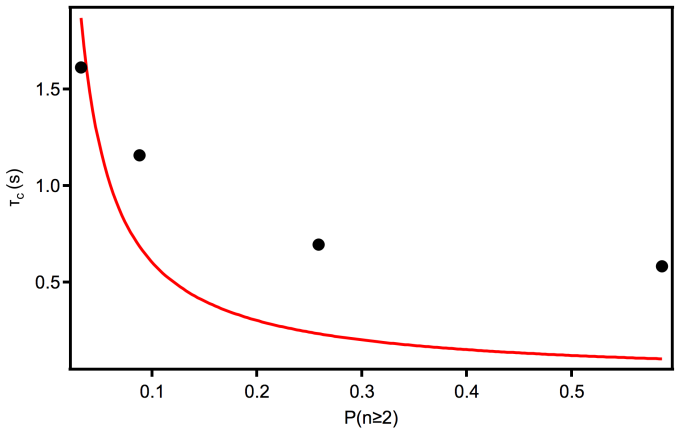

Figure 4.7: Experimental on-state truncation time values (black circles) plotted against the probability of multiexciton formation at the four excitation intensities used. Theoretical fit to the equation above (red line) if Auger auto-ionization were responsible for the power law truncation.

Several other reports have examined PL blinking in $CsPbX_3$ NCs of size similar to the NCs presented here, including at different excitation intensities, but the reported results have varied considerably.[83–86,99] Flickering of the PL has been reported, where the PL blinks between a bright state and a dim but not off state with short dim-time bursts of <60 ms,[84] while binary on-off blinking has also been reported.[86] Photoactivation at higher powers has been observed and attributed to light-induced structural reorganization[85] as well as rapid PL bleaching even at low excitation intensities.[86]

The lack of a cohesive picture of PL blinking and, in general, the charge dynamics in perovskite NCs highlights the need for further experimental and theoretical study. An analogous experiment to the one presented here could be carried out with lower photon excitation energies. Not only would this reduce the size dependence of the absorption cross section, but the experiments would create charge carriers that are less hot. In the present experiment, the excess photon energy is 650 meV, so PL blinking dynamics obtained with an excitation energy closer to the band-edge could provide insight into the role of hot carriers in perovskite NCs. The evolving synthetic field can also extend the experimental capabilities. For

example, the addition of a passivating shell would provide a barrier to charge ejection, likely extending the on durations and tuning the PL blinking behavior. New ligands that provide more passivating coverage of the NC surface will also affect the carrier dynamics. In addition, achieving higher monodispersity should produce trends with greater certainty, while new stabilization and dispersion techniques will allow for a comparison between polymer and polymer-free external environments.

4.5 Conclusions

In contrast to chalcogenide NCs, perovskite $CsPbBr_3$ NCs in only the weak confinement regime and without a passivating shell display bright PL that can largely be attributed to the material's inherent defect tolerance. In this work, PL trajectories were recorded for over 130 $CsPbBr_3$ perovskite NCs using a range of excitation intensities ($\langle N_{ex} \rangle = 0.3 - 2$). Minimal photobleaching due to the low repetition rate laser combined with the use of the changepoint analysis method were important to achieve a reliable extraction of kinetics. The on-state probability distributions at all intensities yielded an average $\alpha_{on} < 1.2$ and $1/\tau_c > 0.5$ s, revealing that perovskite NCs tend toward longer on durations than traditional chalcogenide NC compositions. In the excitation regime of $\langle N_{ex} \rangle < 1$, the on-state truncation time decreases with increasing excitation intensity according to $1/\tau_c \propto I_{ex}^m$, where $1 < \mathrm{m} < 2$. A saturation is observed near $\langle N_{ex} \rangle \approx 1$, indicating that the on$\rightarrow$off trapping process is most likely dominated by a DCET blinking mechanism, with a smaller contribution from Auger autoionization. Continued experiments and theoretical studies are required to investigate the mechanism of PL blinking in defect tolerant semiconductor NCs such as the lead halide perovskites, and more broadly, to understand how these materials compare to traditional semiconductors.

Chapter 5

Charge Carrier Dynamics in Semiconductor Nanowires and Nanoplates

Chapters 3-4 described photoluminescence (PL) studies of single semiconductor 0-D nanocrystals (NCs) using the setup outlined in Chapter 2. Nanostructures of other dimensionalities can also be investigated using the same tools with only slight modifications to the setup. In this chapter, PL measurements on 1-D nanowires (NWs) and NW arrays are summarized. Section 5.1 presents time-resolved and spectral measurements on cesium lead halide perovskite nanowires capable of lasing at room temperature. The same composition of NWs but in colloidal bundles are the focus of the time-resolved measurements in Section 5.2. Finally, time-resolved studies of wurtzite indium phosphide NW arrays are discussed in Section 5.3.

5.1 Lasing in Robust Cesium Lead Halide Perovskite Nanowires

Nanoscale lasers are miniaturized photonic devices that are promising light sources for optoelectronic applications. They can offer high performance and flexibility, and facile fabrication and manipulation. In 1-D semiconductor NWs, the gain medium is provided by the wire itself and requires a highly absorptive and emissive material. The large difference in refractive index between the NW material and the external environment leads to end facet reflectivity, forming a built-in laser cavity and generating wave guiding along the wire length.[100] Lead halide perovskites are attractive materials for nanoscale lasers given their emission

wavelength tunability achieved by altering the halide composition. Organic-inorganic lead halide perovskite NWs, $CH_3NH_3PbX_3$ (X = Cl, Br, I), have demonstrated low lasing thresholds, high quality (Q) factors, and wavelength tunability through halide substitution and alloying.[71] Their intrinsic lack of stability due to their susceptibility to hydrolysis from atmospheric water can be improved by using a less reactive cation such as cesium. Towards this end, single-crystal $CsPbX_3$ (X = Br, Cl) NWs and nanoplates were grown in solution by dipping a PbI_2 thin film into a CsX-methanol solution with mild heating (50°C). The NWs ranged in length from 2 to 40 μm and in width from 0.2 to 2.3 μm.

NWs with clean, well-formed facets were transferred to a clean, fused silica coverslip using a micromanipulator and secured in N_2-gas-filled cells that were mounted in the microscope. A widefield configuration (as described in Chapter 2) with a 50×, 0.50-numerical aperture (NA) air objective (Olympus LMPLFLN) was used to produce a large spot size of 29 ± 4 μm to uniformly illuminate single NWs. High-resolution color images were recorded using a charge-coupled device (CCD) (MRc 5, AxioCam). Spectral PL measurements were acquired with a fiber coupled UV-Vis spectrometer (Spectra Pro-300i, Acton) with a 300-nm blaze angle, 1200 mm^{-1} grating, equipped with a liquid-N_2-cooled CCD (7346-0001, Roper Scientific) for a spectral resolution of 0.06 nm. Time-resolved PL (TRPL) measurements were performed using the APDs and TCSPC setup described in Chapter 2.

For $CsPbBr_3$ NWs, lasing was achieved via optical excitation from a femtosecond pulsed laser. At excitation densities below the lasing threshold, spontaneous emission dominates, and the NW is uniformly emissive as shown in Figure 5.1B. Upon surpassing the threshold, however, stimulated emission takes over and a periodic emission pattern is observed (Figures 5.1 C and D), which is caused by interference of the coherent emission from the two end facets of the NW. The dependence of the PL spectral response on increasing excitation fluence is shown in Figure 5.1E.

The spontaneous emission from a $CsPbBr_3$ NW is centered at 516 nm with a 16-nm (74 meV) full-width-at-half-maximum (fwhm). The spontaneous emission peak first increases with increasing excitation intensity, then plateaus as narrow, closely spaced lasing peaks (0.5-nm minimum fwhm) emerge on the red edge of the emission spectrum near 532 nm and grow rapidly with excitation intensity. The narrow peaks correspond to Fabry-Pérot lasing modes as the mode spacing is found to change linearly with the inverse of the NW length (Figure 5.1F, *Inset*). The power-dependent output intensity (Figure 5.1F) follows the typical "S"-curve shape and depicts all three PL regimes: spontaneous emission dominates at low excitation intensities until the onset of lasing near 5 μJ cm^{-2} (P_{th}), the superlinear PL increase indicative of amplified spontaneous emission follows, and finally gain-pinning and the emergence of lasing occurs past 10 μJ cm^{-2}.[101] Analysis of the individual peak widths from the spectra in Figure 5.1E provides information about the NW laser cavity Q factor, or how well the cavity confines and amplifies emission. The Q factor is mode dependent with stronger modes possessing higher values because this corresponds to more efficient am-

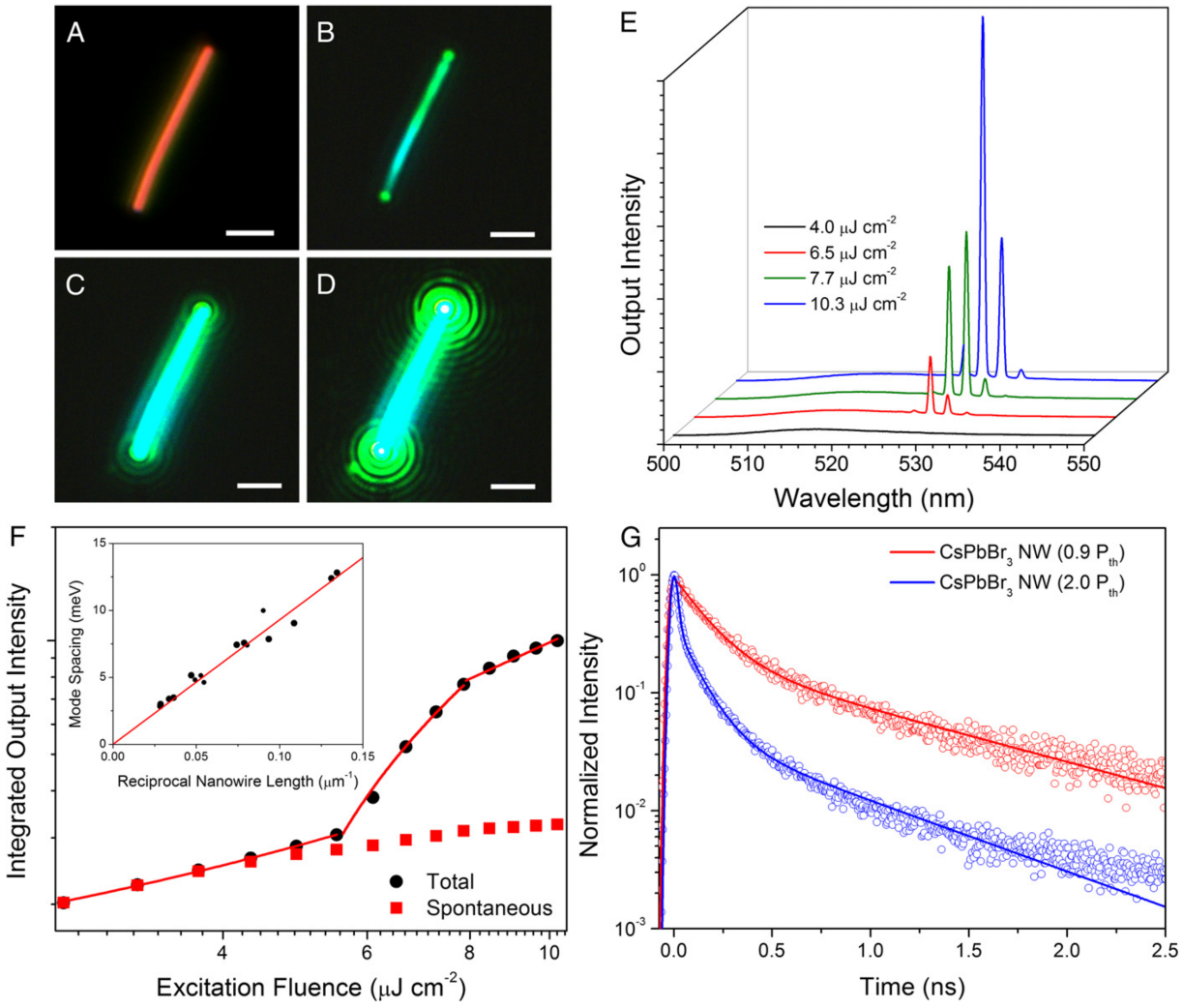

Figure 5.1: Lasing in single-crystal $CsPbBr_3$ NWs. (A) Dark-field image of a $CsPbBr_3$ NW. (B-D) The NW from A under excitation from a femtosecond pulsed laser with increasing excitation fluence. (Scale bar, 2 μm.) (E) Power-dependent emission spectra from the $CsPbBr_3$ NW shown in images A-D. Narrow emission peaks at $\sim$ 530 nm are indicative of lasing. (F) The integrated output intensity of the $CsPbBr_3$ NW with increasing pump fluence (black circles) follows a typical S-curve pattern and can be linearly fit to show three separate emission regimes: spontaneous emission ($<$ 5 μJ cm^{-2}), amplified spontaneous emission (5-10 μJ cm^{-2}), and lasing ($>$ 10 μJ cm^{-2}). Spontaneous emission (red squares) from the NW plateaus as stimulated emission begins to dominate. *(Inset)* Plot of inverse NW length against mode spacing, confirming that Fabry-Pérot-type lasing is dominant. (G) TRPL from a $CsPbBr_3$ NW below (red) and above (blue) the lasing threshold (P_{th}). The emergence of a rapid decay component ($<$ 10 ps) suggests rapid carrier quenching due to stimulated emission.

plification and thus higher emission intensity. Using the relationship $Q = \lambda/\delta\lambda$, where λ is the peak center wavelength and $\delta\lambda$ is the peak width, a maximum, single-mode Q factor of $1,009 \pm 5$ was determined with an average of 960 ± 60 when considering the four major modes (Figure 5.2).

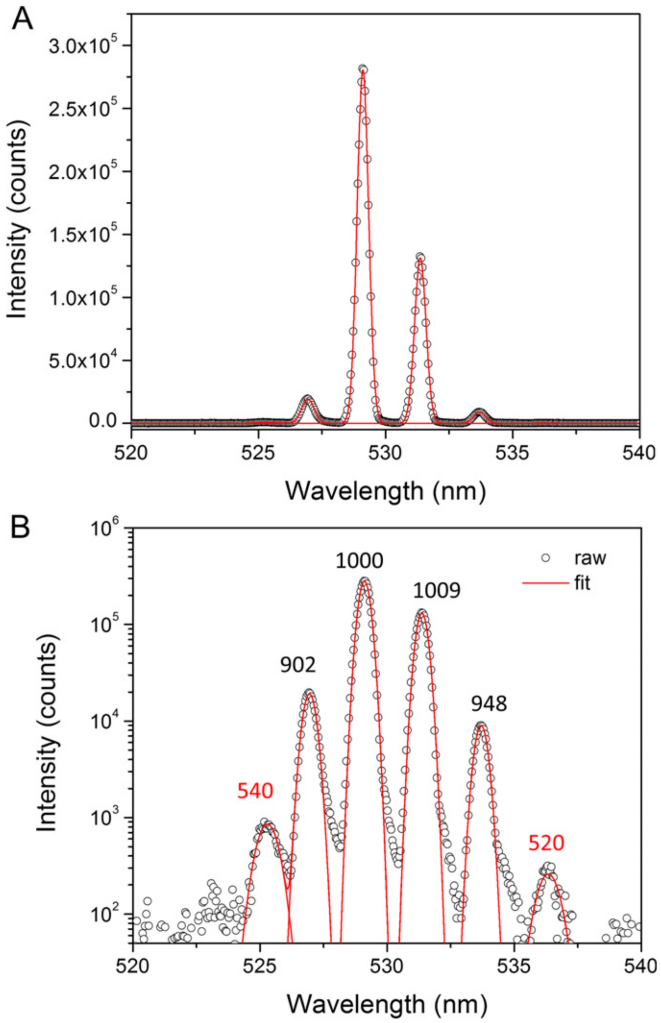

Figure 5.2: Q-factor analysis of a $CsPbBr_3$ NW. (A) A linear plot of the emission spectrum at 10.3 μJ cm^{-2} from Figure 5.1E is shown with Gaussian fits of each lasing mode. The spontaneous emission has been subtracted for clarity and ease of fitting. (B) The same spectrum and fit plotted on a log scale showing the quality of the fit. Peak annotations correspond to the Q factor for the specific peak.

TRPL can be used to measure the carrier population dynamics of the laser cavity above and below the lasing threshold. Below the lasing threshold (Figure 5.1G, red trace), the NW

PL signal decays biexponentially with the rapid component (154 ± 2 ps, 81%) contributing much more than the slower component (970 ± 20 ps, 19%). Based on preliminary TRPL measurements of previously reported, surface-passivated, colloidal $CsPbX_3$ (X = Cl, Br, I) NWs, which exhibit much longer lifetimes (>>1 ns), the rapid component is attibuted to surface state recombination and the longer component to bulk recombination.[102] When the excitation fluence is increased past the lasing threshold, an additional decay component is observed (< 30 ps, 87%), which decays more rapidly than the other components (110 ± 2 ps, 11%; 720 ± 20 ps, 2%) as well as the instrument response. This rapid decay corresponds to the stimulated emission process depleting carriers that would otherwise undergo spontaneous emission. The low-lasing threshold and high Q factor place these NWs in the upper tier of NW lasers and clearly demonstrate the effectiveness of $CsPbBr_3$ as a gain medium (see references[100,103,104] for detailed lists of NW lasers and their performance characteristics).

The mechanism for optical gain by stimulated emission in perovskite nanostructures is still under investigation. In $CsPbX_3$ (X = Cl, Br, I) NCs, support for both single exciton and biexciton lasing has been demonstrated.[104,105] In the case of biexciton-driven stimulated emission, a 50-meV red-shifted emission band was assigned to biexciton recombination, in agreement with expected biexciton binding energies in $CsPbX_3$ NCs.[106] Whereas a similar asymmetric red-shifted emission band is observed at 290 and 6 K (Figure 5.3), the red shift of 69 meV is an order of magnitude larger than expected for biexciton binding energies in non-quantum confined $CsPbBr_3$ NWs. Instead, an electron-hole plasma (EHP) mechanism is postulated to be responsible for stimulated emission, as proposed in well-known compositions such as ZnO[107] and GaN[108] as well as in recent $CH_3NH_3PbX_3$ (X = Cl, Br, I) NWs.[71] An EHP is formed in bulk crystals when the carrier density surpasses the Mott density; here, the carrier density at the lasing threshold was estimated to be $\sim 6 \times 10^{17}$ cm^{-3} by finite-difference time-domain simulations, a factor of 3 greater than the bulk $CsPbBr_3$ Mott density of $\sim 2 \times 10^{17}$ cm^{-3}. In addition, the formation of an EHP is expected to lead to a blueshift in the cavity modes due to a decrease in the refractive index that arises from exciton absorption saturation.[107] A blueshift of 2 nm is observed with increasing excitation fluence (Figure 5.4), suggesting that an EHP mechanism is responsible for stimulated emission in $CsPbBr_3$ NWs. Further study is needed, however, to conclusively elucidate the stimulated emission carrier dynamics.

Cesium lead halide materials have been shown to be stable when exposed to atmospheric water or heat, making them attractive for real-world application.[105,109] The $CsPbBr_3$ NWs reported here are stable for days under ambient atmosphere and illumination without loss of morphology. Additionally, the material composition remains intact over the course of months and does not separate into $PbBr_2$ and other byproducts as has been demonstrated for some hybrid perovskite materials (Figure 5.5A).[110] $CsPbBr_3$ NWs are also stable under constant, pulsed excitation above the lasing threshold. NWs were excited to 1.2 P_{th} under either a closed nitrogen atmosphere or ambient atmosphere ($26°C \pm 0.5°C$, $50\% \pm 1\%$ relative humidity) and the integrated emission intensity was monitored. The results shown in Fig-

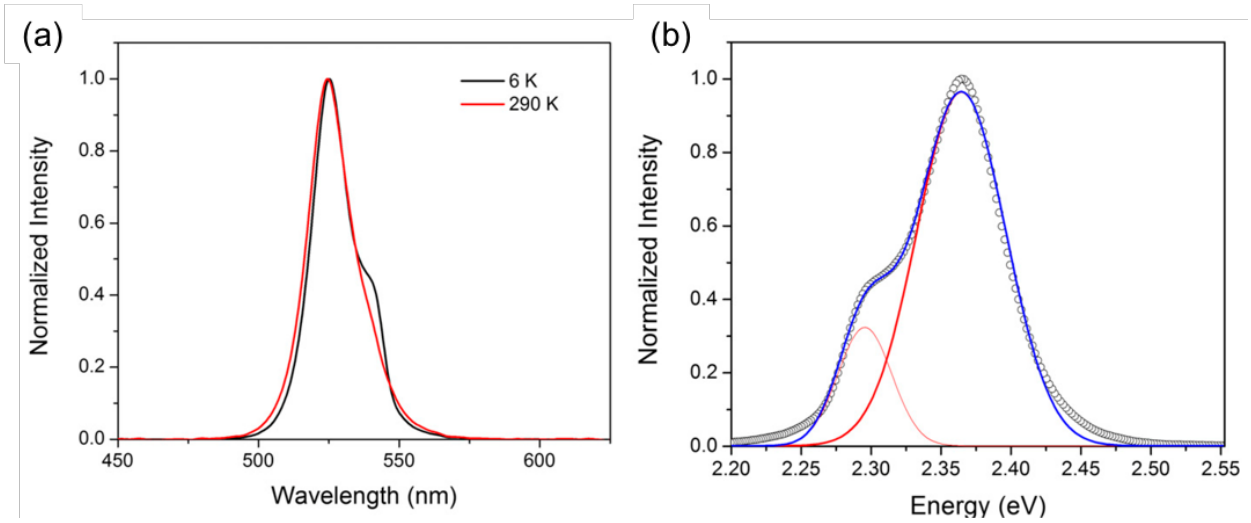

Figure 5.3: Low-energy emission band in $CsPbBr_3$ NWs. (A) $CsPbBr_3$ NW emission at room temperature (290 K) and low temperature (6 K) shows the growth of the low-energy band. (C) The low-temperature emission spectrum may be fit to a pair of Gaussians (red) that are 69 meV apart.

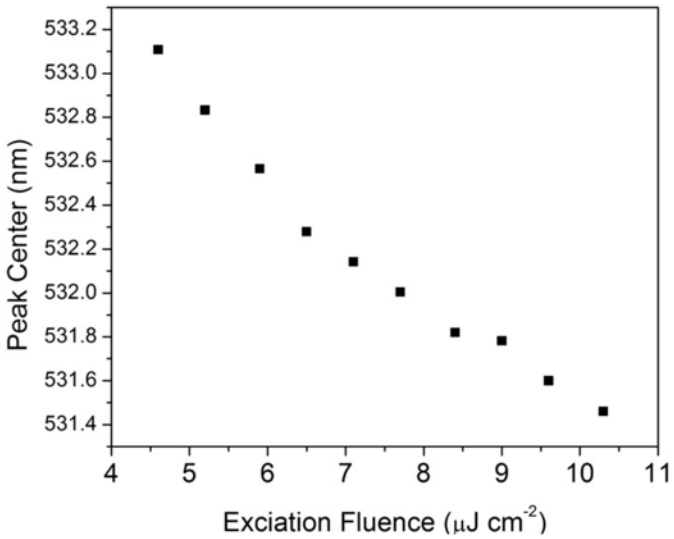

Figure 5.4: Peak center of the most intense lasing mode as a function of excitation fluence, demonstrating a 2 nm blueshift.

ure 5.5B indicate significant operating lifetimes even under atmospheric conditions. Under nitrogen, NW lasing continues uninterrupted for longer than 1 h or over 10^9 excitation cycles (Figure 5.5B, blue trace), with the NW undamaged after this time. Under atmospheric conditions, lasing output is observed to decrease over the course of the experiment, but it does not fall below the original output until over 4.4×10^8 excitation cycles (Figure 5.5B, red trace). In contrast, amplified spontaneous emission from thin films of $CsPbBr_3$ falls to 90% after only 1.6×10^7 excitation cycles.[104] In hybrid perovskite materials, whispering gallery mode lasing in $CH_3NH_3PbI_3$ persists for 8×10^6 excitation cycles,[111] whereas the long-term lasing stability of $CH_3NH_3PbX_3$ (X = Cl, Br, I) NWs lasers has not been reported.[71] The stable, continuous lasing operation observed here is promising for future applications as it suggests both high photo- and thermal stability under ideal or suboptimal environmental conditions.

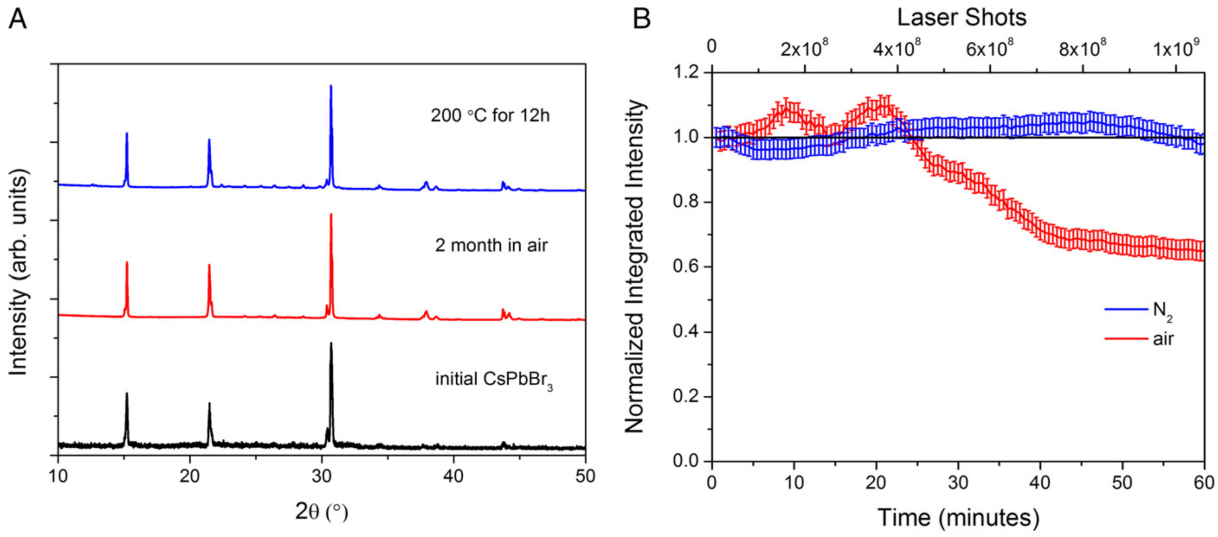

Figure 5.5: Stability of $CsPbBr_3$. (A) XRD patterns of as-grown $CsPbBr_3$ before testing (black), after exposure to air for 2 mo (red), and after annealing at 200°C (blue). In both cases, the $CsPbBr_3$ phase remained identical to the as-grown and indicated high compositional stability. (B) Integrated emission intensity for $CsPbBr_3$ NWs under constant pulsed excitation (1.2 P_{th}) while exposed to nitrogen (blue) and ambient atmosphere (red).

Lasing is also possible for other compositions and geometries besides $CsPbBr_3$ NWs. Single-crystal NWs of $CsPbCl_3$ were successfully synthesized by replacing CsBr with CsCl during the reaction. The smooth, rectangular facets of the $CsPbCl_3$ NWs, as well as the strong PL emission centered at 418 nm, make them ideal for extending the wavelength range of lead halide perovskite NW lasers. Upon focused excitation, lasing occurred near 430 nm with the emergence of narrow peaks similar to $CsPbBr_3$ NWs as shown in Figure 5.6A. The

lasing threshold was found at $\sim$ 86 μJ cm^{-2}, significantly higher than for $CsPbBr_3$ NWs, and the Q factor was consequently found to be lower, with a maximum of 690 ± 70 and an average of 580 ± 120. Nevertheless, interference from end facet emission was observed (Figure 5.6A, *Inset*), indicating effective waveguiding and coherent emission from the NW. Halide alloying may be pursued in the future to achieve broad wavelength tunability. In addition to NWs, well-faceted $CsPbBr_3$ nanoplates (NPLs) were found to lase at $\sim$ 38 μJ cm^{-2} with the power-dependent emission spectra shown in Figure 5.6B. Despite the high mode density, peak fitting yields a mode spacing of 3.9 ± 0.7 meV (Figure 5.7), which for a 19.3-μm-long plate falls within error of the fit line shown in Figure 5.1F *(Inset)*. This suggests Fabry-Pérot lasing from multiple transverse modes, which may be easily supported by the broad, rectangular plate. This assignment is further supported by the stronger emission intensity observed at one pair of end facets indicating a preference for lasing in that direction (Figure 5.6B, *Inset*). This lasing behavior is in contrast to whispering gallery mode lasing observed in 100-μm-sized plates of $CsPbBr_3$, which demonstrated broad peak spacing and a uniform spatial emission profile.[104]

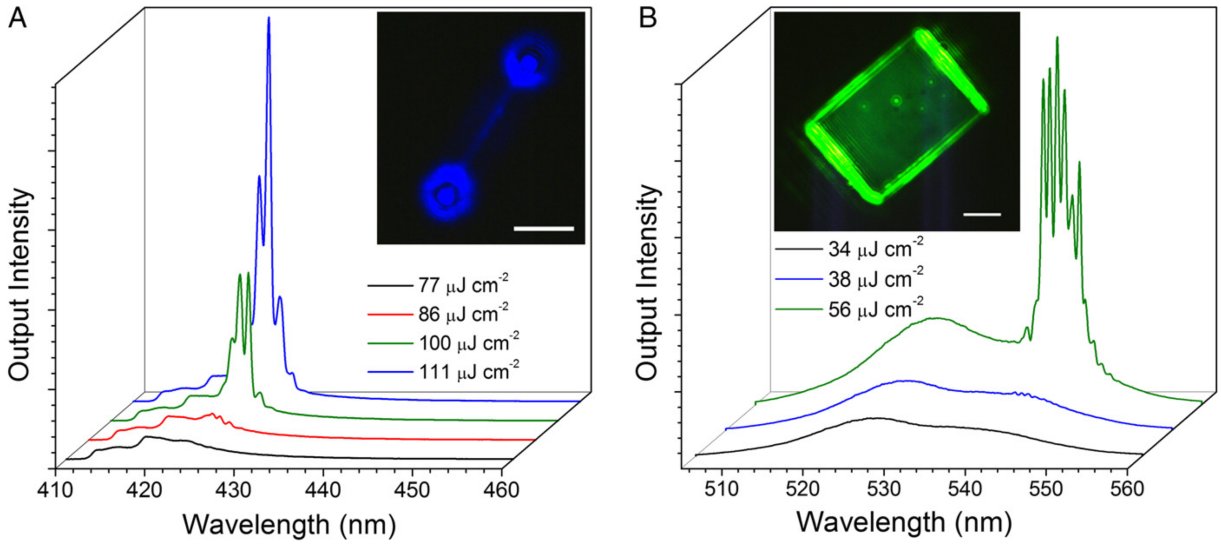

Figure 5.6: Lasing in $CsPbCl_3$ NWs and $CsPbBr_3$ NPLs. (A) $CsPbCl_3$ NW power-dependent emission spectra showing lasing at ∼425 nm. *(Inset)* Optical image of the same NW above the lasing threshold. (Scale bar, 5 μm.) (B) $CsPbBr_3$ NPL power-dependent emission spectra showing lasing at ∼545 nm. *(Inset)* Optical image of the same NPL above the lasing threshold. (Scale bar, 5 μm.)

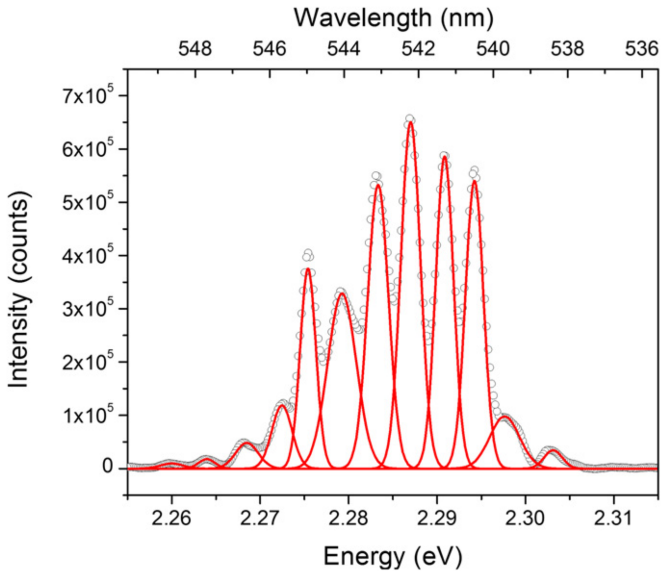

Figure 5.7: PL spectrum of the $CsPbBr_3$ NPL in Figure 5.6B at 56 μJ cm^{-2} fit to 12 Gaussian functions. The spontaneous emission has been subtracted for clarity and ease of fitting. The mode spacing suggests Fabry-Pérot-type lasing.

5.2 Time-Resolved Photoluminescence of Colloidal Cesium Lead Halide Nanowires

In this section, TRPL measurements on the colloidal versions of cesium lead halide ($CsPbX_3$, X = Cl, Br, I) NWs are discussed. In contrast to the NWs presented in the preceeding section, these wires are too narrow (< 20 nm) to support photonic lasing, which requires diameters > 180 nm.[70] The experimental techniques available in this setup are valuable for studying the effect of surface defects on the recombination dynamics.

Based on a previously reported method[102] but with octylamine surfactant, colloidal $CsPbBr_3$ NWs with uniform diameters of 10 ± 2 nm were synthesized with a 90% purity.[112] By reacting the $CsPbBr_3$ NWs with iodide and chloride precursors under air-free conditions, a wide range of alloy compositions were synthesized through anion-exchange reactions. The morphology and crystal structure were well-preserved (see Figure 2 in ref. [112]), and PL quantum yields ranging from 20% to 80% were achieved.[112] Solutions of the NWs dispersed in hexane were spin-cast onto fused silica coverslip substrates and secured in N_2-gas-filled cells that were mounted in the microscope. A confocal configuration was used with the 100×, 1.3-NA oil objective and the detectors described in Chapter 2. TRPL decays were acquired (5 min acquisition time, 4-16 ps resolution) for bundles of the pure $CsPbBr_3$ NWs as well as several alloy compositions, two $CsPb(Br/Cl)_3$ and two $CsPb(Br/I)_3$ alloys.

All TRPL measurements were best fit to a biexponential decay function:

$$I(t) = A_1 e^{-t/\tau_1} + A_2 e^{-t/\tau_2} \tag{5.1}$$

At least six measurements of separate wire bundles were acquired, more if a large spread in the results was present. The fit parameters for each sample are summarized in Table 5.1 and representative TRPL decays are shown in Figure 5.8 (the 'Alloy 2' samples are more rich in Cl or I than the 'Alloy 1' samples).

Table 5.1: TRPL Fit Parameters for $CsPbBr_3$ and Alloy NW Bundles.

Sample	PL Peak (nm)	τ_1 (ns)	τ_2 (ns)	Amplitude 1	Amplitude 2
$CsPb(Br/Cl)_3$ Alloy 1	430	0.94	4.46	0.84	0.16
$CsPb(Br/Cl)_3$ Alloy 2	481	1.48	9.07	0.77	0.23
$CsPbBr_3$	519	1.22	3.55	0.74	0.26
$CsPb(Br/I)_3$ Alloy 1	586	1.70	11.78	0.78	0.22
$CsPb(Br/I)_3$ Alloy 2	663	2.31	50.39	0.64	0.36

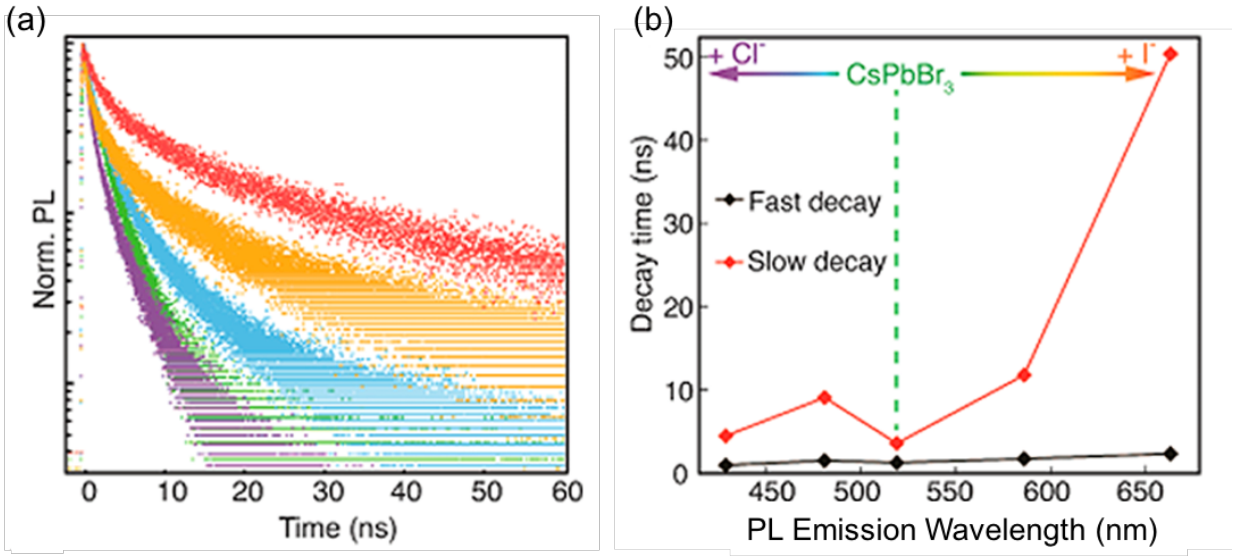

Figure 5.8: TRPL of $CsPbBr_3$ and alloy NWs. Purple=$CsPb(Br/Cl)_3$ Alloy 1; blue=$CsPb(Br/Cl)_3$ Alloy 2; green=$CsPbBr_3$; orange=$CsPb(Br/I)_3$ Alloy 1; red=$CsPb(Br/I)_3$ Alloy 2.

The amplitudes remain fairly consistent between all compositions, with the slow decay component τ_1 contributing about three times as much ($\sim 75\%$) as the rapid decay component τ_2 ($\sim 25\%$). The lifetimes τ_1 and τ_2 likely correspond to surface site and bulk recombination,

respectively. If the quality of the surface was severely compromised during an anion exchange reaction, the alloy NWs would likely have faster τ_1 decays and/or an increase in the contribution of τ_1. An examination of Table 5.1 instead reveals nearly constant amplitudes across all compositions and a longer τ_1 in all but one composition ($CsPb(Br/Cl)_3$ Alloy 1) where it is slightly shorter. This implies that the anion exchange reactions did not increase the degree of defect-related recombination. Figure 5.9 offers a summary of the decay components in the measured TRPL of the colloidal cesium lead halide NWs.

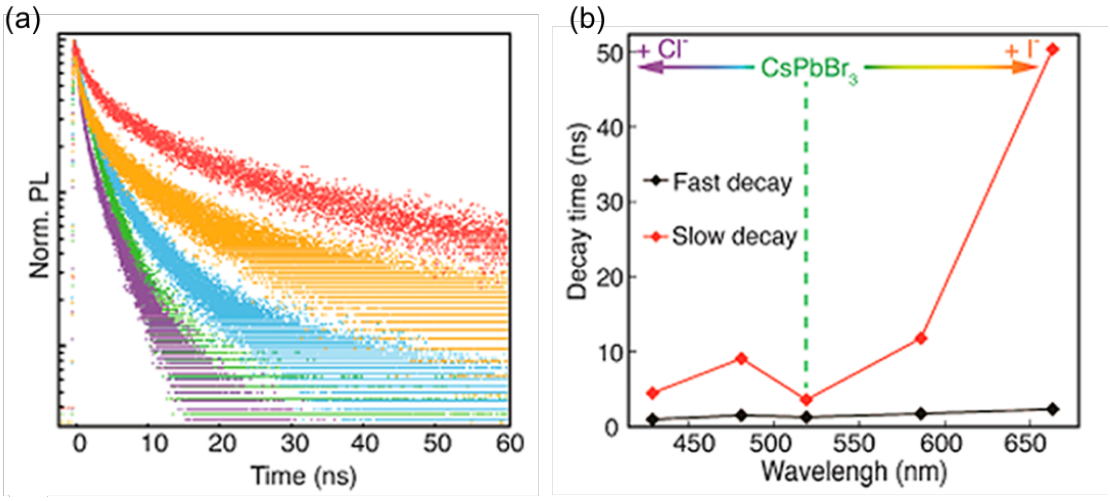

Figure 5.9: (a) TRPL decays and (b) lifetimes of $CsPbBr_3$ and anion-exchange alloy NWs.

5.3 Time-Resolved Photoluminescence of Wurtzite Indium Phosphide Nanowire Arrays

In this final section, TRPL measurements are performed on indium phosphide (InP) NWs and Zn-doped InP NWs to probe the excited state recombination dynamics of the as-grown NWs as well as the effect of the Zn doping on the recombination dynamics. Wurtzite InP NW arrays were grown on p-type $\langle 111 \rangle$ silicon substrates with a metal-organic chemical vapor deposition process, incorporating trime-thylindium and tert-butylphosphine as In and P precursors, respectively.[113] Doping with Zn, a p-type dopant, was performed via thermal annealing using zinc phosphide powder; the doped InP NWs were then implemented as light-absorbing photocathodes in photoelectrochemical cells.[113]

TPRL decays were measured for the as-grown and Zn-doped NWs across six orders of magnitude of excitation intensity. The decay curves were best fit to a biexponential function (Equation 5.1) for all NWs. As in Section 5.2, the rapid lifetime component τ_1 likely corresponds to surface related recombination (contributed to 70-80% of the decay) and the slow

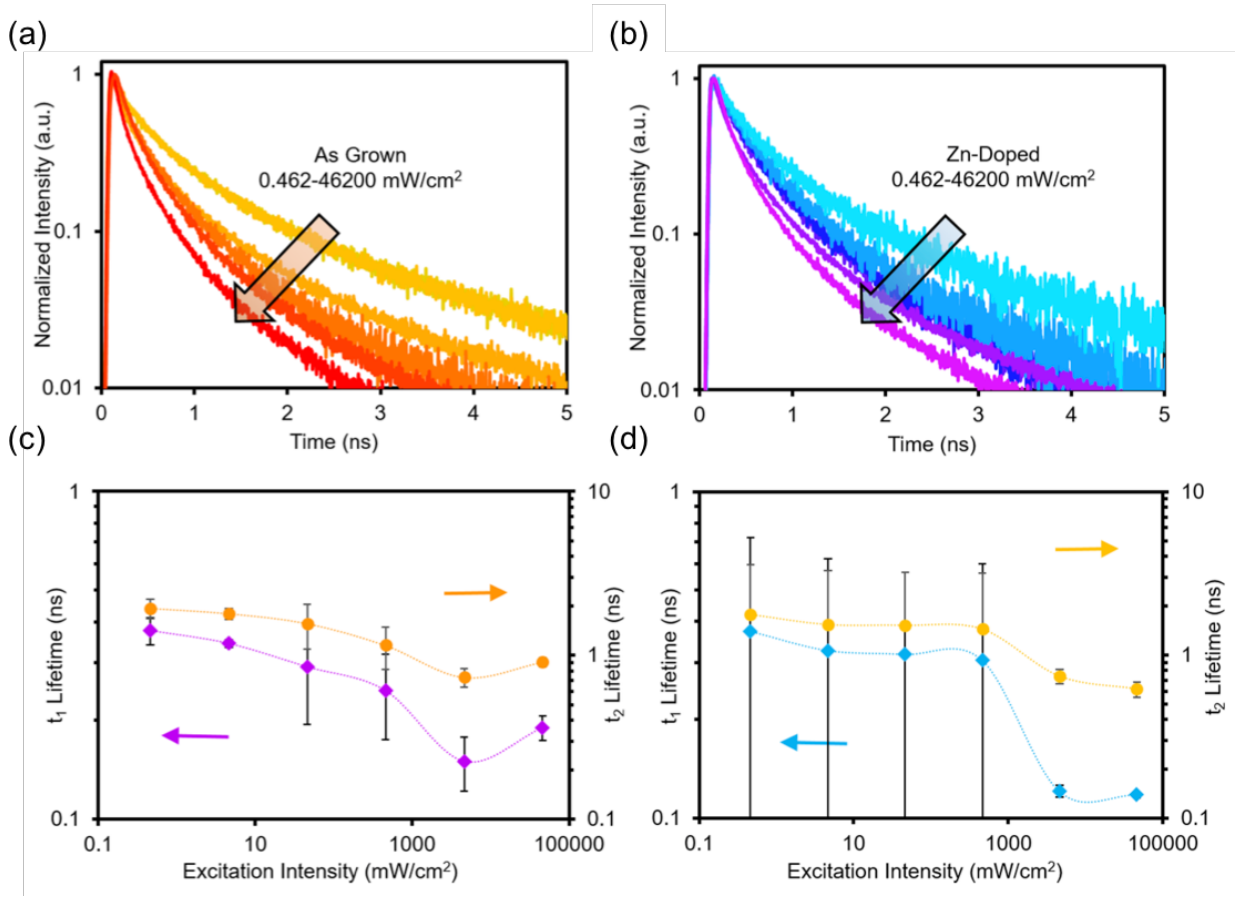

Figure 5.10: TRPL decays of the as-grown (a) and Zn- doped (b) NWs, exhibiting a decrease in both lifetime components with increasing excitation intensity. Average τ_1 and τ_2 values for the as-grown (c) and Zn- doped (d) NWs. The error bars represent one standard deviation from three and eight samples of the undoped and Zn-doped NWs, respectively.

lifetime component τ_2 to bulk recombination (contributed to 20-30% of the decay). As the excitation intensity was increased from 0.462 to 46200 mW/cm^2, the lifetime of both components decreased (Figures 5.10a,b) for the as-grown and Zn-doped NWs. This suggests that as the intensity is increased, trap states, likely on the surface, are filled and multiexciton processes accelerate the recombination kinetics. The as-grown NWs show more consistent behavior than the Zn-doped NWs, which exhibit a much larger spread in their τ_1 and τ_2 values (see Figures 5.10c,d and 5.11). This result is indicative of the thermal annealing doping process leading to Zn-doped InP NWs that are more heterogeneous than the as-grown wires.

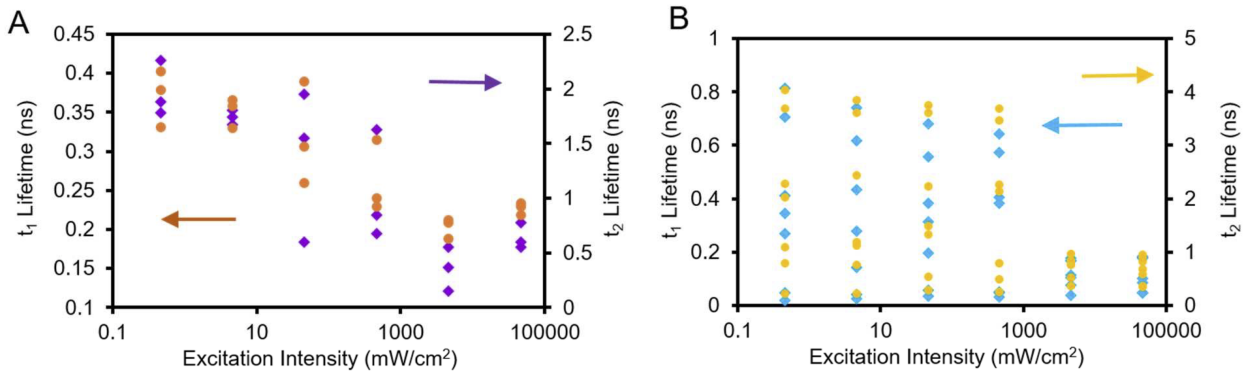

Figure 5.11: TRPL lifetime distributions of as-grown (A) and Zn-doped (B) InP NWs.

Chapter 6

Summary and Outlook

Probing the photoluminescence (PL) or fluorescence emitted from an optically excited semiconductor nanoparticle is an extremely informative way of studying charge carrier dynamics in this class of materials. In particular, time-resolved studies of the PL emitted from a single nanoparticle are extremely valuable, as the removal of ensemble averaging reveals new phenomena that are only detectable on the single particle level. The bulk of this dissertation describes the use of single particle spectroscopy to probe charge carrier dynamics in semiconductor nanocrystals (NCs). The PL intensity of a single semiconductor NC fluctuates between bright and dark periods of intensity over time. PL blinking, as it is referred to, relates directly to charge carrier trapping in NCs, although a comprehensive, detailed mechanism to relate the underlying dynamics to PL blinking has yet to account for all observations.

PL blinking in thick-shell CdSe/CdS core/shell NCs is analyzed using the changepoint analysis (CPA) and the traditional bin-and-threshold methods, the latter of which assumes only one bright, on state and one dark, off state exist. This two-level assumption can be avoided using CPA, and as such, it is found to be more accurate to study the kinetics in NCs that display multilevel emission. PL blinking is investigated in lead halide perovskite $CsPbBr_3$ NCs to uncover the excitation intensity dependence of the on-state kinetics, through the use of the CPA analysis method once more. The perovskite NCs tend towards longer on durations than traditional chalcogenide NC compositions, and the intensity-dependent results suggest that a diffusion-controlled electron transfer mechanism dominates the on$\rightarrow$off trapping dynamics, with a smaller contribution from Auger autoionization. Lastly, room-temperature lasing in single lead halide perovskite $CsPbBr_3$ nanowires (NWs) is studied and time-resolved PL decays of colloidal $CsPbX_3$ (X = Cl, Br, I) NWs and wurtzite InP NWs are measured.

When this lab was first built over a decade ago, many of the most important PL blinking experiments and new theoretical models to account for blinking observations had yet to emerge. Our understanding of how the underlying charge carrier dynamics in semiconductor NCs can lead to power-law distributed kinetics in their PL trajectories has greatly improved

over this time, to which the former researchers in this lab contributed greatly. The ability to perform single particle experiments using commercial, low-cost ("black-box") picosecond lasers and the continued improvements on the PL quantum yield (PLQY) of NCs has led to a proliferation in the number of research groups contributing to this field. Presently there is a wealth of knowledge available, in particular for the prototypical CdSe, which has led to such significant synthetic advances that commercial display applications have even been realized in the past few years.

In the future, there will undoubtedly be many more important contributions to the field of PL blinking, including in new NC compositions. As the nanoscience field has evolved, the ability for chemists and material scientists to synthesize brand new compositions of NCs, and achieve high PLQYs within a short amount of time following the first synthesis, has led to many recent compositions of bright NCs whose photophysics have yet to be thoroughly investigated. Perovskites are one such example, but the future will likely see many other new compositions of NCs to explore as well. In particular, improvements to the PLQY of transition-metal dichalcogenide NCs will make it more feasible to study them on a single particle level. NC heterostructures are also likely to provide interesting, new territory to explore. Future experiments in these directions will surely lead to exciting, new science being discovered.

Bibliography

(1) Neamen, D. A., *Semiconductor Physics and Devices: Basic Principles*, Third; McGraw-Hill: New York, 2003.

(2) National Nanotechnology Initiative. What is Nanotechnology?, https://www.nano.gov/nanotech-101/what/definition (accessed 07/19/2018).

(3) Calderón-Jiménez, B.; Johnson, M. E.; Montoro Bustos, A. R.; Murphy, K. E.; Winchester, M. R.; Vega Baudrit, J. R. Silver Nanoparticles: Technological Advances, Societal Impacts, and Metrological Challenges. *Front. Chem.* **2017**, *5*, 1–26.

(4) ICIS. Titanium Dioxide (TiO_2) Uses and Market Data., https://www.icis.com (accessed 07/19/2018).

(5) Alivisatos, A. P. Semiconductor Clusters, Nanocrystals, and Quantum Dots. *Science* **1996**, *271*, 933–937.

(6) Gaponenko, S. V., *Optical Properties of Semicondcutor Nanocrystals*; Cambridge University Press: Cambridge, 1998.

(7) Brus, L. E. Electron-electron and electron-hole interactions in small semiconductor crystallites: The size dependence of the lowest excited electronic state. *J. Chem. Phys.* **1984**, *80*, 4403–4409.

(8) Kittel, C., *Introduction to Solid State Physics*, Eighth; John Wiley & Sons: Hoboken, 2005.

(9) Maia, A. E.; Pires Filho, A.; Sampaio, A.; Freire, V. The Thermalization Process of Photoexcited Electrons and Holes in the Second Kinetic Stage of Relaxation. *Phys. Status Solidi* **1993**, *180*, 213–222.

(10) Schwartz, O.; Oron, D. A present understanding of colloidal quantum dot blinking. *Isr. J. Chem.* **2012**, *52*, 992–1001.

(11) Burda, C.; Link, S.; Mohamed, M.; El-Sayed, M. The relaxation pathways of CdSe nanoparticles monitored with femtosecond time-resolution from the visible to the IR: Assignment of the transient features by carrier quenching. *J. Phys. Chem. B* **2001**, *105*, 12286–12292.

(12) Klimov, V.; McBranch, D.; Leatherdale, C. A.; Bawendi, M. G. Electron and hole relaxation pathways in semiconductor quantum dots. *Phys. Rev. B* **1999**, *60*, 13740–13749.

(13) Hendry, E.; Koeberg, M.; Wang, F.; Zhang, H.; De Mello Donegá, C.; Vanmaekelbergh, D.; Bonn, M. Direct observation of electron-to-hole energy transfer in CdSe quantum dots. *Phys. Rev. Lett.* **2006**, *96*, 057408.

(14) Robel, I.; Gresback, R.; Kortshagen, U.; Schaller, R. D.; Klimov, V. I. Universal size-dependent trend in auger recombination in direct-gap and indirect-gap semiconductor nanocrystals. *Phys. Rev. Lett.* **2009**, *102*, 177404.

(15) Takeuchi, S. Recent progress in single-photon and entangled-photon generation and applications. *Jpn. J. Appl. Phys.* **2014**, *53*, 030101.

(16) Talapin, D. V.; Lee, J.-S.; Kovalenko, M. V.; Shevchenko, E. V. Prospects of Colloidal Nanocrystals for Electronic and Optoelectronic Applications. *Chem. Rev.* **2010**, *110*, 389–458.

(17) Xie, X. S.; Trautman, J. K. Optical studies of single molecules at room temperature. *Annu. Rev. Phys. Chem.* **1998**, *49*, 441–480.

(18) Moerner, W. E.; Fromm, D. P. Methods of single-molecule fluorescence spectroscopy and microscopy. *Rev. Sci. Instrum.* **2003**, *74*, 3597–3619.

(19) Lakowicz, J. R., *Principles of Fluorescence Spectroscopy*, Third; Springer Science+Business Media: New York, 2006.

(20) Brooks Shera, E.; Seitzinger, N. K.; Davis, L. M.; Keller, R. A.; Soper, S. A. Detection of single fluorescent molecules. *Chem. Phys. Lett.* **1990**, *174*, 553–557.

(21) Müller, M., *Introduction to Confocal Fluorescence Microscopy*, Second; The Society of Photo-Optical Instrumentation Engineers: Bellingham, 2006.

(22) Taylor, J. R., *An Introduction to Error Analysis: The Study of Uncertainties in Physical Measurements*, Second; University Science Books: Sausalito, 1997.

(23) Nirmal, M.; Dabbousi, B. O.; Bawendi, M. G.; Macklin, J. J.; Trautman, J. K; Harris, T. D.; Brus, L. E. Fluorescence Intermittency in Single CdSe Nanocrystals. *Nature* **1996**, *383*, 802–804.

(24) Ambrose, W. P.; Goodwin, P. M.; Martin, J. C.; Keller, R. A. Alterations of Single Molecule Fluorescence Lifetimes in Near-Field Optical Microscopy. *Science* **1994**, *265*, 364–367.

(25) Xie, X. S.; Dunn, R. C. Probing single molecule dynamics. *Science* **1994**, *265*, 361–364.

(26) Frantsuzov, P.; Kuno, M.; Jankó, B.; Marcus, R. A. Universal emission intermittency in quantum dots, nanorods and nanowires. *Nat. Phys.* **2008**, *4*, 519–522.

(27) Kuno, M.; Fromm, D. P.; Hamann, H. F.; Gallagher, A.; Nesbitt, D. J. "On"/"off" fluorescence intermittency of single semiconductor quantum dots. *J. Chem. Phys.* **2001**, *115*, 1028–1040.

(28) Efros, A. L.; Rosen, M. Random telegraph signal in the photoluminescence intensity of a single quantum dot. *Phys. Rev. Lett.* **1997**, *78*, 1110–1113.

(29) Kuno, M.; Fromm, D. P.; Hamann, H. F.; Gallagher, A.; Nesbitt, D. J. Nonexponential blinking kinetics of single CdSe quantum dots: A universal power law behavior. *J. Chem. Phys.* **2000**, *112*, 3117–3120.

(30) Cordones, A. A.; Leone, S. R. Mechanisms for charge trapping in single semiconductor nanocrystals probed by fluorescence blinking. *Chem. Soc. Rev.* **2013**, *42*, 3209–3221.

(31) Cannavò, F.; Nunnari, G. On a Possible Unified Scaling Law for Volcanic Eruption Durations. *Sci. Rep.* **2016**, *6*, 22289.

(32) Carreras, B. A.; Lynch, V. E.; Dobson, I.; Newman, D. E. Complex dynamics of blackouts in power transmission systems. *Chaos* **2004**, *14*, 643–652.

(33) Efros, A. L.; Nesbitt, D. J. Origin and control of blinking in quantum dots. *Nat. Nanotechnol.* **2016**, *11*, 661–671.

(34) Frantsuzov, P. A.; Volkán-Kacsó, S.; Jankó, B. Model of fluorescence intermittency of single colloidal semiconductor quantum dots using multiple recombination centers. *Phys. Rev. Lett.* **2009**, *103*, 207402.

(35) Cichos, F.; von Borczyskowski, C.; Orrit, M. Power-law intermittency of single emitters. *Curr. Opin. Colloid Interface Sci.* **2007**, *12*, 272–284.

(36) Boyd, R. W., *Nonlinear Optics*, Third; Elsevier: Burlington, 2008.

(37) Brodeur, A.; Chin, S. L. Ultrafast white-light continuum generation and self-focusing in transparent condensed media. *J. Opt. Soc. Am. B* **1999**, *16*, 637–650.

(38) Wahl, M. *Time-Correlated Single Photon Counting*; tech. rep.; PicoQuant GmbH, 2014, pp 1–14.

(39) Barkai, E.; Jung, Y.; Silbey, R. Theory of Single-Molecule Spectroscopy: Beyond the Ensemble Average. *Annu. Rev. Phys. Chem.* **2004**, *55*, 457–507.

(40) Hanbury Brown, R.; Twiss, R. Q. Correlation between photons in two coherent beams of light. *Nature* **1956**, *177*, 27–29.

(41) Fisher, B. R.; Eisler, H.-J.; Stott, N. E.; Bawendi, M. G. Emission intensity dependence and single-exponential behavior in single colloidal quantum dot fluorescence lifetimes. *J. Phys. Chem. B* **2004**, *108*, 143–148.

(42) Makarov, N. S.; Guo, S.; Isaienko, O.; Liu, W.; Robel, I.; Klimov, V. I. Spectral and Dynamical Properties of Single Excitons, Biexcitons, and Trions in Cesium-Lead-Halide Perovskite Quantum Dots. *Nano Lett.* **2016**, *16*, 2349–2362.

(43) Crouch, C. H.; Sauter, O.; Wu, X.; Purcell, R.; Querner, C.; Drndic, M.; Pelton, M. Facts and artifacts in the blinking statistics of semiconductor nanocrystals. *Nano Lett.* **2010**, *10*, 1692–1698.

(44) Shimizu, K. T.; Neuhauser, R. G.; Leatherdale, C. A.; Empedocles, S. A.; Woo, W. K.; Bawendi, M. G. Blinking statistics in single semiconductor nanocrystal quantum dots. *Phys. Rev. B - Condens. Matter Mater. Phys.* **2001**, *63*, 205316.

(45) Galland, C.; Ghosh, Y.; Steinbrück, A.; Sykora, M.; Hollingsworth, J. A.; Klimov, V. I.; Htoon, H. Two types of luminescence blinking revealed by spectroelectrochemistry of single quantum dots. *Nature* **2011**, *479*, 203–207.

(46) Chung, I.; Bawendi, M. G. Relationship between single quantum-dot intermittency and fluorescence intensity decays from collections of dots. *Phys. Rev. B - Condens. Matter Mater. Phys.* **2004**, *70*, 165304.

(47) Peterson, J. J.; Nesbitt, D. J. Modified power law behavior in quantum dot blinking: A novel role for biexcitons and auger ionization. *Nano Lett.* **2009**, *9*, 338–345.

(48) Watkins, L. P.; Yang, H. Detection of intensity change points in time-resolved single-molecule measurements. *J. Phys. Chem. B* **2005**, *109*, 617–628.

(49) Houel, J.; Doan, Q. T.; Cajgfinger, T.; Ledoux, G.; Amans, D.; Aubret, A.; Dominjon, A.; Ferriol, S.; Barbier, R.; Nasilowski, M.; Lhuillier, E.; Dubertret, B.; Dujardin, C.; Kulzer, F. Autocorrelation analysis for the unbiased determination of power-law exponents in single-quantum-dot blinking. *ACS Nano* **2015**, *9*, 886–893.

(50) Yang, H.; Xie, X. S. Probing single-molecule dynamics photon by photon. *J. Chem. Phys.* **2002**, *117*, 10965–10979.

(51) Volkán-Kacsó, S. Two-state theory of binned photon statistics for a large class of waiting time distributions and its application to quantum dot blinking. *J. Chem. Phys.* **2014**, *140*, 224110.

(52) Gopich, I. V.; Szabo, A. Theory of the statistics of kinetic transitions with application to single-molecule enzyme catalysis. *J. Chem. Phys.* **2006**, *124*, 154712.

(53) Pelton, M.; Grier, D. G.; Guyot-Sionnest, P. Characterizing quantum-dot blinking using noise power spectra. *Appl. Phys. Lett.* **2004**, *85*, 819–821.

(54) Pelton, M.; Smith, G.; Scherer, N. F.; Marcus, R. A. Evidence for a diffusion-controlled mechanism for fluorescence blinking of colloidal quantum dots. *Proc. Natl. Acad. Sci.* **2007**, *104*, 14249–14254.

(55) Messin, G.; Hermier, J. P.; Giacobino, E.; Desbiolles, P.; Dahan, M. Bunching and antibunching in the fluorescence of semiconductor nanocrystals. *Opt. Lett.* **2001**, *26*, 1891–1893.

(56) Qin, W.; Guyot-Sionnest, P. Evidence for the role of holes in blinking: Negative and oxidized CdSe/CdS dots. *ACS Nano* **2012**, *6*, 9125–9132.

(57) Spinicelli, P.; Buil, S.; Quélin, X.; Mahler, B.; Dubertret, B.; Hermier, J. P. Bright and grey states in CdSe-CdS nanocrystals exhibiting strongly reduced blinking. *Phys. Rev. Lett.* **2009**, *102*, 136801.

(58) Tenne, R.; Teitelboim, A.; Rukenstein, P.; Dyshel, M.; Mokari, T.; Oron, D. Studying quantum dot blinking through the addition of an engineered inorganic hole trap. *ACS Nano* **2013**, *7*, 5084–5090.

(59) Gomez, D. E.; van Embden, J; Mulvaney, P; Fernee, M. J.; Rubinsztein-Dunlop, H Exciton-trion transitions in single CdSe-CdS core-shell nanocrystals. *ACS Nano* **2009**, *3*, 2281–2287.

(60) Chen, O.; Zhao, J.; Chauhan, V. P.; Cui, J.; Wong, C.; Harris, D. K.; Wei, H.; Han, H. S.; Fukumura, D.; Jain, R. K.; Bawendi, M. G. Compact high-quality CdSe-CdS core-shell nanocrystals with narrow emission linewidths and suppressed blinking. *Nat. Mater.* **2013**, *12*, 445–451.

(61) Verberk, R.; Van Oijen, A. M.; Orrit, M. Simple model for the power-law blinking of single semiconductor nanocrystals. *Phys. Rev. B - Condens. Matter Mater. Phys.* **2002**, *66*, 233202.

(62) Zhang, K.; Chang, H.; Fu, A.; Alivisatos, A. P.; Yang, H. Continuous distribution of emission states from single CdSe/ZnS quantum dots. *Nano Lett.* **2006**, *6*, 843–847.

(63) Osborne, M. A.; Fisher, A. A. E. Charge-tunnelling and self-trapping: common origins for blinking, grey-state emission and photoluminescence enhancement in semiconductor quantum dots. *Nanoscale* **2016**, *8*, 9272–9283.

(64) Green, M. A.; Ho-Baillie, A.; Snaith, H. J. The emergence of perovskite solar cells. *Nat. Photonics* **2014**, *8*, 506–514.

(65) Hou, H.; Chen, Q.; Li, G.; Luo, S.; Song, T. B.; Duan, H. S.; Hong, Z.; You, J.; Liu, Y.; Yang, Y. Interface engineering of highly efficient perovskite solar cells. *Science* **2014**, *345*, 542–546.

(66) Jeon, N. J.; Noh, J. H.; Yang, W. S.; Kim, Y. C.; Ryu, S.; Seo, J.; Seok, S. I. Compositional engineering of perovskite materials for high-performance solar cells. *Nature* **2015**, *517*, 476–480.

(67) Tan, Z.-K.; Moghaddam, R. S.; Lai, M. L.; Docampo, P.; Higler, R.; Deschler, F.; Price, M.; Sadhanala, A.; Pazos, L. M.; Credgington, D.; Hanusch, F.; Bein, T.; Snaith, H. J.; Friend, R. H. Bright light-emitting diodes based on organometal halide perovskite. *Nat. Nanotechnol.* **2014**, *9*, 687–692.

(68) Li, G.; Tan, Z. K.; Di, D.; Lai, M. L.; Jiang, L.; Lim, J. H. W.; Friend, R. H.; Greenham, N. C. Efficient Light-Emitting Diodes Based on Nanocrystalline Perovskite in a Dielectric Polymer Matrix. *Nano Lett.* **2015**, *15*, 2640–2644.

(69) Xing, G.; Mathews, N.; Lim, S. S.; Yantara, N.; Liu, X.; Sabba, D.; Grätzel, M.; Mhaisalkar, S.; Sum, T. C. Low-temperature solution-processed wavelength-tunable perovskites for lasing. *Nat. Mater.* **2014**, *13*, 476–480.

(70) Eaton, S. W.; Lai, M.; Gibson, N. A.; Wong, A. B.; Dou, L.; Ma, J.; Wang, L.-W.; Leone, S. R.; Yang, P. Lasing in robust cesium lead halide perovskite nanowires. *Proc. Natl. Acad. Sci.* **2016**, *113*, 1993–1998.

(71) Zhu, H.; Fu, Y.; Meng, F.; Wu, X.; Gong, Z.; Ding, Q.; Gustafsson, M. V.; Trinh, M. T.; Jin, S.; Zhu, X. Y. Lead halide perovskite nanowire lasers with low lasing thresholds and high quality factors. *Nat. Mater.* **2015**, *14*, 636–642.

(72) Bekenstein, Y.; Koscher, B. A.; Eaton, S. W.; Yang, P.; Alivisatos, A. P. Highly Luminescent Colloidal Nanoplates of Perovskite Cesium Lead Halide and Their Oriented Assemblies. *J. Am. Chem. Soc.* **2015**, *137*, 16008–16011.

(73) Protesescu, L.; Yakunin, S.; Bodnarchuk, M. I.; Krieg, F.; Caputo, R.; Hendon, C. H.; Yang, R. X.; Walsh, A.; Kovalenko, M. V. Nanocrystals of Cesium Lead Halide Perovskites ($CsPbX_3$, X = Cl, Br, and I): Novel Optoelectronic Materials Showing Bright Emission with Wide Color Gamut. *Nano Lett.* **2015**, *15*, 3692–3696.

(74) Buin, A.; Pietsch, P.; Xu, J.; Voznyy, O.; Ip, A. H.; Comin, R.; Sargent, E. H. Materials processing routes to trap-free halide perovskites. *Nano Lett.* **2014**, *14*, 6281–6286.

(75) Brandt, R. E.; Stevanovic, V.; Ginley, D. S.; Buonassisi, T. Identifying defect-tolerant semiconductors with high minority-carrier lifetimes: Beyond hybrid lead halide perovskites. *MRS Commun.* **2015**, *5*, 265–275.

(76) Kang, J.; Wang, L. W. High Defect Tolerance in Lead Halide Perovskite $CsPbBr_3$. *J. Phys. Chem. Lett.* **2017**, *8*, 489–493.

(77) Tang, J.; Marcus, R. A. Diffusion-controlled electron transfer processes and power-law statistics of fluorescence intermittency of nanoparticles. *Phys. Rev. Lett.* **2005**, *95*, 107401.

(78) Tang, J.; Marcus, R. A. Mechanisms of fluorescence blinking in semiconductor nanocrystal quantum dots. *J. Chem. Phys.* **2005**, *123*, 054704.

(79) Califano, M. Off-state quantum yields in the presence of surface trap states in CdSe Nanocrystals: The inadequacy of the charging model to explain blinking. *J. Phys. Chem. C* **2011**, *115*, 18051–18054.

(80) Jha, P. P.; Guyot-Sionnest, P. Trion decay in colloidal quantum dots. *ACS Nano* **2009**, *3*, 1011–1015.

(81) Zhao, J.; Nair, G.; Fisher, B. R.; Bawendi, M. G. Challenge to the charging model of semiconductor-nanocrystal fluorescence intermittency from off-state quantum yields and multiexciton blinking. *Phys. Rev. Lett.* **2010**, *104*, 157403.

(82) Frantsuzov, P. A.; Marcus, R. A. Explanation of quantum dot blinking without the long-lived trap hypothesis. *Phys. Rev. B - Condens. Matter Mater. Phys.* **2005**, *72*, 155321.

(83) Hu, F.; Zhang, H.; Sun, C.; Yin, C.; Lv, B.; Zhang, C.; Yu, W. W.; Wang, X.; Zhang, Y.; Xiao, M. Superior Optical Properties of Perovskite Nanocrystals as Single Photon Emitters. *ACS Nano* **2015**, *9*, 12410–12416.

(84) Swarnkar, A.; Chulliyil, R.; Ravi, V. K.; Irfanullah, M.; Chowdhury, A.; Nag, A. Colloidal $CsPbBr_3$ Perovskite Nanocrystals: Luminescence beyond Traditional Quantum Dots. *Angew. Chemie - Int. Ed.* **2015**, *54*, 15424–15428.

(85) Seth, S.; Mondal, N.; Patra, S.; Samanta, A. Fluorescence Blinking and Photoactivation of All-Inorganic Perovskite Nanocrystals $CsPbBr_3$ and $CsPbBr_2I$. *J. Phys. Chem. Lett.* **2016**, *7*, 266–271.

(86) Park, Y. S.; Guo, S.; Makarov, N. S.; Klimov, V. I. Room Temperature Single-Photon Emission from Individual Perovskite Quantum Dots. *ACS Nano* **2015**, *9*, 10386–10393.

(87) Wen, X.; Ho-Baillie, A.; Huang, S.; Sheng, R.; Chen, S.; Ko, H. C.; Green, M. A. Mobile Charge-Induced Fluorescence Intermittency in Methylammonium Lead Bromide Perovskite. *Nano Lett.* **2015**, *15*, 4644–4649.

(88) Tian, Y.; Merdasa, A.; Peter, M.; Abdellah, M.; Zheng, K.; Ponseca, C. S.; Pullerits, T.; Yartsev, A.; Sundström, V.; Scheblykin, I. G. Giant photoluminescence blinking of perovskite nanocrystals reveals single-trap control of luminescence. *Nano Lett.* **2015**, *15*, 1603–1608.

(89) Tachikawa, T.; Karimata, I.; Kobori, Y. Surface Charge Trapping in Organolead Halide Perovskites Explored by Single-Particle Photoluminescence Imaging. *J. Phys. Chem. Lett.* **2015**, *6*, 3195–3201.

(90) Cottingham, P.; Brutchey, R. L. On the crystal structure of colloidally prepared $CsPbBr_3$ quantum dots. *Chem. Commun.* **2016**, *52*, 5246–5249.

(91) Chen, J.; Žídek, K.; Chábera, P.; Liu, D.; Cheng, P.; Nuuttila, L.; Al-Marri, M. J.; Lehtivuori, H.; Messing, M. E.; Han, K.; Zheng, K.; Pullerits, T. Size- and Wavelength-Dependent Two-Photon Absorption Cross-Section of $CsPbBr_3$ Perovskite Quantum Dots. *J. Phys. Chem. Lett.* **2017**, *8*, 2316–2321.

(92) Schwartz, O.; Tenne, R.; Levitt, J. M.; Deutsch, Z.; Itzhakov, S.; Oron, D. Colloidal quantum dots as saturable fluorophores. *ACS Nano* **2012**, *6*, 8778–8782.

(93) Cheng Yuan, G.; Ritchie, C.; Ritter, M.; Murphy, S.; Gomez, D. E.; Mulvaney, P. The Degradation and Blinking of Single $CsPbI_3$ Perovskite Quantum Dots. *J. Phys. Chem. C* **2017**, *122*, 13407–13415.

(94) Raja, S. N.; Bekenstein, Y.; Koc, M. A.; Fischer, S.; Zhang, D.; Lin, L.; Ritchie, R. O.; Yang, P.; Alivisatos, A. P. Encapsulation of Perovskite Nanocrystals into Macroscale Polymer Matrices: Enhanced Stability and Polarization. *ACS Appl. Mater. Interfaces* **2016**, *8*, 35523–35533.

(95) Bae, Y. J.; Gibson, N. A.; Ding, T. X.; Alivisatos, A. P.; Leone, S. R. Understanding the Bias Introduced in Quantum Dot Blinking Using Change Point Analysis. *J. Phys. Chem. C* **2016**, *120*, 29484–29490.

(96) Early, K. T.; Nesbitt, D. J. Size-dependent photoionization in single CdSe/ZnS nanocrystals. *Nano Lett.* **2013**, *13*, 4844–4849.

(97) Stefani, F. D.; Knoll, W.; Kreiter, M.; Zhong, X.; Han, M. Y. Quantification of photoinduced and spontaneous quantum-dot luminescence blinking. *Phys. Rev. B - Condens. Matter Mater. Phys.* **2005**, *72*, 125304.

(98) Frantsuzov, P. A.; Volkán-Kacsó, S.; Jankó, B. Universality of the fluorescence intermittency in nanoscale systems: Experiment and theory. *Nano Lett.* **2013**, *13*, 402–408.

(99) Rainoì, G.; Nedelcu, G.; Protesescu, L.; Bodnarchuk, M. I.; Kovalenko, M. V.; Mahrt, R. F.; Stöferle, T. Single Cesium Lead Halide Perovskite Nanocrystals at Low Temperature: Fast Single-Photon Emission, Reduced Blinking, and Exciton Fine Structure. *ACS Nano* **2016**, *10*, 2485–2490.

(100) Couteau, C.; Larrue, A.; Wilhelm, C.; Soci, C. Nanowire lasers. *Nanophotonics* **2015**, *4*, 90–107.

(101) Zimmler, M. A.; Bao, J.; Capasso, F.; Müller, S.; Ronning, C. Laser action in nanowires: Observation of the transition from amplified spontaneous emission to laser oscillation. *Appl. Phys. Lett.* **2008**, *93*, 2006–2009.

(102) Zhang, D.; Eaton, S. W.; Yu, Y.; Dou, L.; Yang, P. Solution-Phase Synthesis of Cesium Lead Halide Perovskite Nanowires. *J. Am. Chem. Soc.* **2015**, *137*, 9230–9233.

(103) Lin, Q.; Armin, A.; Lyons, D. M.; Burn, P. L.; Meredith, P. Low noise, IR-blind organohalide perovskite photodiodes for visible light detection and imaging. *Adv. Mater.* **2015**, *27*, 2060–2064.

(104) Yakunin, S.; Protesescu, L.; Krieg, F.; Bodnarchuk, M. I.; Nedelcu, G.; Humer, M.; De Luca, G.; Fiebig, M.; Heiss, W.; Kovalenko, M. V. Low-threshold amplified spontaneous emission and lasing from colloidal nanocrystals of caesium lead halide perovskites. *Nat. Commun.* **2015**, *6*, 8056.

(105) Wang, Y.; Li, X.; Song, J.; Xiao, L.; Zeng, H.; Sun, H. All-Inorganic Colloidal Perovskite Quantum Dots: A New Class of Lasing Materials with Favorable Characteristics. *Adv. Mater.* **2015**, *27*, 7101–7108.

(106) Klimov, V. I. Spectral and Dynamical Properties of Multiexcitons in Semiconductor Nanocrystals. *Annu. Rev. Phys. Chem.* **2007**, *58*, 635–673.

(107) Johnson, J. C.; Yan, H.; Yang, P.; Saykally, R. J. Optical Cavity Effects in ZnO Nanowire Lasers and Waveguides. *J. Phys. Chem. B* **2003**, *107*, 8816–8828.

(108) Johnson, J. C.; Choi, H. J.; Knutsen, K. P.; Schaller, R. D.; Yang, P.; Saykally, R. J. Single gallium nitride nanowire lasers. *Nat. Mater.* **2002**, *1*, 106–110.

(109) Kulbak, M.; Cahen, D.; Hodes, G. How Important Is the Organic Part of Lead Halide Perovskite Photovoltaic Cells? Efficient $CsPbBr_3$ Cells. *J. Phys. Chem. Lett.* **2015**, *6*, 2452–2456.

(110) Conings, B.; Drijkoningen, J.; Gauquelin, N.; Babayigit, A.; D'Haen, J.; D'Olieslaeger, L.; Ethirajan, A.; Verbeeck, J.; Manca, J.; Mosconi, E.; De Angelis, F.; Boyen, H. G. Intrinsic Thermal Instability of Methylammonium Lead Trihalide Perovskite. *Adv. Energy Mater.* **2015**, *5*, 1500477.

(111) Sutherland, B. R.; Hoogland, S.; Adachi, M. M.; Wong, C. T. O.; Sargent, E. H. Conformal organohalide perovskites enable lasing on spherical resonators. *ACS Nano* **2014**, *8*, 10947–10952.

(112) Zhang, D.; Yang, Y.; Bekenstein, Y.; Yu, Y.; Gibson, N. A.; Wong, A. B.; Eaton, S. W.; Kornienko, N.; Kong, Q.; Lai, M.; Alivisatos, A. P.; Leone, S. R.; Yang, P. Synthesis of Composition Tunable and Highly Luminescent Cesium Lead Halide Nanowires through Anion-Exchange Reactions. *J. Am. Chem. Soc.* **2016**, *138*, 7236–7239.

(113) Kornienko, N.; Gibson, N. A.; Zhang, H.; Eaton, S. W.; Yu, Y.; Aloni, S.; Leone, S. R.; Yang, P. Growth and Photoelectrochemical Energy Conversion of Wurtzite Indium Phosphide Nanowire Arrays. *ACS Nano* **2016**, *10*, 5525–5535.